Scuola Internazionale Superiore di Studi Avanzati

Doctoral Thesis

Relaxation phenomena in isolated integrable quantum systems

Author:
Márton Mestyán

Supervisor:
Prof. Pasquale Calabrese

A thesis submitted in fulfillment of the requirements for the degree of Doctor of Philosophy

in the

PhD Course in Statistical Physics

Preface

In this Thesis I present the results of four research projects I carried out during my Ph.D. training at SISSA. The broad topic of my research was the mechanism of relaxation in isolated, *integrable* quantum systems. Roughly speaking, integrable quantum systems are one-dimensional lattice models or field theories that feature an extensively large number of conservation laws beyond energy and momentum conservation, which greatly influence their dynamical behaviour. Integrable systems have enjoyed a considerable interest in the last decade, mainly due to the development of ultracold atomic techniques. These techniques made it possible to implement experimentally a wealth of one-dimensional quantum models whose significance had been purely theoretical before.

The theoretical interest in integrable systems stems in part from the fact that in many aspects they are *exactly* solvable. Exact analytical formulas are available for their spectrum and their equilibrium thermodynamic properties, creating an incentive to study analytically their non-equilibrium behaviour as well. Exact results for the dynamics of integrable systems may serve as a benchmark for confirming theories in statistical mechanics or testing approximative methods.

To this day, computing analytically the entire time evolution of observables in a genuinely interacting integrable system is prohibitively difficult in general. In this Thesis, I concentrate on the description of the system at long times after it is brought out of equilibrium. Homogeneous, translationally invariant integrable systems are expected to relax to a stationary state, in which local observables are described by a generalization of the Gibbs ensemble that takes into consideration all the conservation laws beyond the energy. Two of the projects presented here concern this relaxed state.

In Chapter 2, a method is presented for computing the Rényi entropies of the Generalized Gibbs Ensemble describing the relaxed state in the integrable Heisenberg XXZ spin chain. Rényi entropies provide information about the relaxed state and its entanglement properties, going beyond the ordinary von Neumann thermodynamic entropy. The method presented there is very general; in principle it works in any integrable model and any translationally invariant thermodynamic macrostate.

An alternative to the GGE in describing relaxed states after a quantum quench is the Quench Action approach. This approach is based on the explicit analytical knowledge of the overlaps between the initial state and the Hamiltonian eigenstates. In Chapter 3, this approach is generalized to a spin-1 integrable spin chain, the SU(3) invariant Lai–Sutherland model. The evolution of entanglement is then studied using

the quasiparticle picture, which features ballistically propagating classical particle pairs carrying entanglement.

If the requirement of translational invariance of the initial state is relaxed, various transport phenomena arise in integrable systems. The evolution of slowly varying, smoothly distributed states is described by a generalization of hydrodynamics, which takes into consideration the infinitely many local conservation laws. At the scale of non-diffusive, ballistic transport, the main feature of this generalized hydrodynamics (GHD) is the existence of continuity equations for the occupation number of each mode. Further two projects are presented in this Thesis which are concerned with GHD.

In Chapter 4, a numerical method is presented for computing the evolution of entanglement entropies within GHD. This method combines the quasiparticle picture of entanglement with a molecular dynamics simulation of GHD, the so-called flea gas. Numerical evidence is shown that this method reproduces previously known analytical results in GHD. Its versatility is demonstrated by computing another entanglement-related quantity, the mutual information, for which no analytical results are available.

Finally, in Chapter 5, the GHD framework is generalized to a system of spin-1/2 fermions with repulsive contact interaction, the Yang–Gaudin model. It is shown that at low temperatures, the dynamics of the system is described by the superposition of two uncoupled, inhomogeneous conformal field theories. This fact can be interpreted as a separation of the spin and the charge degrees of freedom of the system.

List of Publications

Publications related to this Thesis

1. M. Mestyán, B. Bertini, L. Piroli, and P. Calabrese,
   "Exact solution for the quench dynamics of a nested integrable system",
   J. Stat. Mech. **2017**, 083103 (2017).

2. M. Mestyán, V. Alba, and P. Calabrese,
   "Rényi entropies of generic thermodynamic macrostates in integrable systems",
   J. Stat. Mech. **2018**, 083104 (2018).

3. M. Mestyán, B. Bertini, L. Piroli, and P. Calabrese,
   "Spin-charge separation effects in the low-temperature transport of 1D Fermi gases",
   Phys. Rev. B **99**, 014305 (2019).

Preprints related to this Thesis

1. M. Mestyán, V. Alba,
   "Molecular dynamics simulation of entanglement spreading in generalized hydrodynamics",
   arXiv:1905.03206 (2019).

Contents

Chapter 1

Introduction

Non-equilibrium isolated quantum many-body systems became the topic of intense research [1–3] after their experimental realization was made possible by ultracold atomic techniques [4–7]. The investigations of this Thesis deal with a subset of these systems: systems that also feature integrability. In rough terms, integrable quantum systems possess an infinite number of local conservation laws that greatly influence their dynamics. These systems moved out of the purely theoretical realm after the famous "quantum Newton cradle" experiment [8], in which signatures of integrability were observed in a 1D system of bosons, described by the integrable Lieb–Liniger gas [9]. Since then, non-equilibrium integrable systems have become a field of study in their own right [10].

The aim of this Introduction is to summarize the main out-of-equilibrium properties of integrable quantum systems and provide the technical framework for the following Chapters. While there are various integrability-specific approximative treatments, such as perturbation theory [11] or truncated space algorithms [12, 13], we focus on exact, analytical methods. We choose the anisotropic Heisenberg spin chain as a paradigmatic model to demonstrate the concepts related to integrability and – on a technical level – to introduce Bethe ansatz related notations.

1.1 Isolated quantum systems out of equilibrium

The paradigmatic out-of-equilibrium setting of an isolated quantum system is the quantum quench. In a quantum quench the system is initially prepared in a state described by a density matrix ρ_0, then it is evolved with the system Hamiltonian

$$\rho(t) = e^{-iHt}\rho_0\, e^{iHt}. \tag{1.1}$$

For now, let us suppose that the Hamiltonian is translationally invariant, and the initial state is a translationally invariant pure state $\rho_0 = |\Psi_0\rangle\langle\Psi_0|$. One of the most important questions is how does the system behave in the long time limit, i.e., whether it thermalizes. Thermalization in the global sense would mean that the

long-time limit of $\rho(t)$ would be a Gibbs ensemble density matrix

$$\rho_{\mathrm{GE}} = \frac{1}{Z_{GE}} e^{-\beta H}, \quad Z_{\mathrm{GE}} = \mathrm{Tr}\, e^{-\beta H}. \tag{1.2}$$

However, (1.2) cannot be the long-time limit of $\rho(t)$ because the unitary evolution (1.1) preserves $\mathrm{Tr}\,\rho^2(t)$, and thus it cannot lead to a mixed state from a pure initial state. In other words, thermalization in the global sense is not possible.

Thermalization may occur in an isolated system in a local sense. Local thermalization is defined using the notion of local operators, which depend on only a few degrees of freedom. For example, on a lattice system of L sites, local operators have the form

$$O = \sum_{r=0}^{L-1} \mathcal{T}_r \sum_{k=1}^{K} \mathcal{O}_k, \tag{1.3}$$

where $\mathcal{O}_k$ acts on at most k neighboring sites, K is a finite integer, and $\mathcal{T}_r$ is the r-site translation operator (with periodic boundary conditions). In general, the local observables O of a translationally invariant, generic (non-integrable) system are expected to satisfy

$$\lim_{T\to\infty} \lim_{L\to\infty} \frac{1}{T} \int_0^T dt \langle O(t) \rangle = \mathrm{Tr}\, \rho_{GE}\, O. \tag{1.4}$$

This means that in the thermodynamic limit, the long-time average of expectation value of all local operators can be expressed by the same thermal density matrix (1.2). The Lagrange multiplier β appearing in the density matrix is determined by the requirement of energy conservation

$$\mathrm{Tr}\, \rho_{GE} H = \langle \Psi_0 | H | \Psi_0 \rangle. \tag{1.5}$$

One of the most important questions regarding isolated non-equilibrium systems is how local thermalization (1.4) occurs.

The most probable mechanism of (1.4) is given by the eigenstate thermalization hypothesis (ETH) and the diagonal ensemble (DE). In order to introduce the ETH, the time average on the left hand side of (1.4) can be rewritten using the full set of energy eigenstates $H|n\rangle = E_n|n\rangle$ as

$$\begin{aligned} \frac{1}{T} \int_0^T dt \langle O(t) \rangle &= \frac{1}{T} \int_0^T dt \langle \Psi_0 | e^{iHt} O e^{-iHt} | \Psi_0 \rangle \\ &= \frac{1}{T} \int_0^T dt \sum_{n,m} e^{-i(E_n - E_m)t} \langle \Psi_0 | m \rangle \langle m | O | n \rangle \langle n | \Psi_0 \rangle. \end{aligned} \tag{1.6}$$

The eigenstate thermalization hypothesis states that for all the energy eigenstates $|n\rangle$ whose energies fall in a small interval $(E, E+\delta E)$, the expectation value of a local observable $\langle n|O|n\rangle$ will be the same in the thermodynamic limit. More precisely, for local observable O satisfying the ETH, it holds that [14–20]

$$\langle m | O | n \rangle = f_O(E) \delta_{m,n} + O(e^{-\xi L}) \quad (\xi > 0), \tag{1.7}$$

where $E = (E_m + E_n)/2$, and most importantly, $f_O(E)$ is a smooth function of E. Using (1.7) on (1.6), one obtains

$$\lim_{T\to\infty}\lim_{L\to\infty}\frac{1}{T}\int_0^T dt\langle O(t)\rangle = \lim_{L\to\infty}\sum_n \langle n|O|n\rangle|\langle\Psi_0|n\rangle|^2. \tag{1.8}$$

The right-hand side can be interpreted as an ensemble average

$$\mathrm{Tr}\,\rho_{\mathrm{DE}}\,O, \qquad \rho_{\mathrm{DE}} = \sum_n \left(|\langle n|\Psi_0\rangle|^2\right)\,|n\rangle\langle n|. \tag{1.9}$$

The density matrix ρ_{DE} defines the diagonal ensemble. In the thermodynamic limit, the ensemble average (1.9) is equal to the Gibbs ensemble prediction (1.4) because of the ETH (1.7): since the diagonal matrix element $f_O(E)$ is a smooth function of the energy, the average (1.9) can be computed using a canonical ensemble with density matrix (1.9) that ensures energy conservation by the Lagrange multiplier β. This is the mechanism of thermalization in the local sense.

In this Thesis the particular class of *integrable* quantum systems is considered, for which the above reasoning breaks down. Integrable systems possess an extensive amount of local operators $Q_s^{(j)}$ that commute with each other. They also commmute with the system Hamiltonian, thus their expectation value is conserved. In these systems, the Gibbs ensemble (1.2) yields the correct mean value of the energy but for other conserved charges

$$\mathrm{Tr}\,\rho_{\mathrm{GE}}Q_s^{(j)} \neq \langle\Psi_0|Q_s^{(j)}|\Psi_0\rangle. \tag{1.10}$$

Since the Gibbs ensemble does not satisfy all the conservation laws, it cannot be the correct description of the relaxed state in the long time limit. The rest of this Introduction will be devoted to how the long time relaxed state can be still described in integrable systems.

1.2 Quantum integrable models: the XXZ spin chain

Before elaborating on equilibration in integrable systems, we give a brief overview of quantum integrability itself. Specifically, we summarize the Bethe ansatz framework for obtaining the spectrum and the thermodynamics of an integrable system. This also allows us to set Bethe ansatz notations for the rest of this Thesis. We do not show the tedious derivation of the Bethe ansatz formulae (for which many good introductory texts exist, see e.g. [21–23]), and instead focus on the interpretation of the formulae.

In the following, the spin-1/2 XXZ Heisenberg spin chain will be used to showcase the general features of quantum integrable systems. The Bethe ansatz solution for the spectrum of this lattice model is relatively simple and the model itself is among

the most studied integrable systems. The Hilbert space of the model consists of L spin-1/2 sites, $\mathcal{H} = \{\mathbb{C}^2\}^{\otimes L}$. The Hamiltonian is

$$H = \sum_{k=1}^{L} \left[\sigma_k^x \sigma_{k+1}^x + \sigma_k^y \sigma_{k+1}^y + \Delta \left(\sigma_k^z \sigma_{k+1}^z - 1\right)\right]. \tag{1.11}$$

The matrices σ_k^α are the standard Pauli matrices

$$\sigma^x = \begin{pmatrix} 0 & 1 \\ 1 & 0 \end{pmatrix}, \qquad \sigma^y = \begin{pmatrix} 0 & -i \\ i & 0 \end{pmatrix}, \qquad \sigma^z = \begin{pmatrix} 1 & 0 \\ 0 & -1 \end{pmatrix}, \tag{1.12}$$

which act on the k-th site. Periodic boundary conditions are implied by $\sigma_{L+1}^\alpha = \sigma_1^\alpha$. The parameter Δ is called the anisotropy parameter. The system has a finite gap in the thermodynamic limit at $\Delta > 1$, while it is gapless at $\Delta \leq 1$. In the following, we consider the case $\Delta > 1$,

1.2.1 Bethe ansatz solution at finite size

The Bethe ansatz eigenstates of the XXZ Hamiltonian (1.11) are constructed over the ferromagnetic reference state $|\uparrow\uparrow \ldots \uparrow\rangle$. Since the Hamiltonian commutes with the total magnetization $S^z_{\text{tot}} = \sum_j \sigma_j^z/2$, the eigenstates can be expanded over the states with a definite number N of down spins and $L - N$ up spins. A generic eigenstate satisfying $H|\boldsymbol{\lambda}\rangle = E_{\boldsymbol{\lambda}}|\boldsymbol{\lambda}\rangle$ can be expanded as

$$|\boldsymbol{\lambda}\rangle = \sum_{n_1 < n_2 < \cdots < n_N} \psi(n_1, n_2, \ldots, n_N) \sigma_{n_1}^- \sigma_{n_2}^- \ldots \sigma_{n_N}^- |\uparrow\uparrow \ldots \uparrow\rangle, \tag{1.13}$$

where $\sigma_k^\pm$ are the spin raising and lowering operators

$$\sigma^+ = \begin{pmatrix} 0 & 1 \\ 0 & 0 \end{pmatrix}, \qquad \sigma^- = \begin{pmatrix} 0 & 0 \\ 1 & 0 \end{pmatrix} \tag{1.14}$$

acting on the k-th site. The Bethe ansatz for the expansion coefficients in (1.13) is a superposition of plane waves [24],

$$\psi(n_1, n_2, \ldots, n_N) = \frac{1}{\sqrt{\mathcal{N}}} \sum_P A(P) \exp\left[i \left(k_{P_1} n_1 + k_{P_2} n_2 + \cdots + k_{P_N} n_N\right)\right], \tag{1.15}$$

where $k_1, \ldots, k_N$ are wave numbers that parametrize the eigenstate, and the sum over P is the sum over all permutations of N labels. The real number $\mathcal{N}$ sets the norm to 1. The coefficients $A(P)$ are [24]

$$A(P) = (-1)^{\sigma(P)} \prod_{j=1}^{N} \prod_{k=j+1}^{N} \left\{\exp\left[i\left(k_{P_j} + k_{P_k}\right)\right] + 1 - 2\Delta \exp\left[i k_{P_j}\right]\right\}, \tag{1.16}$$

where $\sigma(Q)$ is the inversion number of permutation Q. Working with this ansatz is considerably simplified by Orbach's parametrization, which introduces rapidity

parameters λ_j instead of the wave numbers k_j. For $\Delta > 1$, the relation between the different parameters is [25]

$$\exp(ik_j) = \frac{\sin(\lambda_j + i\eta/2)}{\sin(\lambda_j - i\eta/2)}, \tag{1.17}$$

where $\eta \equiv \cosh^{-1}(\Delta)$. Using this parametrization, the wave function becomes

$$\psi(n_1, n_2, \ldots, n_n) = \frac{1}{\sqrt{\mathcal{N}}} \sum_P A(P) \prod_{j=1}^{N} \left(\frac{\sin(\lambda_{P_j} + i\eta/2)}{\sin(\lambda_{P_j} - i\eta/2)} \right)^{n_j}, \tag{1.18}$$

with the coefficients $A(P)$ being

$$A(P) = (-1)^{\sigma(P)} \prod_{j=1}^{N} \prod_{k=j+1}^{N} \sin(\lambda_{P_j} - \lambda_{P_k} + i\eta). \tag{1.19}$$

The advantage of this parametrization is that the constraints imposed by periodic boundary conditions can be expressed in an elegant form [25],

$$\left(\frac{\sin(\lambda_j + i\eta/2)}{\sin(\lambda_j - i\eta/2)} \right)^L = \prod_{k \neq j} \frac{\sin(\lambda_j - \lambda_k + i\eta)}{\sin(\lambda_j - \lambda_k - i\eta)}, \quad (j = 1, \ldots N). \tag{1.20}$$

These N equations are the Bethe equations of the XXZ model with $\Delta > 1$. Any eigenstate with periodic boundary conditions will satisfy these equations.

The form of the Bethe ansatz wave function (1.18)–(1.19) is quite complicated. However, in order to develop the thermodynamics or the hydrodynamics of the model, it is not necessary to consider the wave function itself. Instead, it is enough to enumerate energy eigenstates through the set of their rapidity parameters $\boldsymbol{\lambda} = \{\lambda_j\}$, obtained as the solutions to Eqs. (1.20). The energy eigenvalue corresponding to an eigenstate is expressed as a sum over the rapidities describing it,

$$E_{\boldsymbol{\lambda}} = \sum_{j=1}^{N} e_1(\lambda_j), \qquad e_1(\lambda) \equiv \frac{2\sinh^2(\eta)}{\cosh(\eta) - \cos(2\lambda)}. \tag{1.21}$$

The Hamiltonian of the XXZ model is embedded into a set of commuting quasilocal charges $Q_s^{(j)}$, whose eigenvalues are also expressed as a sum over rapidities. We will further elaborate on these charges in Section 1.2.3.

1.2.2 Thermodynamics of the XXZ model

The thermodynamics of the XXZ model at $\Delta > 1$ was explored by Gaudin [26], using the generalization of the Thermodynamic Bethe Ansatz framework developed by Yang and Yang for the Lieb–Liniger model [27]. As mentioned at the end of the previous Section, it is not necessary to consider the wave function itself in order to describe the thermodynamics of the XXZ model. It is enough to enumerate eigenstates using the set of rapidity parameters $\boldsymbol{\lambda}$. In the thermodynamic limit

$L \to \infty, N/L = \text{const.}$, the rapidities are described by the string hypothesis. The string hypothesis for $\Delta > 1$ says that the rapidities are organized into strings of complex numbers centered around the real axis,

$$\boldsymbol{\lambda} \equiv \{\lambda_j\}_{j=1}^{N} = \bigcup_{n=1}^{\infty} \bigcup_{\alpha=1}^{M_n} \left[\bigcup_{\ell=1}^{n} \{\lambda_\alpha^n + i\eta/2\,(n+1-2\ell)\} \right]. \tag{1.22}$$

Here n is the number of rapidities forming a string, and M_n is the number of n-strings consisting of n rapidities. The content of the brackets is called the αth n-string, which is fully described by its real string center λ_α^n.

By using the string hypothesis (1.22), and by taking logarithm, the Bethe equations (1.20) can be written in the form

$$L\theta_n(\lambda_\alpha^n) = 2\pi I_\alpha^n + \sum_{m,\beta \neq m,\alpha} \Theta_{nm}(\lambda_\alpha^n - \lambda_\beta^m), \tag{1.23}$$

where

$$\theta_n(\lambda) \equiv -i \ln \left(\frac{\sin(\lambda + in\eta/2)}{\sin(\lambda - in\eta/2)} \right) = 2 \tan^{-1} \left(\frac{\tan \lambda}{\tanh n\eta/2} \right), \tag{1.24}$$

$$\Theta_{nm}(\lambda) \equiv (1 - \delta_{n,m})\theta_{|n-m|}(\lambda) + \theta_{|n-m|+2}(\lambda) + \cdots + \theta_{n+m-2}(\lambda) + \theta_{n+m}(\lambda). \tag{1.25}$$

The quantum numbers I_α^n are integers for $L - M_n$ odd and half-integers for $L - M_n$ even. The set of quantum numbers $\{I_\alpha^n\}_{n,\alpha=1}^{\infty}$ identifies the eigenstate, therefore it can be used interchangeably with the corresponding set of rapidities.

In order to describe thermodynamics of the quantum system, it is also necessary to treat unoccupied quantum numbers as holes. By defining

$$h_n(\lambda) \equiv \theta_n(\lambda) - \frac{1}{L} \sum_{m,\beta \neq m,\alpha} \Theta_{nm}(\lambda - \lambda_\beta^m), \tag{1.26}$$

the rapidity $\tilde{\lambda}_\alpha^n$ of the α-th n-string hole is given by the solution of

$$h(\lambda_\alpha^n) = \frac{2\pi}{L} J_\alpha^n, \tag{1.27}$$

where J_α^n is the α-th (half-)integer that is not present among the set of n-string quantum numbers $\{I_\alpha^n\}_{\alpha=1}^{\infty}$.

In the thermodynamic limit, it is impossible and unnecessary to enumerate all the string centers λ_α^n individually. Instead, the thermodynamics is described by the densities of string centers in rapidity space, $\rho_n(\lambda)$, which are defined as continuous functions satisfying

$$\rho_n(\tilde{\lambda}_j^n) \sim \frac{1}{L} \frac{1}{\lambda_{j+1}^n - \lambda_j^n}. \tag{1.28}$$

Morover, it is possible to define the density of holes and the density of states by

$$\rho_{\mathrm{h},n}(\tilde{\lambda}_j^n) \sim \frac{1}{L} \frac{1}{\tilde{\lambda}_{j+1}^n - \tilde{\lambda}_j^n}, \qquad \rho_{\mathrm{t},n}(\lambda) \equiv \rho_n(\lambda) + \rho_{\mathrm{h},n}(\lambda) = \frac{1}{2\pi} \frac{d}{d\lambda} h_n(\lambda). \tag{1.29}$$

The Bethe equations (1.23) constrain these densities. By taking the derivative of (1.23) in λ, one obtains the Bethe–Gaudin–Takahashi equations

$$\rho_{\mathrm{t},n}(\lambda) = a_n(\lambda) - \sum_{m=1}^{\infty} [A_{nm} \star \rho_m](\lambda), \tag{1.30}$$

where the special functions are

$$a_n(\lambda) \equiv \frac{1}{2\pi}\frac{d}{d\lambda}\theta_n(\lambda) = \frac{1}{\pi}\frac{\sinh(n\eta)}{\cosh(n\eta)-\cos(2\lambda)}, \tag{1.31}$$

$$\begin{aligned} A_{nm}(\lambda) &\equiv \frac{1}{2\pi}\frac{d}{d\lambda}\Theta_{nm}(\lambda) \\ &= (1-\delta_{n,m})a_{|n-m|}(\lambda) + a_{|n-m|+2}(\lambda) + \cdots + a_{n+m-2}(\lambda) + a_{n+m}(\lambda), \end{aligned} \tag{1.32}$$

and the convolution operator $\star$ is defined as

$$[f \star g](\lambda) \equiv \int_{-\pi/2}^{\pi/2} \mathrm{d}\mu\, f(\lambda-\mu)g(\mu). \tag{1.33}$$

It is also customary to introduce the occupation number $\vartheta_n(\lambda) = \rho_n(\lambda)/\rho_{\mathrm{t},n}(\lambda)$ to describe eigenstates.

The densities $\boldsymbol{\rho}$ describe do not uniquely identify an eigenstate of the Hamiltonian. On the contrary, there is an extensive number of eigenstates corresponding to the same set of densities. The number of such eigenstates is given by the Yang–Yang entropy [27]

$$\begin{aligned} s_{\mathrm{YY}}[\boldsymbol{\rho}] &= \frac{1}{L}\ln(\#\text{ of corresponding eigenstates}) \\ &= \sum_{n=1}^{\infty}\int \mathrm{d}\lambda\, \left[\rho_{\mathrm{t},n}(\lambda)\ln\rho_{\mathrm{t},n}(\lambda) - \rho_n(\lambda)\ln\rho_n(\lambda) - \rho_{\mathrm{h},n}(\lambda)\ln\rho_{\mathrm{h},n}(\lambda)\right]. \end{aligned} \tag{1.34}$$

This functional is interpreted as the thermodynamic entropy of the thermodynamic macrostate described by $\boldsymbol{\rho}$. Despite the large number of eigenstates corresponding to the densities $\boldsymbol{\rho}$, it is accepted that the mean values of local operators is uniquely determined by the densities in the TDL. For example, the density of the energy (1.21) can be expressed as

$$E/L = e[\boldsymbol{\rho}] \equiv \sum_{n=1}^{\infty}\int_{-\pi/2}^{\pi/2} d\lambda \rho_n(\lambda) e_n(\lambda), \tag{1.35}$$

where

$$\begin{aligned} e_1(\lambda) &\equiv \frac{2\sinh^2(\eta)}{\cosh(\eta)-\cos(2\lambda)}. \\ e_n(\lambda) &\equiv \sum_{j=1}^{n} e_1\left(\lambda + \frac{i\eta}{2}(n+1-2j)\right) = \frac{2\sinh(\eta)\sinh(n\eta)}{\cosh(n\eta)-\cos(2\lambda)} \qquad (n>1). \end{aligned} \tag{1.36}$$

The summation in the second line of (1.36) goes over the constituent rapidities forming an n-string with real center λ.

The thermodynamics of the XXZ model at a finite temperature T is described by the free energy density

$$f_T[\boldsymbol{\rho}] = e[\boldsymbol{\rho}] - T s_{\mathrm{YY}}[\boldsymbol{\rho}]. \tag{1.37}$$

If the chain is in thermal equilibrium with a heath bath of temperature T, then its macroscopic behaviour is described by the macrostate $\boldsymbol{\rho}_T = \{\rho_{T,n}(\lambda)\}_{n=1}^{\infty}$ that minimizes (1.37). It is customary to describe $\boldsymbol{\rho}_T$ using the functions

$$\varepsilon_{T,n}(\lambda) \equiv T^{-1} \log(\rho_{\mathrm{T,h},n}(\lambda)/\rho_{T,n}(\lambda)), \tag{1.38}$$

which are the thermal dressed energies (see Section 1.2.4). Using calculus of variations, one finds that the dressed energies satisfy the integral equations [21, 26]

$$\varepsilon_{T,n}(\lambda) = e_n(\lambda) + T \sum_{m=1}^{\infty} [A_{nm} \star (1 + \exp(-\varepsilon_{T,m}/T))](\lambda), \tag{1.39}$$

where the star symbol denotes the convolution (1.33). Once the pseudoenergies are computed, one can use their definition (1.38) and the BGT equations (1.30) to compute the densities $\boldsymbol{\rho}_T$, and the thermal expectation values of observables. The value of the free energy (1.37) can be cast in the simplified form [21]

$$F/L = f_T[\boldsymbol{\rho}_T] = J\Delta - T \sum_{n=1}^{\infty} \int_{-\pi/2}^{\pi/2} d\lambda \, a_n(\lambda) \ln(1 + 1/\eta_{T,n}(\lambda)). \tag{1.40}$$

.

1.2.3 Conserved charges

The XXZ model features an infinite number of mutually commuting quasi-local conserved operators. Later we will see that the existence of infinitely many such operators, a common feature in integrable systems, has a definitive effect on their non-equilibrium behaviour. Now we summarize the construction [22, 28, 29] of these charges in the XXZ model at $\Delta > 1$.

First, let us consider a Hilbert space $\mathcal{V}_s = \mathbb{C}^{2s+1}$, where s is integer or half-integer. The basis in this space consists of the vectors $|m\rangle$, with the range of the (half-)integers m being $s, s-1, \ldots, -s$. In this auxiliary space, the spin-s representation of the q-deformed $\mathcal{U}_q(\mathfrak{sl}(2))$ algebra is

$$\begin{aligned} S_a^{\pm}|m\rangle &= \sqrt{[s+1 \pm m]_q [s \mp m]_q}\,|m \pm 1\rangle, \\ S_a^{z}|m\rangle &= m|m\rangle, \end{aligned} \tag{1.41}$$

where $[x]_q = (q^x - q^{-x})/(q - q^{-1})$. These matrices satify the $\mathcal{U}_q(\mathfrak{sl}(2))$ algebra

$$[S_a^+, S_a^-] = [2S^z]_q, \qquad q^{2S^z} S^{\pm} = q^{\pm 2} S^{\pm} q^{2S^z}. \tag{1.42}$$

Using the representation (1.41), one can define L-operators acting in $\mathbb{C}^2 \otimes \mathcal{V}_s$ as

$$L_a(\lambda) \equiv \frac{1}{\sinh(\lambda + i\eta)} \begin{pmatrix} \sinh(\lambda + i\eta S_a^z) & i \sinh(\eta) S_a^- \\ i \sinh(\eta) S_a^+ & \sinh(\lambda + i\eta S_a^z) \end{pmatrix}, \tag{1.43}$$

where $S_a^{\pm,z}$ acts in the auxiliary space $\mathcal{V}_s$ Using the L-matrices, one can define the transfer matrices

$$t_s(\lambda) \equiv \mathrm{Tr_a}\, L_{a,L}(\lambda) L_{a,L-1}(\lambda) \dots L_{a,1}(\lambda), \qquad (\mathcal{V}_a = \mathbb{C}^{2s+1}), \tag{1.44}$$

where $L_{a,k}(u)$ acts on the k-th site of the physical spin chain. The transfer matrices (1.44) commute with each other, satisfying [22, 28, 29]

$$[t_s(\lambda), t_{s'}(\lambda')] = 0. \tag{1.45}$$

They correspond to the XXZ Hamiltonian by the derivative

$$H_{\mathrm{XXZ}} = -2i \sinh \eta \, \frac{d}{d\lambda} \log t_{1/2}(\lambda)\Big|_{\lambda = i\eta/2}. \tag{1.46}$$

Because of the commutation property (1.45), the expansion coefficients of $t_s(\lambda)$ in λ are commuting matrices. One can consider the matrices obtained by the expansion of the logarithm around $\lambda = \eta/2$ [29],

$$Q_s^{(j)} = (-i)^{j-1} \frac{d^{j-1}}{d\lambda^{j-1}} \log t_s(\lambda)\Big|_{\lambda = i\eta/2}. \tag{1.47}$$

These charges have the properties

$$[Q_r^{(j)}, Q_s^{(k)}] = 0, \qquad Q_{1/2}^{(2)} = \frac{1}{2 \sinh \eta} H_{\mathrm{XXZ}}. \tag{1.48}$$

For $s = 1/2$ these charges are local, i.e., in the thermodynamic limit they have the form

$$Q_{1/2}^{(j)} = \sum_{j=-\infty}^{\infty} \mathcal{T}_r \sum_{k=1}^{K} \mathcal{Q}_{1/2,k}^{(j)}, \tag{1.49}$$

where $\mathcal{T}_j$ is the j-site translation operator, $\mathcal{Q}_{1/2,k}^{(j)}$ is an operator that is acting non-trivially (i.e., not as the identity operator) on k neighboring sites, and K is a finite integer. For $s > 1/2$, the charges in (1.47) are quasi-local, i.e., their form is

$$Q_s^{(j)} = \sum_{j=1}^{\infty} \mathcal{T}_j \sum_{k=1}^{\infty} \mathcal{Q}_{s,k}^{(j)}, \qquad (s > 1/2), \tag{1.50}$$

where $\mathcal{Q}_{s,k}^{(j)}$ acts non-trivially on k neighboring sites, and its norm satisfies [29]

$$||\mathcal{Q}_{s,k}^{(j)}||_{\mathrm{HS}} < C e^{-\xi k}, \qquad (C > 0,\, \xi > 0), \tag{1.51}$$

where the Hilbert–Schmidt norm is defined as $||A||^2_{\mathrm{HS}} = \mathrm{Tr}\, A^\dagger A$.

Since the conserved charges (1.47) commute with the Hamiltonian, the Bethe ansatz states (1.18) are simultaneously eigenstates of all conserved charges. In the thermodynamic limit $L \to \infty$, $N/L = \text{const.}$, the density expectation values of both local and quasi-local conserved charges can be expressed, similarly to the energy (1.35), with integrals [29]

$$Q_s^{(j)}/L = q_s^{(j)}[\boldsymbol{\rho}] \equiv \sum_{n=1}^{\infty} \int_{-\pi/2}^{\pi/2} d\lambda \rho_n(\lambda) q_{s,n}^{(j)}(\lambda), \tag{1.52}$$

where the density kernel for unbound states is

$$q_{s,1}^{(j)} = \left(-i\frac{d}{d\lambda}\right)^j \ln\left(\frac{\sin(\lambda + is\eta)}{\sin(\lambda - is\eta)}\right), \tag{1.53}$$

and the density kernel for bound states is

$$q_{s,n}^{(j)} = \sum_{k=1}^{n} q_s^{(j)}(\lambda + i\eta/2(n+1-2k)). \tag{1.54}$$

Here the sum is over the constituent rapidities (1.22) of the bound state. As a consequence of (1.48), the density kernels satisfy $2\sinh(\eta) q_{1/2,n}^{(1)}(\lambda) = e_n(\lambda)$.

An important conserved charge of the XXZ model is the total momentum P. From the form (1.18) of the Bethe ansatz solution, one can see that in a finite system the total momentum satisfies

$$\langle \boldsymbol{\lambda} | e^{iP} | \boldsymbol{\lambda} \rangle = \langle \boldsymbol{\lambda} | \mathcal{T}_1 | \boldsymbol{\lambda} \rangle = \prod_j \left(\frac{\sin(\lambda_j + i\eta/2)}{\sin(\lambda_j - i\eta/2)}\right), \tag{1.55}$$

where $\mathcal{T}_1$ is the one-site translation operator. As a consequence, in the thermodynamic limit the total momentum formally satisfies (modulo 2π)

$$P = Lp[\boldsymbol{\rho}] \equiv L \sum_{n=1}^{\infty} \int_{-\pi/2}^{\pi/2} d\lambda \rho_n(\lambda) p_n(\lambda), \tag{1.56}$$

where $p_n(\lambda) = \theta_n(\lambda)$, and $\theta_n(\lambda)$ is defined in (1.24).

1.2.4 Quasiparticles, dressed charges, velocities

An eigenstate of the XXZ model, described by the string densities $\boldsymbol{\rho}$, can be interpreted as a collection of stable quasiparticles. Each n-string is associated with a quasiparticle that propagates linearly with an effective velocity $v_n(\lambda)$ [30]. This interpretation is important in the development of the hydrodynamics of the XXZ model, as discussed in Chapter 1.4.

The velocity of the quasiparticles is defined using the notion of dressed charge. Let us consider an eigenstate of the XXZ chain, characterized by the set of quantum numbers $\{I_\alpha^n\}$. If a new particle is added to the system with the (previously

unoccupied) quantum number I_β^m, then the rapidities of the other particles will be shifted from $\{\lambda_\alpha^n\}$ to $\{\tilde{\lambda}_\alpha^n\}$. Let us denote the rapidity of the new particle by μ_β^m. By the addition of the particle, the expectation value of a conserved charge will change by

$$\begin{aligned}\langle\tilde{\boldsymbol{\lambda}},\,\mu_\beta^m|Q_s^{(j)}|\tilde{\boldsymbol{\lambda}},\,\mu_\beta^m\rangle-\langle\boldsymbol{\lambda}|Q_s^{(j)}|\boldsymbol{\lambda}\rangle&=q_s^{(j)}(\mu_\beta^m)+\sum_n\sum_{\alpha=1}^{N_n}\left(q_s^{(j)}(\tilde{\lambda}_\alpha^n)-q_s^{(j)}(\lambda_\alpha^n)\right)\\&\equiv q_s^{(j)\,\mathrm{dr}}(\mu_\beta^n).\end{aligned}\tag{1.57}$$

In this formula, $q_s^{(j)}(\mu_\beta^m)$ is the bare charge (1.53), which would be associated with the quasiparticle I_β^m if no other particles were present. However, the addition of the rapidity μ_β^m also shifts the other rapidities from λ_α^n to $\tilde{\lambda}_\alpha^n$, and an additional contribution to the total charge occurs, reflected by the double sum in (1.57). In other words, the additional charge $q_s^{(j)}(\mu_\beta^m)$ is dressed by the other quasiparticles, resulting in the dressed charge $q_s^{(j)\,\mathrm{dr}}(\mu_\beta^m)$.

In the thermodynamic limit, the dressed charge of an additional n-string quasiparticle can be obtained by solving the linear equations [31, 32]

$$q_{s,n}^{(j)\,\mathrm{dr}}(\mu)=q_{s,n}^{(j)\prime}(\mu)-\sum_m[A_{nm}\star\vartheta_m q_{s,m}^{(j)\,\mathrm{dr}}](\mu),\tag{1.58}$$

where the filling fraction is introduced as

$$\vartheta_n(\lambda)\equiv\frac{\rho_n(\lambda)}{\rho_{\mathrm{t},n}(\lambda)}.\tag{1.59}$$

Similarly to (1.58), one can compute the dressed energy $e_n^{\mathrm{dr}}(\mu)$ of the quasiparticle by solving

$$e_n^{\mathrm{dr}}(\mu)=e_n'(\mu)-\sum_m[A_{nm}\star\vartheta_m e_m^{\mathrm{dr}}](\mu).\tag{1.60}$$

The dressed momentum is instead described by

$$p_n^{\mathrm{dr}}(\mu)=2\pi a_n(\mu)-\sum_m[A_{nm}\star\vartheta_m p_m^{\mathrm{dr}}](\mu),\tag{1.61}$$

where the fact $p_n'(\lambda)=2\pi a_n(\lambda)$ was used. By comparing (1.61) with (1.30), one concludes that $p_n^{\mathrm{dr}}(\mu)=2\pi\rho_{\mathrm{t},n}(\mu)$.

The effective velocity of an n-string quasiparticle is defined as [30–32]

$$v_n(\lambda)\equiv\frac{\partial e_n^{\mathrm{dr}}(\lambda)}{\partial p_n^{\mathrm{dr}}(\lambda)}=\frac{e_n^{\mathrm{dr}\prime}(\lambda)}{p_n^{\mathrm{dr}\prime}(\lambda)}.\tag{1.62}$$

Using the definitions (1.60) and (1.61), a system of equations can be derived for the effective velocity, which reads [30, 31]

$$\rho_{\mathrm{t},n}(\lambda)v_n(\lambda)=\frac{e_n'(\lambda)}{2\pi}-\sum_{m=1}^{\infty}[A_{nm}\star\rho_m v_m](\lambda).\tag{1.63}$$

We note that the effective velocity is different from the bare velocity $v_n^{\rm bare}(\lambda) = e_n'(\lambda)/p_n'(\lambda)$. As it will be discussed in Section 1.4, $v_n(\lambda)$ is the velocity of the stable quasiparticles that appear in the hydrodynamic description of the integrable systems. By using the BGT equations (1.30), it is also possible to write (1.63) in the alternative, equivalent form

$$v_n(\lambda) = v_n^{\rm bare}(\lambda) + \sum_m \int_{-\pi/2}^{\pi/2} d\mu \, \frac{A_{nm}(\lambda-\mu)}{\rho_n(\lambda)} \rho_m(\mu)(v_n(\lambda) - v_m(\mu)) \,. \tag{1.64}$$

This form of the equation has an intuitive interpretation in terms of scattering quasiparticles, which will be discussed in Chapter 4.

1.3 Global quantum quenches in integrable systems

Let us now consider the paradigmatic non-equilibrium scenario, the global quantum quench in homogeneous integrable systems. The system is initially prepared in a translationally invariant initial state $|\Psi_0\rangle$, and it is evolved by an integrable Hamiltonian as

$$|\Psi(t)\rangle = e^{-iHt}|\Psi_0\rangle. \tag{1.65}$$

We have seen in Section 1.1 that in the long time limit the system cannot thermalize globally, since it remains in a pure state. Instead, we are interested in describing the limit

$$\lim_{T\to\infty} \lim_{L\to\infty} \frac{1}{T} \int_0^t dt \, \langle \Psi_0 | e^{iHt} O e^{-iHt} | \Psi_0 \rangle \tag{1.66}$$

of expectation values of local operators O with an appropriate ensemble. In a generic non-integrable system they would be described by the Gibbs ensemble (1.2) but this ensemble fails to take into consideration the infinite number of conservation laws (1.10). There are two complementary approaches to overcome this problem. On one hand, the Generalized Gibbs Ensemble [17] works by including all the quasilocal conserved operators in the density matrix. On the other hand, the Quench Action approach [33] explicitly computes expectation values in the diagonal ensemble (1.9).

1.3.1 Generalized Gibbs Ensemble

The Generalized Gibbs Ensemble has been studied in diverse free quantum systems [34–42], interacting quantum gases [43–47], integrable quantum chains [48–65] and quantum field theories [66–72]. For the sake of simplicity, let us now concentrate on the XXZ model, whose quasi-local conserved charges are given by (1.47). The Generalized Gibbs Ensemble [17] takes into consideration these conservation laws by including them in the density matrix

$$\rho_{\rm GGE} = \frac{1}{Z_{\rm GGE}} e^{-\sum_{s,j} \beta_s^{(j)} Q_s^{(j)}}, \qquad Z_{\rm GGE} = {\rm Tr}\, e^{-\sum_{s,j} \beta_s^{(j)} Q_s^{(j)}}, \tag{1.67}$$

and setting $\beta_s^{(j)}$ such that the conservation laws are satisfied,

$$\operatorname{Tr} \rho_{\mathrm{GGE}}\, Q_s^{(j)} = \langle \Psi_0 | Q_s^{(j)} | \Psi_0 \rangle. \tag{1.68}$$

In (1.67) the indices s go over all integers and half-integers, while the indices j go over all integers. It has been observed that it is important to include all the local and quasilocal charges into the ensemble in order to get correct predictions for the expectation values of local observables [55–60, 73].

Similarly to the Gibbs ensemble describing thermal equilibrium, the trace in the expectation values can be expressed as a functional integral over all thermodynamic macrostates

$$\operatorname{Tr} \frac{1}{Z_{\mathrm{GGE}}} e^{-\sum_{s,j} \beta_s^{(j)} Q_s^{(j)}} \sim \int D[\boldsymbol{\rho}]\, e^{-L \sum_{s,j} \beta_s^{(j)} q_s^{(j)}[\boldsymbol{\rho}] + L\, s_{YY}[\boldsymbol{\rho}]}, \tag{1.69}$$

where $q_s^{(j)}[\boldsymbol{\rho}]$ is the charge expectation value (1.52) and $s_{\mathrm{YY}}[\boldsymbol{\rho}]$ is the Yang–Yang entropy (1.34) enumerating the states with density $\boldsymbol{\rho}$. On the right-hand side the partition sum Z_{GGE} is incorporated into the functional measure. Due to $L \to \infty$ the functional integral can be computed by saddle-point analysis. The thermodynamic properties are described by the representative state $\boldsymbol{\rho}_\beta$ for which

$$\delta f_{\mathrm{GGE}}[\boldsymbol{\rho}]\Big|_{\boldsymbol{\rho}_\beta} \equiv \delta \left(\sum_{s,j} \beta_s^{(j)} q_s^{(j)}[\boldsymbol{\rho}] - \, s_{YY}[\boldsymbol{\rho}] \right) \Bigg|_{\boldsymbol{\rho}_\beta} = 0. \tag{1.70}$$

By variational calculus and the use of the BGT equations, one can derive the system describing $\boldsymbol{\rho}_\beta$, which is

$$\ln \eta_{\boldsymbol{\beta},n}(\lambda) = g_n(\lambda) + \sum_{m=1}^{\infty} A_{nm} \star \ln[1 + 1/\eta_{\boldsymbol{\beta},m}](\lambda), \tag{1.71}$$

where

$$g_n(\lambda) = \sum_{s,j} \beta_s^{(j)} q_{s,n}^{(j)}(\lambda). \tag{1.72}$$

The information about the saddle-point root densities is now encoded in the functions $\eta_{\boldsymbol{\beta},n} \equiv \rho_{\mathrm{h},n}(\lambda)/\rho_n(\lambda)$. Once $\eta_{\boldsymbol{\beta},n}(\lambda)$ are known, the root densities themselves can be found using the BGT equations (1.30). The densities then determine the expectation values of local observables. In particular, the expectation values of the conserved charges can be computed using the integral formulas (1.52), and correlation functions can be computed using their factorization properties [74–84].

Let us note that, the usage of the GGE as described above is problematic because the number of quasi-local charges is infinite, and therefore it is impossible to determine the value of $\beta_s^{(j)}$ from the conservation laws (1.68). This difficulty can be overcome using the string–charge duality which is a linear relation between the expectation values of conserved charges and the string densities [85]. Using this duality, the steady state values $\eta_{\boldsymbol{\beta},n}$ have been computed in the spin-1/2 XXZ model for several initial states, including the dimer [85], the tilted Néel and tilted ferromagnetic [62] states.

1.3.2 The Quench Action

An alternative method of determining the long-time limit (1.66) of expectation values is the Quench Action approach [33, 86], which has been used to describe the relaxed state in diverse lattice systems [33, 55–58, 87–89] and quantum gases [45, 90–92]. This approach uses a straightforward computation of averages in the diagonal ensemble (1.9)

$$\rho_{\mathrm{DE}} = \sum_n \left(|\langle n|\Psi_0\rangle|^2 \right) |n\rangle\langle n|. \tag{1.73}$$

The main obstacle in working with this ensemble is the knowledge of the overlaps $|\langle\Psi_0|n\rangle|^2$. For specific translationally invariant states $|\Psi_0\rangle$ these overlaps can be computed analytically. Since $|\Psi_0\rangle$ is translationally invariant, the overlaps are nonzero only with translationally invariant Bethe states, which have the form $\boldsymbol{\lambda} = \{\pm\lambda_j\}_{j=1}^{L/2}$. For specific initial states the overlaps can be written in the form

$$-\ln\left(|\langle\Psi_0|\boldsymbol{\rho}\rangle|\right)/L \equiv \mathcal{E}[\boldsymbol{\rho}] = \sum_{n=1}^{\infty} \int_{-\pi/2}^{\pi/2} d\lambda \rho_n(\lambda) d_{\Psi_0,n}(\lambda), \tag{1.74}$$

where $d_{\Psi_0,1}(\lambda)$ is a known function depending on the initial state, and

$$d_{\Psi_0,n}(\lambda) = \sum_{k=1}^{n} d_{\Psi_0,1}\left(\lambda + \frac{i\eta}{2}(n+1-2k)\right), \qquad (n \geq 2). \tag{1.75}$$

In the spin-1/2 XXZ model, such formulas have been derived for the class of these integrable initial states [93], which include the Néel [94, 95], the dimer [57, 58] and the q-dimer [58] initial states.

The integral formula (1.74) allows one to express ensemble averages of the diagonal ensemble (1.74) as functional integrals [33],

$$\mathrm{Tr}\,\rho_{\mathrm{DE}} O \sim \int D[\boldsymbol{\rho}] e^{-L(2\mathcal{E}[\boldsymbol{\rho}] - s_{YY}[\boldsymbol{\rho}]/2)} O[\boldsymbol{\rho}], \tag{1.76}$$

where $O[\boldsymbol{\rho}] \equiv \langle\boldsymbol{\rho}|O|\boldsymbol{\rho}\rangle$. The factor 1/2 before the Yang–Yang entropy takes into consideration that the microscopic form of the overlapping states is $\boldsymbol{\lambda} = \{\pm\lambda_j\}_{j=1}^{L/2}$, therefore only positive quantum numbers are freely chosen in the microscopic state. Working in the thermodynamic limit, the functional integral (1.76) can be computed using saddle point analysis, which is analogous to the thermal case (1.39). A representative state $\boldsymbol{\rho}^*$ describes the state of the system that satisfies [33, 55]

$$\ln\eta_n^*(\lambda) = d_{\Psi_0,n}(\lambda) + \sum_{m=1}^{\infty} A_{nm} \star \ln[1 + 1/\eta_m^*](\lambda), \tag{1.77}$$

where the information about $\boldsymbol{\rho}^*$ is encoded in the functions $\eta_n^*(\lambda) = \rho_{\mathrm{h},n}^*(\lambda)/\rho_n^*(\lambda)$. Once (1.77) is solved for η^*, the root densities can be found by solving the BGT equations (1.30). The root densities are then used to express the expectation values of local observables in the relaxed state after the quench. We note that the Quench Action saddle point densities $\boldsymbol{\rho}^*$ are the same as the GGE saddle point state $\boldsymbol{\rho}_\beta$, since they describe the same stationary state after the same quench.

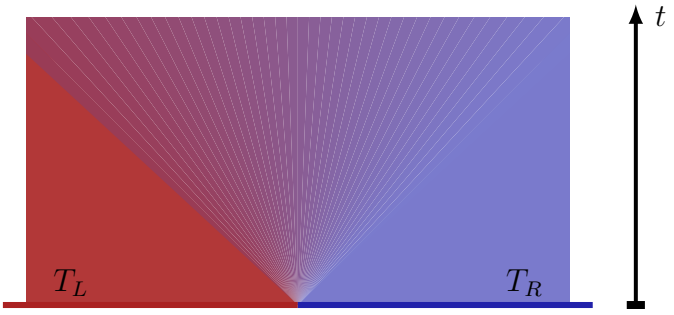

Figure 1.1: Pictorial representation of the bipartite thermal quench protocol. After the sudden junction of the two halves in two thermal states at temperatures T_L and T_R a non-trivial light-cone region emerges from the junction.

1.4 Generalized Hydrodynamics

In the previous Section we have considered the behaviour of integrable systems after quenching them from *homogeneous* initial states. Now let us consider the behaviour of the system after quenching from an *inhomogeneous* initial state. At large space-time scales, slowly and smoothly varying integrable systems are described by the Generalized Hydrodynamics (GHD) approach [31, 32]. This approach has been used to describe the ballistic transport properties of diverse quantum [31, 32, 96–110] and classical [111–117] integrable systems. It has also been experimentally verified in a recent cold atomic experiment [118].

In this Thesis we focus on hydrodynamics at the Euler scale $x \sim t$, where transport is described by ballistically propagating quasiparticles. However, in interacting integrable systems, diffusive and superdiffusive corrections to the ballistic picture arise at scales $x \sim t^\alpha$ with $\alpha < 1$. These phenomena have been the subject of intense research in recent years [119–132].

In order to summarize the GHD approach, let us consider a bipartite integrable system with a Hilbert space $\mathcal{H} = \mathcal{H}_{\rm L} \otimes \mathcal{H}_R$, in the bipartite initial state

$$\rho_0 = \frac{1}{Z}\left(e^{-\beta_L H_L} \bigotimes e^{-\beta_R H_R}\right) . \tag{1.78}$$

Here H_L and H_R are integrable Hamiltonians, such as the XXZ Hamiltonian (1.46) acting on $\mathcal{H}_{\rm L}$ and $\mathcal{H}_R$. At $t = 0$ the system is released and evolves according to

$$\rho(t) = e^{-iHt}\rho_0 e^{iHt}, \tag{1.79}$$

where H is an integrable Hamiltonian acting on $\mathcal{H}$. This evolution is depicted on Figure 1.1.

At large space-time scales, the evolution (1.79) can be described by the Generalized Hydrodynamics (GHD) approach [31, 32]. This approach is based on the existence of an infinite amount of quasilocal conserved charges in the integrable

model, such as the charges of the XXZ model (1.47). These charges fulfil continuity equations

$$\partial_t q_k(x,t) + \partial_x j_k(x,t) = 0, \tag{1.80}$$

where the operator $q_k(x,t)$ is the density of charge k, and the operator $j_k(x,t)$ is the current density associated to the charge. In the long time limit, the state of the system after a bipartite quench (1.78) is slowly varying in space time. Therefore the system can be divided into small cells in space, and in each cell it is described by a quasi-stationary GGE (called a Local Quasi-Stationary State). Thus (1.80) can be written as an equation for expectation values

$$\partial_t \langle q_k(x,t)\rangle_{\boldsymbol{\beta}(x,t)} + \partial_x \langle j_k(x,t)\rangle_{\boldsymbol{\beta}(x,t)} = 0, \tag{1.81}$$

where $\langle . \rangle_{\boldsymbol{\beta}(x,t)}$ is the expectation value in the local GGE described by the Lagrange multipliers $\boldsymbol{\beta}(x,t)$.

The expectation values of the charges appearing in (1.81) can be expressed using the integral formula

$$\langle q_k\rangle_{\boldsymbol{\beta}} = q_k[\boldsymbol{\rho}_{\boldsymbol{\beta}}] = \sum_n \int_{-\infty}^{\infty} \mathrm{d}\lambda\, \rho_{n,\boldsymbol{\beta}}(\lambda)\, q_{k,n}(\lambda) \tag{1.82}$$

where $q_{j,n}(\lambda)$ is the charge density function and $\rho_{n,\boldsymbol{\beta}}(\lambda)$ is the particle density of different bound states in the GGE saddle point state. For example, in the XXZ model, the density is given by Eq. (1.53)–(1.54), and the GGE saddle point is described by the equations (1.71). The integral formula (1.82) is a direct consequence of the integrable structure of the model.

The expectation values of the currents in (1.81) are somewhat more complicated. At the Euler scale $x \sim t$, they are given by the formula [31, 32]

$$\langle j_k\rangle_{\boldsymbol{\beta}} = j_k[\boldsymbol{\rho}_{\boldsymbol{\beta}}] = \sum_n \int_{-\infty}^{\infty} \mathrm{d}\lambda\, v_{n,\boldsymbol{\beta}}(\lambda)\rho_{n,\boldsymbol{\beta}}(\lambda)\, q_{k,n}(\lambda) \tag{1.83}$$

where $v_{n,\boldsymbol{\beta}}$ are the effective velocities of quasiparticles in the macrostate described by $\boldsymbol{\rho}_{\boldsymbol{\beta}}$. In the XXZ model, they are given as the solution to the equations (1.63) with $\boldsymbol{\rho} = \boldsymbol{\rho}_{\boldsymbol{\beta}}$. While the formula (1.83) has a clear intuitive interpretation (which becomes apparent by comparing it to (1.82)), it has not been proved in general. Analytical proofs exist relativistic integrable field theories [133], and in the XXZ model [134], while in the Lieb–Liniger model there are intuitive arguments [32]. In the rest of this Thesis, we suppose that this formula works in any Bethe ansatz solvable model.

Substituting the averages in (1.81) with (1.82) and (1.83), and using that the functions $q_{j,n}(\lambda)$) form a one obtains the continuity equation for the root densities [31, 32]

$$\partial_t \rho_{n;x,t}(\lambda) + \partial_x(\rho_{n;x,t}(\lambda) v_{n;x,t}(\lambda)) = 0, \tag{1.84}$$

where $\boldsymbol{\rho}_{x,t}$ is the set of root densities describing the local quasi-stationary state at x,t described by GGE Lagrange multipliers $\boldsymbol{\beta}_{x,t}$. The existence of the continuity

equation (1.84) for the root density of each mode is the defining characteristics of Generalized Hydrodynamics.

In the special case of the bipartite quench (1.78) (see also Fig. 1.1), physical quantities depend on the ray $\zeta = x/t$, because of the existence of stable quasiparticles in integrable systems. Therefore the continuity equation (1.84) can be rewritten as [31]

$$\zeta \partial_\zeta \rho_{n,\zeta}(\lambda) - \partial_\zeta(\rho_{n,\zeta}(\lambda) v_{n,\zeta}(\lambda)) = 0. \tag{1.85}$$

The normal modes of these equations are the occupation numbers

$$\vartheta_{n;\zeta}(\lambda) \equiv \rho_{n;\zeta}(\lambda)/\rho_{\mathrm{t},n;\zeta}(\lambda), \tag{1.86}$$

which satisfy [31]

$$(\zeta - v_{n,\zeta}(\lambda))\partial_\zeta \vartheta_{n,\zeta}(\lambda) = 0. \tag{1.87}$$

These equations have the implicit solution [31]

$$\vartheta_{n,\zeta}(\lambda) = \begin{cases} \vartheta_{\mathrm{L}}(\lambda), & \text{if } \zeta <= v_{n,\zeta}(\lambda), \\ \vartheta_{\mathrm{R}}(\lambda), & \text{if } \zeta > v_{n,\zeta}(\lambda), \end{cases} \tag{1.88}$$

where $\vartheta_{\mathrm{L}}(\lambda)$ and $\vartheta_{\mathrm{R}}(\lambda)$ are the thermal occupation numbers on the left and the right in the initial state (1.78). This solution is implicit, because $v_{n,\zeta}(\lambda)$ depend on $\vartheta_{n,\zeta}(\lambda)$. It can be solved by numerical iteration. Once the occupation numbers are known, the BGT equations (1.30) can be used to compute the root densities $\rho_{n;\zeta}(\lambda)$, which in turn determine the spatio-temporal profiles of observables. See Fig. 5.1 for an example of the particle density profiles.

Chapter 2

Rényi entropy of macrostates in generic integrable systems

In this Chapter we will have a closer look at the Generalized Gibbs Ensemble describing stationary or quasi-stationary states of integrable systems. We devise a generic method for computing the Rényi entropies of this ensemble. This method works not only with the GGE describing a post-quench relaxed state, but in principle with any thermodynamic macrostate of an integrable system.

In order to define Rényi entropies, let us repeat that the density matrix of the GGE is

$$\rho_{\rm GGE} = \frac{1}{Z_{\rm GGE}} e^{-\sum_{s,j}\beta_s^{(j)} Q_s^{(j)}}, \qquad Z_{\rm GGE} = {\rm Tr}\, e^{-\sum_{s,j}\beta_s^{(j)} Q_s^{(j)}}, \tag{2.1}$$

where $Q_s^{(j)}$ are the local and quasi-local conserved charges. For example, in the XXZ model, the charges are given by (1.47). The Lagrange multipliers $\beta_s^{(j)}$ fix the GGE expectation values of the charges to the correct values. Then Rényi entropies of the GGE density matrix are

$$S^{(\alpha)}_{\rm GGE} \equiv \frac{1}{1-\alpha} \ln\, {\rm Tr}\, \rho^\alpha_{\rm GGE}, \tag{2.2}$$

where the parameter α is a positive real number. The $\alpha \to 1$ limit is the von Neumann entropy

$$S_{\rm GGE} \equiv -{\rm Tr}\, \rho_{\rm GGE} \ln \rho_{\rm GGE}, \tag{2.3}$$

whose density is given by the Yang–Yang entropy $s_{\rm YY}[\boldsymbol{\rho}_\beta]$ of the GGE saddle point state (1.70)–(1.72). In view of this fact, the Rényi entropies can be interpreted as a generalization of the von Neumann entropy, containing much more information about a thermodynamic ensemble.

2.1 TBA approach for the stationary Rényi entropies

Our method for computing Rényi entropies is related to a recently developed approach based on the Thermodynamic Bethe Ansatz, which yields Rényi entropies

in the steady state at long time after a quantum quench [135, 136]. We begin by revising these results and extending them to new initial states.

Specifically, we consider quantum quenches of the XXZ model. By a global quantum quench in the XXZ model, we mean preparing the system in an initial state $|\Psi_0\rangle$, and evolving it according to the XXZ Hamiltonian (1.11) as

$$|\Psi(t)\rangle = e^{-iH_{\rm XXZ}t}|\Psi_0\rangle. \tag{2.4}$$

As we have seen in the Introduction, the long-time limit of the macroscopically large system will be described by a GGE.

2.1.1 General procedure for computing the Rényi entropy

The Rényi entropies of a post-quench relaxed state can be computed by a saddle-point analysis similar to the saddle-point analysis (1.70) describing local observables. After plugging (2.1) into (2.2), the Renyi entropies read

$$S^{(\alpha)}_{\rm GGE} = \frac{1}{1-\alpha}\left[\ln {\rm Tr}\, \exp\left(-\alpha\sum_{s,j}\beta^{(j)}_s Q^{(j)}_s\right) - \alpha \ln Z_{\rm GGE}\right]. \tag{2.5}$$

The trace over the eigenstates in (2.5) in the thermodynamic limit is replaced by a functional integral over the TBA densities ρ_n as

$${\rm Tr} \to \int D[\boldsymbol{\rho}] e^{L s_{YY}[\boldsymbol{\rho}]}, \tag{2.6}$$

Here the Yang-Yang entropy takes into account the number of microscopic eigenstates corresponding to the same thermodynamic state. The Rényi entropies (2.5) are then given by the functional integral [135, 136]

$$S^{(\alpha)}_{\rm GGE} = \frac{1}{1-\alpha}\left[\ln \int D[\boldsymbol{\rho}] \exp\left(-\alpha L \mathcal{E}[\boldsymbol{\rho}] + L s_{\rm YY}[\boldsymbol{\rho}]\right) + \alpha L f_{\rm GGE}\right]. \tag{2.7}$$

Here we introduce the pseudoenergy $\mathcal{E}[\boldsymbol{\rho}]$ as

$$\mathcal{E}[\boldsymbol{\rho}] \equiv \sum_{s,j}\beta^{(j)}_s \sum_n \int {\rm d}\lambda \rho_n(\lambda) q^{(j)}_{s,n}(\lambda), \tag{2.8}$$

where $q^{(j)}_{s,n}$ are defined in (1.53)–(1.54). (In the case of the standard Gibbs ensemble the sum includes only the energy $q^{(2)}_{1/2,n}(\lambda)$ coupled with the inverse temperature $\beta^{(2)}_{1/2}$.) The quantity $f_{\rm GGE}$ is the GGE grand canonical potential defined as

$$f_{\rm GGE} = -\ln Z_{\rm GGE}/L. \tag{2.9}$$

Similarly to the description of local observables, the functional integral in (2.7) can be evaluated using the saddle-point method [135, 136]. The integral is expressed using the saddle-point $\boldsymbol{\rho}^{(\alpha)}$ that satisfies

$$\delta\left(\mathcal{S}^{(\alpha)}_{\rm GGE}[\boldsymbol{\rho}]\right)\Big|_{\boldsymbol{\rho}=\boldsymbol{\rho}^{(\alpha)}} \equiv \delta\left(-\alpha L\mathcal{E}[\boldsymbol{\rho}] + L s_{\rm YY}[\boldsymbol{\rho}]\right)\Big|_{\boldsymbol{\rho}=\boldsymbol{\rho}^{(\alpha)}} = 0. \tag{2.10}$$

The functional $\mathcal{S}^{(\alpha)}_{\rm GGE}[\boldsymbol{\rho}]$ is explicitly dependent on the Rényi index α. For $\alpha = 1$, Eq. (2.10) provides the macrostate $\boldsymbol{\rho}_\beta$ (1.70) which describes local and quasi-local properties of the steady state and the von Neumann entropy. The minimisation procedure gives a set of coupled integral equations for the macrostate densities $\boldsymbol{\rho}^{(\alpha)}$. These are conveniently written in terms of a set of functions $\eta^{(\alpha)}_n(\lambda) = \rho^{(\alpha)}_{{\rm h},n}(\lambda)/\rho^{(\alpha)}_n(\lambda)$, where α is the index of the Renyi entropy. Specifically, the saddle point condition on (2.10) yields the equations

$$\ln \eta^{(\alpha)}_n = \alpha g_n + \sum_{m=1}^{\infty} A_{nm} \star \ln[1 + 1/\eta^{(\alpha)}_m], \tag{2.11}$$

where $A_{nm}(\lambda)$ is defined in (1.32), and the TBA driving function $g_n(\lambda)$ is defined as

$$g_n(\lambda) \equiv \sum_{s,j} \beta^{(j)}_s q^{(j)}_{s,n}(\lambda). \tag{2.12}$$

Here $q^{(j)}_{s,n}(\lambda)$ are the functions expressing the eigenvalues of (quasi)local charges as in (1.52). Similarly to the standard equilibrium TBA [21], it is possible to partially decouple the system of integral equations (2.11), obtaining

$$\ln \eta^{(\alpha)}_n = \alpha w_n + s \star \ln(1 + \eta^{(\alpha)}_{n-1})(1 + \eta^{(\alpha)}_{n+1}) \qquad (\eta_0 \equiv 0), \tag{2.13}$$

where

$$s(\lambda) \equiv \frac{1}{2\pi} \sum_{k=-\infty}^{\infty} \frac{e^{-2ik\lambda}}{\cosh k\eta} = \frac{1}{2\pi} + \frac{1}{2\pi} \sum_{k=1}^{\infty} \frac{\cos 2k\lambda}{\cosh k\eta}, \tag{2.14}$$

and the source terms w_n are defined as

$$d_n = g_n - s \star (g_{n-1} + g_{n+1}), \qquad (g_0 \equiv 0). \tag{2.15}$$

This set of equations is easier to solve numerically than (2.11) because they contain fewer convolutions. Once the solutions $\eta^{(\alpha)}_n(\lambda)$ are determined, the particle densities $\boldsymbol{\rho}^{(\alpha)}$ are obtained by using the BGT equations (1.30). Finally, the GGE Rényi entropy (2.5) is obtained by evaluating (2.7) on the densities $\boldsymbol{\rho}^{(\alpha)}$ as

$$S^{(\alpha)}_{\rm GGE}/L = \frac{1}{\alpha - 1}\Big[\Big(\alpha \mathcal{E}[\boldsymbol{\rho}^{(\alpha)}] - s_{\rm YY}[\boldsymbol{\rho}^{(\alpha)}]\Big) + \alpha f_{\rm GGE}[\boldsymbol{\rho}_\beta]\Big], \tag{2.16}$$

where $f_{\rm GGE}[\boldsymbol{\rho}_\beta]$ is the grand canonical potential (2.9) expressed by the saddle point (1.70). Note that $f_{\rm GGE}$ is calculated over the macrostate $\boldsymbol{\rho}_\beta \equiv \boldsymbol{\rho}^{(1)}$, i.e., with $\alpha = 1$.

We stress that the thermodynamic macrostate $\boldsymbol{\rho}^{(\alpha)}$ describing the Rényi entropies is not the same as $\boldsymbol{\rho}_\beta$, which characterises the local observables, or the von Neumann entropy. Moreover, the Renyi entropies with different α are computed from different representative macrostates $\boldsymbol{\rho}^{(\alpha)}$. This difference does not come as a surprise when considering the thermodynamic entropies. However, the thermodynamic entropies are the same as the entanglement entropies of a subsystem that is large in itself but a vanishing fraction of the whole system. From this point of view, the difference is very puzzling because entanglement entropies are all calculated from the same quantum mechanical wavefunction.

2.1.2 A simplified expression for the Rényi entropies

The GGE Rényi entropy as expressed in (2.16) are functionals of an infinite set of densities $\rho_n(\lambda)$. In this section we show that it is possible to simplify (2.16), writing the Rényi entropies only in terms of $\eta_1^{(\alpha)}$. A formula similar to the one we are going to derive is known for the Gibbs (thermal) free energy since many years [21].

The first step in this derivation is to rewrite (2.16) as

$$S^{(\alpha)}_{\rm GGE} = \frac{L}{\alpha-1}\sum_{n=1}^{\infty}\int_{-\pi/2}^{\pi/2}{\rm d}\lambda\Big[\alpha\rho_n^{(\alpha)}(\lambda)g_n(\lambda) - \rho_n^{(\alpha)}(\lambda)\ln(1+\eta_n^{(\alpha)}(\lambda)) \\ - \rho_{{\rm h},n}^{(\alpha)}(\lambda)\ln(1+1/\eta_n^{(\alpha)}(\lambda))\Big] + \frac{\alpha L}{\alpha-1}f_{\rm GGE}. \tag{2.17}$$

By eliminating $\alpha g_n(\lambda)$ using the saddle-point equations (2.11), and eliminating $\rho_{{\rm h},n}(\lambda)$ via the BGT equations (1.30), we get

$$S^{(\alpha)}_{\rm GGE} = \frac{L}{1-\alpha}\left[\sum_{n=1}^{\infty}\int_{-\pi/2}^{\pi/2}{\rm d}\lambda\, a_n(\lambda)\ln(1+1/\eta_n^{(\alpha)}(\lambda)) - \alpha f_{\rm GGE}\right]. \tag{2.18}$$

The infinite sum in (2.18) can be further simplified by considering the first of the saddle point equations in (2.11), which can be rewritten as

$$\ln(1+\eta_1^{(\alpha)}(\lambda)) = \alpha g_1(\lambda) + \sum_{m=1}^{\infty}[(a_{m-1}+a_{m+1})\star\ln(1+1/\eta_m^{(\alpha)})](\lambda). \tag{2.19}$$

One then has to multiply (2.19) by $s(\lambda)$ (cf. (2.14)) and integrate over λ, obtaining

$$\int_{-\pi/2}^{\pi/2}{\rm d}\lambda\, s(\lambda)\Big[\ln(1+\eta_1^{(\alpha)}(\lambda)) - \alpha g_1(\lambda)\Big] = \sum_{n=1}^{\infty}\int_{-\pi/2}^{\pi/2}{\rm d}\lambda\, a_m(\lambda)\ln(1+1/\eta_m^{(\alpha)}(\lambda)). \tag{2.20}$$

The right-hand side of (2.20) is precisely the first term in the square brackets in (2.18). Plugging (2.20) into (2.18), one obtains the simplified formula for the Rényi entropy as

$$S^{(\alpha)}_{\rm GGE} = \frac{L}{\alpha-1}\left\{\int_{-\pi/2}^{\pi/2}{\rm d}\lambda\, s(\lambda)\Big[\alpha g_1(\lambda) - \ln(1+\eta_1^{(\alpha)}(\lambda))\Big] + \alpha f_{\rm GGE}\right\}, \tag{2.21}$$

which is our final result depending only on $\eta_1^{(\alpha)}(\lambda)$.

While (2.21) depends explicitly only on $\eta_1^{(\alpha)}$, it is still necessary to solve the full set of TBA equations (2.11) in order to determine $\eta_1^{(\alpha)}$, because all the $\eta_n^{(\alpha)}$ are coupled. However, Eq. (2.21) has at least two advantages. First, it is more convenient than (2.16) from the numerical point of view, because it contains less integrals to be evaluated. Second, Eq. (2.21) is more convenient for analytical manipulations, as we will see later.

2.1.3 Rényi entropies after quenching from the dimer state

Let us now employ the TBA approach described above to calculate the Rényi entropies after quenching from the dimer state, generalising the results of Ref. [136] for the quench from the Néel state. The translationally invariant dimer initial state is defined as

$$|\Psi_0\rangle = \left(\frac{1+\mathcal{T}_1}{\sqrt{2}}\right)\left(\frac{|\uparrow\downarrow\rangle - |\downarrow\uparrow\rangle}{\sqrt{2}}\right)^{\otimes L/2}, \tag{2.22}$$

where $\mathcal{T}$ is the one-site translation operator. For the dimer state, the overlaps with Bethe states, and the Quench Action driving functions (1.74) are analytically known [57]. Since the Quench Action saddle point must be the same as the GGE saddle point describing local observables in the relaxed state, the GGE driving functions $g_n(\lambda)$ (2.12) are the same as the Quench Action driving functions $d_n(\lambda)$. Therefore, by using the overlap formulas of Ref. [57],

$$\begin{aligned} g_1(\lambda) &= -\ln\left(\frac{\sinh^4(\lambda)\cot^2(\lambda)}{\sin(2\lambda+i\eta)\,\sin(2\lambda-i\eta)}\right), \\ g_n(\lambda) &= \sum_{k=1}^{n} g_1(\lambda + i\eta(n+1-2k)/2), \qquad (n\geq 2), \end{aligned} \tag{2.23}$$

$$w_n(\lambda) = -\ln\left(\frac{\vartheta_4(\lambda)}{\vartheta_1(\lambda)}\right)^2 + (-1)^n \ln\left(\frac{\vartheta_2(\lambda)}{\vartheta_3(\lambda)}\right)^2, \tag{2.24}$$

where $\vartheta_\ell(x)$ are the Jacobi ϑ-functions with nome $e^{-2\eta}$.

The strategy to calculate the Rényi entropies is to use the driving function g_n in the TBA equations for $\eta_n^{(\alpha)}$ (cf. (2.11)). After solving for $\eta_n^{(\alpha)}$, the GGE Rényi entropies are obtained from (2.21).

The numerical results for the Rényi entropies obtained with this procedure are shown in Figure 2.1. The Figure shows the entropy densities $S^{(\alpha)}/L$ plotted versus the chain anisotropy Δ. Different lines correspond to different values of α. As expected, one has that for any Δ, $S^{(\alpha)} < S^{(\alpha')}$ if $\alpha > \alpha'$. For completeness we report the result for $\alpha \to 1$. An interesting observation is that the Rényi entropies do not vanish in the Ising limit for $\Delta \to \infty$. This is in contrast with what happens for the quench from the Néel state [135, 136], for which the steady-state entropies at $\Delta \to \infty$ vanish. The reason is that the Néel state becomes the ground state of the XXZ chain in that limit, and there is no dynamics after the quench. In some limiting cases it is possible to derive closed analytic formulas for the post-quench stationary Rényi entropy: in the following, we will provide analytical results in the Ising limit $\Delta \to \infty$ and for the min entropy, i.e., the limit $\alpha \to \infty$.

2.1.4 Expansion of Rényi entropies in the Ising limit

In this section we perform an expansion of the steady-state Rényi entropies in the large Δ limit, by closely following the procedure introduced in [138]. A similar expansion for the Rényi entropies after the quench from the Néel state has been

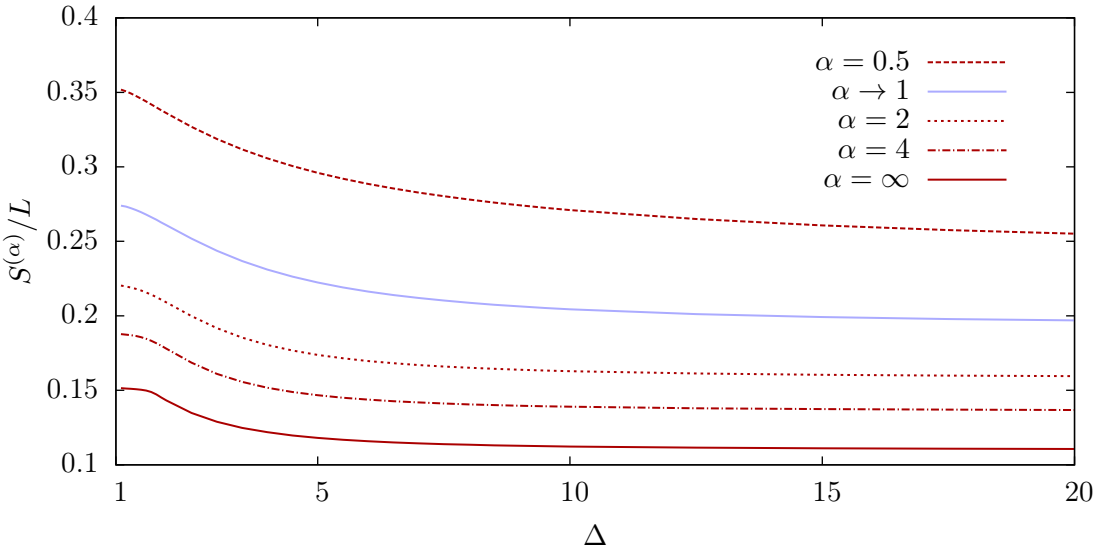

Figure 2.1: Rényi entropies of the GGE after the quench from the dimer state in the XXZ chain. The entropy densities $S^{(\alpha)}/L$ are plotted as a function of the chain anisotropy Δ. The different lines denote results for different Rényi index α. In the limit $\Delta \to \infty$ all the Rényi entropies remain finite. (Figure taken from [137].)

carried out in [135]. In that case, the $\Delta \to \infty$ limit is very special, since the Néel state becomes the ground state of the model, and there is no dynamics. The quench from the dimer state is more generic, because the dimer state is never an eigenstate of the chain, and consequently the post-quench dynamics is nontrivial, implying that the stationary value of the Rényi entropy is nonzero also for $\Delta \to \infty$. We anticipate that in the Ising limit the Rényi entropies have the same form as for free-fermion models [135], but deviations from the free-fermion result appear already at the first non trivial order in $1/\Delta$.

In the following we obtain the steady-state Rényi entropies as a power series in the variable $z \equiv e^{-\eta}$ with $\eta = \operatorname{arccosh}(\Delta)$. Following [136], we use the ansatz for $\eta_n^{(\alpha)}$

$$\eta_n^{(\alpha)}(\lambda) = z^{\beta_n(\alpha)} \eta_{n,0}^{(\alpha)}(\lambda) \exp\left(\Phi_n^{(\alpha)}(z,\lambda)\right). \tag{2.25}$$

Here the exponents $\beta_n(\alpha)$, the functions $\Phi_n^{(\alpha)}(\lambda)$, and $\eta_{n,0}^{(\alpha)}$ have to be determined by plugging the ansatz (2.25) into the TBA equations (2.13). We also need the expansion of the driving functions d_n around $z = 0$:

$$d_n = \begin{cases} \ln(4\sin^2(2\lambda))\, z^2 + 4\cos(4\lambda)\, z^4 + O(z^6) & n \text{ even}, \\ \ln(\tan^2(\lambda)) + 8\cos(2\lambda)\, z^2 - 8\cos(2\lambda)\, z^4 + O(z^6) & n \text{ odd}. \end{cases} \tag{2.26}$$

The expansion of the kernel $s(\lambda)$ appearing in (2.13) is

$$s(\lambda) = \frac{1}{2\pi} + \frac{2}{\pi}\cos(2\lambda) z + \frac{2}{\pi}\cos(4\lambda) z^2 + O(z^3). \tag{2.27}$$

After plugging the ansatz (2.25) into (2.13), and considering the leading order in powers of z, one can fix the exponents β_n. By treating separately the cases of even and odd n in (2.26), one finds

$$\beta_n = \begin{cases} 2\alpha & n \text{ even}, \\ 0 & n \text{ odd}. \end{cases} \tag{2.28}$$

This choice is not unique, but it is the only one that is consistent with the BGT equations (1.30), see [138]. The leading order in z of (2.13) fixes the functions $\eta_{n,0}(\lambda)$ as

$$\eta_{n,0}^{(\alpha)}(\lambda) = \begin{cases} 4^\alpha \, e^{c(\alpha)} \, |\sin(\lambda)|^{2\alpha} & n \text{ even}, \\ |\tan(\lambda)|^{2\alpha} & n \text{ odd}, \end{cases} \tag{2.29}$$

where the constant $c(\alpha)$ is given as

$$c(\alpha) = \frac{1}{\pi} \int_{-\pi/2}^{\pi/2} \mathrm{d}\mu \ln(1 + |\tan(\mu)|^{2\alpha}). \tag{2.30}$$

In the limit $\alpha \to 1$, one has $c(1) = \ln 4$. Interestingly, Eq. (2.29) shows that for n odd, $\eta_n^{(\alpha)}$ is a regular function for any value of λ, whereas for even n it diverges for $\lambda = \pm\pi/2$. This is a striking difference compared to the quench from the Néel state, for which $\eta_n^{(\alpha)}$ diverges in the limit $\lambda \to 0$ for even n (see Ref. [136]), whereas it is regular for odd n.

Also, at the leading order in z, one has that $\Phi_n^{(\alpha)} = 0$. By combining the results in (2.29) and (2.28) with the BGT equations (1.30), the leading order of the rapidity densities $\rho_{\mathrm{t},n}^{(\alpha)}$ are

$$\rho_{\mathrm{t},1}^{(\alpha)} = \frac{1}{2\pi}(1 + 4\cos(2\lambda)\, z) + O(z^{\min(2,2\alpha)}), \tag{2.31}$$

$$\rho_{\mathrm{t},2}^{(\alpha)} = \frac{1}{8\pi} + O(z^{\min(1,2\alpha)}), \tag{2.32}$$

$$\rho_{\mathrm{t},n}^{(\alpha)} = O(z^{2\alpha}) \qquad (n \geq 2). \tag{2.33}$$

We note that for any α, only $\rho_n^{(\alpha)}$ and $\rho_{\mathrm{t},n}^{(\alpha)}$ with $n \leq 2$ remain finite in the limit $z \to 0$, whereas all densities with $n > 2$ vanish. This is different from the Néel state, for which only the densities with $n = 1$ are finite [136]. Physically, this is expected because in the dimer state only components with at most two aligned spins can be present. Furthermore, the leading order of $\rho_{\mathrm{t},n}^{(\alpha)}$ in (2.31)-(2.33) does not depend on the Rényi index α. Finally, in the limit $z \to 0$, the densities become constant, similar to free-fermion models. This suggests that in the limit $z \to 0$ the form of the Rényi entropies may be similar to that of free models, as we are going to show in the following.

It is now straightforward to derive the leading behaviour of the Rényi entropies for any α in the limit $z \to 0$. First, we obtain the expansion of the driving functions g_n (2.23) as

$$g_1(\lambda) = \ln(4\tan^2(\lambda)) + 4z + 4\sin^2(2\lambda)z^2 + O(z^3), \tag{2.34}$$

$$g_2(\lambda) = \ln(64\sin^2(2\lambda)) + 16\sin^2(\lambda)\, z + 4z^2 + O(z^3). \tag{2.35}$$

The contributions of g_n for $n > 2$ are subleading for $z \to 0$ and may be neglected. Using the expansions (2.34) (2.35), the leading order of the densities in (2.31)-(2.33), and (2.29), one obtains the $z \to 0$ limit of $\mathcal{E}$ (cf. (2.8)) as

$$\begin{aligned}\mathcal{E} &= \frac{1}{4\pi}\Big[\int_0^{\pi/2} \mathrm{d}\lambda\, \frac{\ln(4|\tan(\lambda)|^2)}{1+|\tan(\lambda)|^{2\alpha}} + \frac{1}{4}\int_0^{\pi/2} \mathrm{d}\lambda\, \ln(64|\sin(2\lambda)|^2)\Big] \\ &= \frac{1}{8}\ln(2) + \frac{1}{4\pi}\int_0^{\pi/2} \mathrm{d}\lambda\, \frac{\ln(4|\tan(\lambda)|^2)}{1+|\tan(\lambda)|^{2\alpha}}.\end{aligned} \tag{2.36}$$

The two terms in the right-hand-side of (2.36) are the contributions of the densities with $n = 1$ and $n = 2$. Similarly, the $z \to 0$ limit of the Yang-Yang entropy (1.34) is obtained as

$$\begin{aligned}s_{\mathrm{YY}}[\boldsymbol{\rho}^{(\alpha)}] = \frac{1}{2\pi}\int_{-\pi/2}^{\pi/2} \mathrm{d}\lambda \frac{1}{1+|\tan(\lambda)|^{2\alpha}} \ln(1+|\tan(\lambda)|^{2\alpha}) \\ + \frac{1}{2\pi}\int_{-\pi/2}^{\pi/2} \mathrm{d}\lambda \frac{1}{1+|\cot(\lambda)|^{2\alpha}} \ln(1+|\cot(\lambda)|^{2\alpha}).\end{aligned} \tag{2.37}$$

Plugging Eq. (2.36)-(2.37) into the definition of the Rényi entropies (2.2), one obtains at the leading order in z

$$S^{(\alpha)}_{\mathrm{GGE}} = \frac{L}{1-\alpha}\int_{-\pi/2}^{\pi/2} \frac{\mathrm{d}\lambda}{2\pi} \ln\left[\left(\frac{1}{1+\tan^2(\lambda)}\right)^{\alpha} + \left(1-\frac{1}{1+\tan^2(\lambda)}\right)^{\alpha}\right]. \tag{2.38}$$

Eq. (2.38) shows that for any α the Rényi entropies are not vanishing in the limit $z \to 0$.

The Rényi entropy obtained from (2.38) are plotted in Fig. 2.2 as a function of the Rényi index α. Like for finite Δ, the Rényi entropies are monotonically decreasing functions of α. For some values of α the integrals in (2.38) can be computed analytically. For instance, for the max entropy, i.e., in the limit $\alpha \to 0$, one obtains $S^{(0)}/L = \ln(2)/2$: since the max entropy is twice the logarithm of the total number of eigenstates that have nonzero overlap with the initial state [135], we have that that this number is $\propto e^{L/2}$ (which is the same result for the quench from the Néel state [136]). For the min entropy we have $S^{(\infty)}/L = \ln(2) - 2G/\pi$, where G is the Catalan constant. Some other analytical results are reported in the Figure.

It is relatively easy to obtain the higher-order corrections in powers of z for any *fixed* α. Instead, it is rather cumbersome to carry out the expansion for general real α. Therefore, here we only show the explicit calculation for the case $\alpha = 2$. Specifically, we determine $S^{(2)}$ up to $\mathcal{O}(z^2)$. For convenience, instead of $\eta_n^{(\alpha)}$ we consider the filling functions $\vartheta_n \equiv 1/(1+\eta_n)$, where we suppressed the dependence on α, because we consider $\alpha = 2$. The derivation of the higher-order expansion for the filling functions is the same as in Ref. [136] and we will omit it. The idea is that one has to plug the ansatz (2.25) into the equations for η_n (cf. (2.13)) solving the system order by order in powers of z. Similar to the Néel quench, we observe that the system (2.13) contains an infinite set of equations (one for each string type).

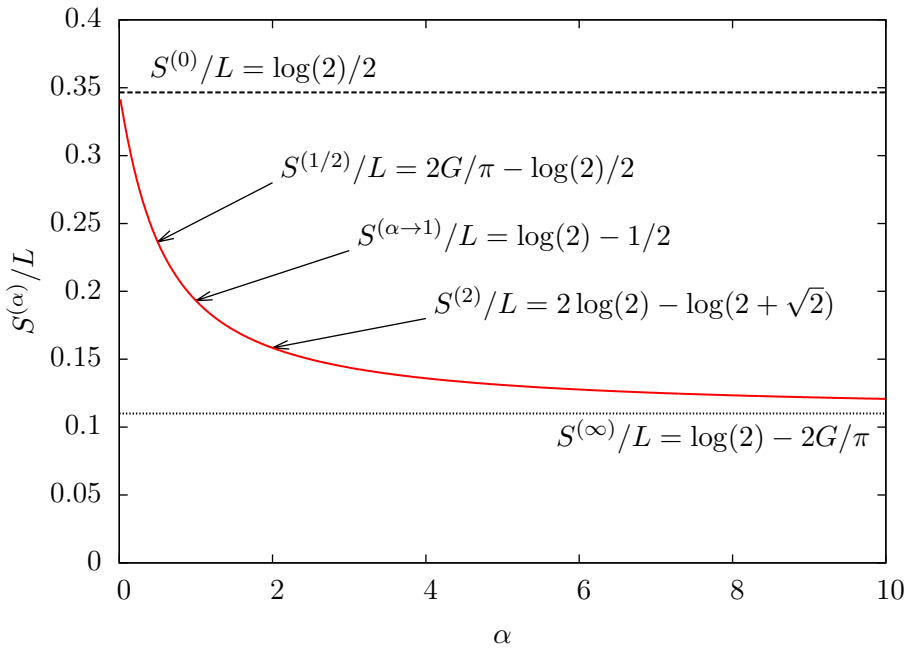

Figure 2.2: Rényi entropy densities S^{α}/L after the quench from the dimer state in the Ising limit $\Delta \to \infty$ of the XXZ chain. On the x-axis α is the Rényi index. The results are obtained using (2.38). The dashed and the dotted lines show the max entropy $S^{(0)}$ and the min entropy $S^{(\infty)}$, respectively. Here G is the Catalan constant. (Figure taken from [137].)

However, to obtain the filling functions up to terms $\mathcal{O}(z^{\omega})$, only the first $m(\omega) \sim \omega$ equations matter because the leading order of higher strings is given by higher orders in powers of z. The expansion of the filling functions ϑ_n around $z = 0$ reads

$$\vartheta_1(\lambda) = \frac{1}{1+\tan(\lambda)^4(\lambda)} - \frac{16\cos(2\lambda)\tan^4(\lambda)}{(1+\tan^4(\lambda))} z^2 + O(z^3), \tag{2.39}$$

$$\vartheta_2(\lambda) = 1 + O(z^4), \tag{2.40}$$

$$\vartheta_n(\lambda) = O(z^4), \qquad (n \geq 3). \tag{2.41}$$

A similar procedure for the TBA equations for the particle densities (cf. (1.30)) gives

$$\rho_{\mathrm{t},1} = \frac{1}{2\pi} + \frac{2}{\pi}\cos(2\lambda) z + \frac{2}{\pi}\cos(4\lambda) z^2 + O(z^3), \tag{2.42}$$

$$\rho_{\mathrm{t},2} = \frac{1}{8\pi} + \frac{2-\sqrt{2}}{\pi}\cos^2(\lambda) z + \frac{1}{\pi}\cos(2\lambda) z^2, \tag{2.43}$$

$$\rho_{\mathrm{t},n} = O(z^4), \qquad (n \geq 3). \tag{2.44}$$

The next-to-leading order in powers of z of the Rényi entropies can be computed by plugging (2.27), (2.34), (2.35) and (2.39)-(2.44) into (2.8) and (1.34). Given that

the first-order in z cancels in both $\mathcal{E}$ and the Yang-Yang entropy and also that the $\mathcal{O}(z^2)$ contribution to S_{YY} vanishes, the first nonzero contribution is $\mathcal{O}(z^2)$ in $\mathcal{E}$, i.e.

$$\mathcal{E} = \frac{1}{4}\ln 2 - \frac{\sqrt{2}\pi}{32} + \frac{z^2}{2} + O(z^3). \tag{2.45}$$

Thus, putting the various pieces together, the second Rényi entropy $S^{(2)}$ is given as

$$S^{(2)} = 2\ln 2 - \ln(2+\sqrt{2}) + 2z^2 + O(z^3). \tag{2.46}$$

Eq. (2.46) implies that the asymptotic value of $S^{(2)}$ for $\Delta \to \infty$ is approached as $1/\Delta$.

2.1.5 A tempting but wrong conjecture

It is tempting to investigate the structure of Eq. (2.38) which has the same structure as the Rényi entropy of free-fermion models, written usually as

$$S^{(\alpha)}_{\rm GGE} = \frac{L}{1-\alpha}\int_{-\pi/2}^{\pi/2}\frac{\mathrm{d}k}{2\pi}\ln\left[\vartheta(k)^\alpha + (1-\vartheta(k))^\alpha\right], \tag{2.47}$$

where $\vartheta(k)$ are now the free-fermion occupation numbers identifying the macrostate. Eq. (2.47) is the same as (2.38) after defining $\vartheta(k) = 1/(1+\tan^2(k))$. Also, the factor $1/(2\pi)$ in (2.38) is the fermionic total density of states $\rho_t = 1/(2\pi)$. A natural question is whether the free-fermion formula (2.47) holds true beyond the leading order in z. For instance, it is interesting to check whether (2.46) can be written in the free-fermion form (2.47). However, as the XXZ chain is interacting, Eq. (2.47) requires some generalisation. First, as there are different families of strings it is natural to sum over the string content of the macrostate. Moreover, in contrast with free fermions, for Bethe ansatz solvable models the total density of states ρ_t is not constant, but it depends on the string type. The most natural generalisation of the free-fermion formula (2.47) would be

$$S^{(\alpha)}_{\rm GGE} \stackrel{?}{=} \frac{L}{1-\alpha}\sum_n \int_{-\pi/2}^{\pi/2} d\lambda \rho_{n,t}\ln[\vartheta_n^\alpha + (1-\vartheta_n)^\alpha]. \tag{2.48}$$

Eq. (2.48) is the same as the free-fermion formula (2.47) except for the overall term $\rho_{\mathrm{t},n}$ in the integrand, which takes into account that for interacting models the density of states is not constant. In Eq. (2.48), the filling functions are given in (2.39)-(2.41).

Unfortunately, Eq. (2.48) does not give the correct value for the steady-state Rényi entropies. A very simple counterexample is provided by the standard Gibbs ensemble at infinite temperature. For the XXZ chain the macrostate describing this ensemble can be derived using the standard TBA approach (see [21]). In particular, for the XXX chain the exact infinite temperature Rényi entropies can be worked out analytically: they become equal and their density is $S^{(\alpha)} = L\ln 2$ for any α. However, by using the analytical expression [21] for the infinite-temperature filling functions ϑ_n for the XXX chain in Eq. (2.48), one can verify that $S^{(2)}/L \neq \ln 2$.

Still, since the free-fermion formula (2.48) holds true exactly at $\Delta \to \infty$ (cf. (2.46)), it is natural to wonder at which order in $1/\Delta$ (equivalently in z) it breaks down. By using Eq. (2.42)-(2.44) and (2.39)-(2.41) in (2.48), one can check that $\rho_{\mathrm{t},2}$ (cf. Eq. (2.43)) gives rise to an $\mathcal{O}(z)$ term in the entropy, which is absent in (2.46). This shows that (2.48) breaks down already at the first nontrivial order beyond the Ising limit.

2.1.6 The min entropy

The Rényi entropy in the limit $\alpha \to \infty$ is also known as min entropy, for which analytical results are obtainable. The analysis of the min entropy after the dimer quench is similar to that for the Néel quench [136]. In the following we remove the dependence on α in the saddle point densities to simplify the notation. After defining the functions $\gamma_n = \ln(\eta_n^{(\alpha)})/\alpha$, the $\alpha \to \infty$ limit of the saddle-point equations (2.13) yields

$$\gamma_n = d_n + s \star (\gamma_{n-1}^+ + \gamma_{n+1}^+), \tag{2.49}$$

where $\gamma_n^+ = (\gamma_n + |\gamma_n|)/2$. Some insights on the structure of the solutions of (2.49) can be obtained by looking at the limit $\Delta \to \infty$. Precisely, from Eq. (2.29) one has that $\eta_n \to 0$ for even n in the limit $\alpha \to \infty$. On the other hand, one has that η_n diverges for odd n for $\lambda \in [-\pi/4, \pi/4]$, which implies $\ln \eta_n = \alpha d_n$ for n odd in that interval. Thus we have that at large Δ, $\gamma_{2n}(\lambda) < 0$ and $\gamma_{2n+1}(\lambda) = d_{2n+1}(\lambda)$. As a consequence, the filling functions ϑ_n become

$$\vartheta_{2n}(\lambda) = \lim_{\alpha\to\infty} \frac{1}{1 + e^{\alpha\gamma_{2n}(\lambda)}} = 1, \tag{2.50}$$

$$\vartheta_{2n+1}(\lambda) = \lim_{\alpha\to\infty} \frac{1}{1 + e^{\alpha d_{2n+1}(\lambda)}} = \Theta_{\mathrm{H}}(|\lambda| - \pi/4), \tag{2.51}$$

where $\Theta_{\mathrm{H}}(x)$ is the Heaviside step function. The associated total densities are obtained using the BGT equations as

$$\rho_{\mathrm{t},1}(\lambda) = s(\lambda), \tag{2.52}$$

$$\begin{aligned}\rho_{\mathrm{t},2}(\lambda) &= [s \star (s \cdot \Theta_{\mathrm{H}}(|x| - \pi/4))](\lambda) \\ &= \frac{1}{4\pi^2} \sum_{k\in\mathbb{Z}} \frac{e^{-2ik\lambda}}{\cosh(k\eta)} \sum_{\ell\neq k} \frac{\sin((k-\ell)\pi) - \sin((k-\ell)\pi/2)}{(k-\ell)\cosh(\ell\eta)} \\ &\quad + \frac{1}{4\pi^2} \sum_{k\in\mathbb{Z}} \frac{e^{-2ik\lambda}}{\cosh(k\eta)} \sum_{\ell\neq k} \frac{\pi}{2\cosh(k\eta)},\end{aligned} \tag{2.53}$$

$$\rho_{\mathrm{t},n}(\lambda) = 0, \qquad (n > 2). \tag{2.54}$$

These results imply that the min entropy is completely determined by the first two densities with $n = 1$ and $n = 2$, in contrast with the quench from the Néel state [136], where only the first density enters in the expression for $S^{(\infty)}$.

To derive the general expression for the min entropy, a crucial preliminary observation is that the macrostate describing $S^{(\infty)}$ has zero Yang-Yang entropy. This

is a general result that holds for quenches from arbitrary states. Indeed, first we notice that the ansatz $\eta_n = e^{\alpha\gamma_n}$ implies that, in the limit $\alpha \to \infty$, ϑ_n can be only zero or one. Then, assuming that $\rho_{\mathrm{t},n}$ is finite, the Yang-Yang entropy

$$s_{YY}[\boldsymbol{\rho}] = -\sum_n \int d\lambda \rho_{\mathrm{t},n}[\vartheta_n \ln \vartheta_n + (1-\vartheta_n)\ln(1-\vartheta_n)], \tag{2.55}$$

must vanish in the limit $\alpha \to \infty$. Consequently the $S^{(\infty)}_{\mathrm{GGE}}$ is determined only by the driving functions as

$$S^{(\infty)}_{\mathrm{GGE}} = L\sum_n \int_{-\pi/2}^{\pi/2} d\lambda g_n \rho_n + L f_{\mathrm{GGE}}. \tag{2.56}$$

Interestingly, in the large Δ limit Eq. (2.56) simplifies. Specifically, only the first two strings with $n = 1, 2$ contribute in (2.56), as it is clear from (2.54).

Upon lowering Δ, we observe a sharp transition in the behaviour of $S^{(\infty)}$. Indeed, there is a "critical" value Δ^*, such that for $\Delta < \Delta^*$, higher-order strings become important. The condition that determines Δ^* is that γ_2 becomes positive, i.e., that for some λ

$$d_2 + 2s \star d_1 \geq 0. \tag{2.57}$$

The value of Δ^* can be found by numerically by imposing equality in (2.57) and the final result is $\Delta^* \approx 1.7669$. This is the same value of Δ^* found for the quench from the Néel state [136], although the condition for higher strings to contribute for the Néel state (i.e. $d_1 + 2s \star d_2 \geq 0$) may appear different. This, however, is equivalent to (2.57) after noticing that $d^{\mathrm{Dimer}}_{2n} = d^{\mathrm{Neel}}_{2n+1}$.

Finally, in contrast with the large Δ limit, for $\Delta < \Delta^*$, an analytical solution of (2.49) is not possible. However, the system (2.49) can be effectively solved numerically. The result for $S^{(\infty)}_{\mathrm{GGE}}$ is reported in Figure 2.1 (bottom line).

2.2 Rényi entropies of generic macrostates

In this section we show how to generalise the approach of Ref. [135] for the calculation of Rényi entropies in the case when the overlaps of a given initial state are not known. In this case, we just know the rapidity densities of the macrostate, e.g. from the string-charge duality [62, 85]. The idea is simple: using the TBA equations

$$\ln \eta_n(\lambda) = g_n(\lambda) + \sum_{m=1}^{\infty} [A_{nm} \star \ln(1 + 1/\eta_m)](\lambda), \tag{2.58}$$

we can extract the numerical values of the driving functions $g_n(\lambda)$ from the GGE saddle point described by $\eta_n(\lambda)$. Once the driving functions are numerically known, it is straightforward to use them in the formalism of Ref. [135] to obtain the steady-state Rényi entropies, as explained in the previous sections. Notice that this procedure does not only apply to stationary states after a quench, but can be used for *generic* Bethe states with arbitrary root densities, independently of where they come from.

Furthermore, for quench problems, this procedure can be used to reconstruct the extensive part of the overlaps and hence to help in conjecturing the entire overlap function at finite size.

To illustrate the validity of the approach, in the following subsections we provide exact results for the Rényi entropies after the quench from the tilted Néel state in the XXZ chain. For this family of quenches, the thermodynamic macrostates describing the post-quench steady states have been calculated in Ref. [62] from the GGE. Only very recently the overlaps of these states with the Bethe ones have been conjectured in Ref. [139]. Consequently, the results presented in the following, not only are a physical relevant application of these ideas but also provide a further confirmation about the validity of the conjecture itself. Finally, we mention that if these ideas would have been developed earlier, they could have speed up the formulation of the conjecture in [139].

2.2.1 Quench from the tilted Néel: the driving terms

Here we numerically extract the driving functions $g_n(\lambda)$ for the global quench (2.4) from the tilted Néel state. The translationally invariant tilted Néel state is

$$\begin{aligned} |\Psi_0\rangle &= \left(\frac{1+\mathcal{T}}{\sqrt{2}}\right) |\nearrow\swarrow\rangle^{\otimes L/2} \\ |\nearrow\swarrow\rangle &\equiv [(\cos(\theta)|\uparrow\rangle + i\sin(\theta/2)|\downarrow\rangle) \otimes (-i\sin(\theta/2)|\uparrow\rangle + \cos(\theta/2)|\downarrow\rangle)]\,, \end{aligned} \tag{2.59}$$

where $\mathcal{T}$ is the one-site translation operator and θ is the tilting angle. The rapidity densities describing the post-quench steady state after this quench have been determined in Ref. [62]. We use these in the system (2.58) to extract g_n. Information about these densities is fully encoded in $\eta_1(\lambda)$, which is given as [62]

$$\eta_1(\lambda) = -1 + \frac{T_1\left(\lambda + i\frac{\eta}{2}\right) T_1\left(\lambda - i\frac{\eta}{2}\right)}{\phi\left(\lambda + i\frac{\eta}{2}\right) \bar{\phi}\left(\lambda - i\frac{\eta}{2}\right)}, \tag{2.60}$$

where the auxiliary functions $\phi, \bar{\phi}$ and T_1 are defined as

$$\begin{aligned} T_1(\lambda) = &-\frac{1}{8}\cot(\lambda)\{8\cosh(\eta)\sin^2(\theta)\sin^2(\lambda) - 4\cosh(2\eta)\} \\ &-\frac{1}{8}\cot(\lambda)\{[\cos(2\theta)+3][2\cos(2\lambda)-1] + 2\sin^2(\theta)\cos(4\lambda)\}, \end{aligned} \tag{2.61}$$

$$\phi(\lambda) = \frac{1}{8}\sin(2\lambda + i\eta)[2\sin^2(\theta)\cos(2\lambda - i\eta) + \cos(2\theta) + 3], \tag{2.62}$$

$$\bar{\phi}(\lambda) = \frac{1}{8}\sin(2\lambda - i\eta)[2\sin^2(\theta)\cos(2\lambda + i\eta) + \cos(2\theta) + 3]. \tag{2.63}$$

For $n > 1$, $\eta_n(\lambda)$ is determined recursively from the Y-system [85]

$$\eta_{n+1}(\lambda) = \frac{\eta_n(\lambda + i\eta/2)\eta_n(\lambda - i\eta/2)}{1 + \eta_{n-1}(\lambda)} - 1, \tag{2.64}$$

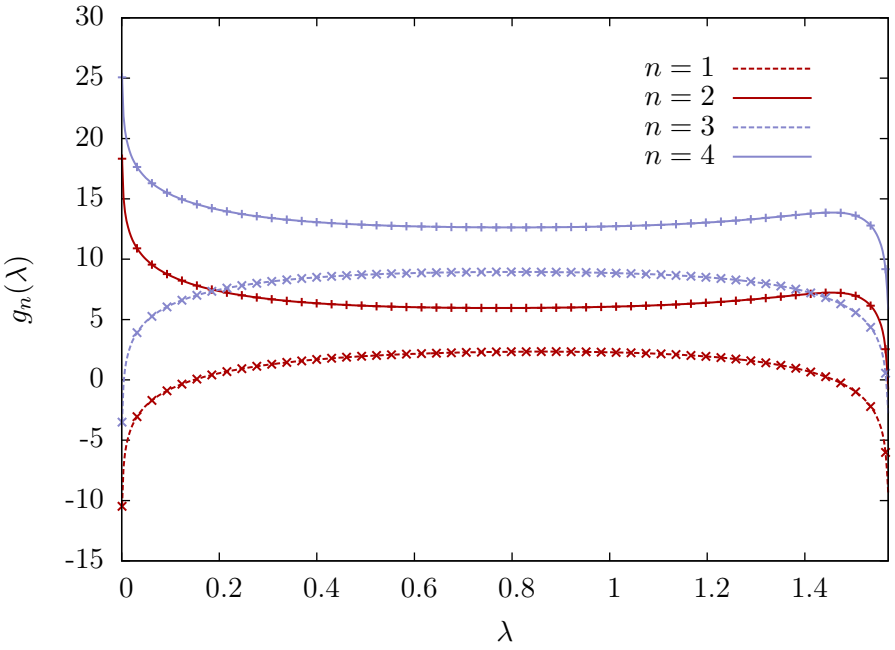

Figure 2.3: GGE driving functions g_n for the quench from the tilted Néel state in the XXZ chain with $\Delta = 2$. On the x-axis λ is the rapidity variable. The Néel tilting angle is $\theta = \pi/3$. Different lines correspond to different strings lengths n. Lines are numerical results using the TBA approach, whereas points denote the analytical conjecture in Ref. [139]. (Figure taken from [137].)

with the convention $\eta_0 \equiv 0$. From the densities η_n, the particle densities ρ_n are obtained, as usual, by solving the thermodynamic version of the TBA equations (1.30).

The driving function g_n can be easily extracted numerically by plugging the above root densities in Eq. (2.58). The results for quenches for the XXZ chain with $\Delta = 2$ and the quench from the tilted Néel state with tilting angle $\theta = \pi/3$ are reported in Figure 2.3. These results may be compared with the recently conjectured form of the overlaps [139].. So far, this conjecture has been tested numerically for Bethe states containing few particles, and it has been shown to give the correct thermodynamic macrostate after the quench. The thermodynamic limit of the overlaps in [139] can be written as

$$\ln\langle\Psi_0|\rho_n\rangle = L\sum_{n=1}^{\infty}\int_{-\pi/2}^{\pi/2} \mathrm{d}\lambda\rho_n(\lambda)g_n(\lambda), \tag{2.65}$$

where ρ_n are the particle densities describing the thermodynamic macrostate and the explicit forms of g_n read [139]

$$g_1(\lambda) = \frac{\tan(\lambda + i\eta/2)\tan(\lambda - i\eta/2)}{4\sin^2(2\lambda)} \cdot \frac{\cos^2(\lambda + i\xi)\cos^2(\lambda - i\xi)}{\cosh^4(\xi)}, \tag{2.66}$$

$$g_n(\lambda) = \sum_{j=1}^{n} g_1(\lambda + i\eta/2(n + 1 - 2j)), \tag{2.67}$$

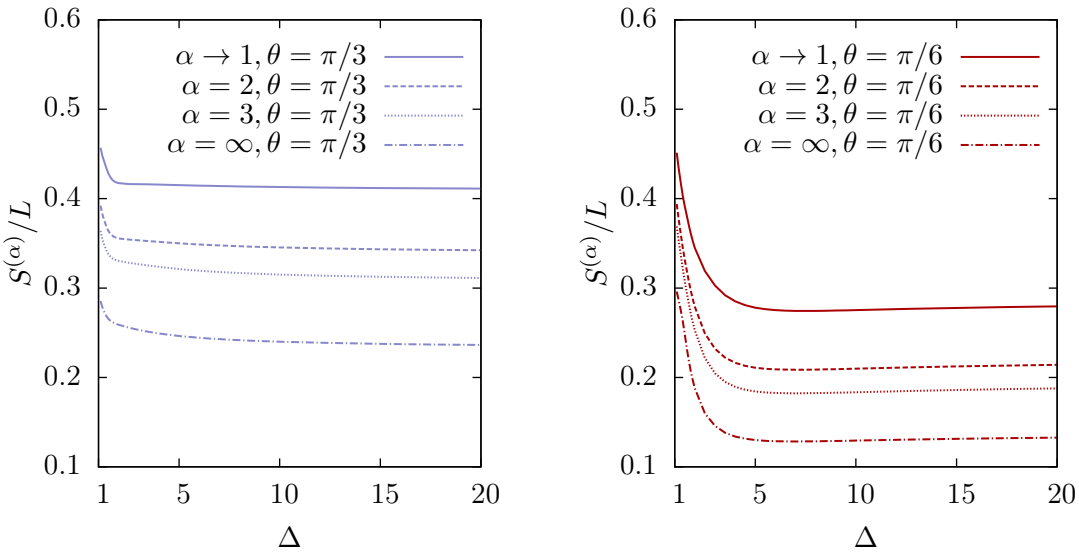

Figure 2.4: Steady-state Rényi entropies $S^{(\alpha)}/L$ after the quench from the tilted Néel state in the XXZ spin chain. The entropies are plotted as a function of the anisotropy Δ. We show results for tilting angles $\theta = \pi/6$ and $\theta = \pi/3$ (right and left panel, respectively). In each panel the different curves correspond to different values of $\alpha \in [1, \infty)$. (Figure taken from [137].)

where ξ is related to the tilting angle θ as $\xi \equiv -\ln(\tan(\theta/2))$.

We now compare the driving functions $g_n(\lambda)$ as extracted from the TBA equations (2.58) with the conjectured result in Eq. (2.66) and (2.67). The comparison is presented in Figure 2.3 for the XXZ chain with $\Delta = 2$ and the quench from the tilted Néel state with tilting angle $\theta = \pi/3$ (we tested them also for other tilting angles, finding equivalent results that we do not report here). The continuous lines are the numerical results for g_n for $n \leq 4$ (higher strings are not reported). The different symbols (crosses) are the numerical results using the conjecture (2.66)-(2.67). As it is clear from the Figure, the agreement between the two results is perfect for all values of λ.

2.2.2 Rényi entropies after quenching from the tilted Néel state

Now we are in the position to obtain results for the steady-state Rényi entropies after the quench from the tilted Néel state in the XXZ chain. The theoretical predictions for the entropies are obtained by combining the results of section 2.2.1 to extract the driving functions g_n with the procedure of Ref. [135] (see section 2.1). Our results are reported in Figure 2.4 plotting $S^{(\alpha)}/L$ versus the chain anisotropy Δ. The data shown in the Figure are for the tilted Néel with tilting angle $\theta = \pi/3$ and $\theta = \pi/6$ (right and left panel, respectively). As expected, one has that $S^{(\alpha)} < S^{(\alpha')}$ if $\alpha > \alpha'$.

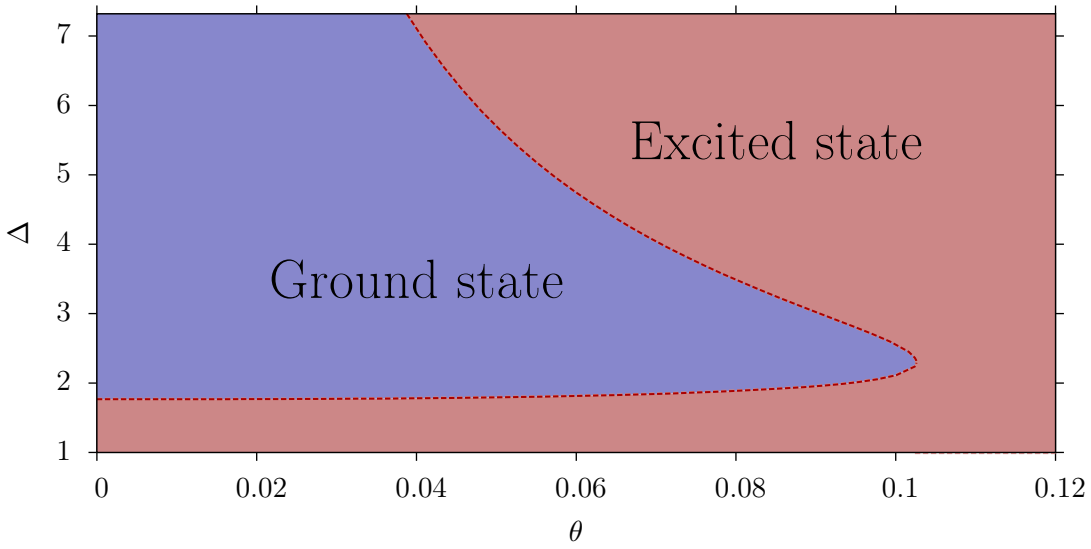

Figure 2.5: TBA macrostate for the steady-state value of the min entropy $S^{(\infty)}$ after the quench from the tilted Néel state in the XXZ chain. The Figure show the macrostate as a function of the chain anisotropy Δ and the tilting angle θ. The blue area denotes the parameter region (θ, Δ) where the macrostate is the ground state of the XXZ chain at that Δ. Outside this region, the macrostate is an excited state of the chain. The dashed line divides the two regions. (Figure taken from [137].)

For all values of α and $\theta \neq 0$ the entropy densities are finite in the limit $\Delta \to \infty$, in contrast with the quench from the Néel state [136], where all the entropies vanish for $\Delta \to \infty$. Finally, an intriguing feature is that for $\theta = \pi/6$ the behaviour of the entropies is not monotonic as a function of Δ, but $S^{(\alpha)}$ exhibits a minimum around $\Delta \approx 5$, although the minimum is not very pronounced. This remains true for a window of tilting angle θ close to $\pi/6$.

2.2.3 The min entropy

Let now focus on the steady-state value of the min entropy, which is determined by the Bethe state that has the largest overlap with $|\Psi_0\rangle$. Similarly to the Néel and dimer states, in the limit $\alpha \to \infty$ one can use the ansatz $(\ln \eta_n^{(\alpha)})/\alpha = \gamma_n$. The equations for γ_n are the same as for the dimer (cf. (2.49)), i.e.,

$$\gamma_n = d_n + s \star (\gamma_{n-1}^{+} + \gamma_{n+1}^{+}), \tag{2.68}$$

where now the driving d_n is obtained from the driving functions g_n for the quench from the tilted Néel as

$$d_n = g_n - s \star (g_{n+1} + g_{n-1}). \tag{2.69}$$

For the Néel quench, i.e., for $\theta = 0$, there is a "critical" value Δ^* such that for $\Delta > \Delta^*$ the thermodynamic macrostate that the describes the min entropy is the

ground state of the XXZ chain [136]. For $\Delta < \Delta^*$ this is not the case, and the macrostate is an excited state with zero Yang-Yang entropy. The "critical" Δ^* at which the behaviour of the thermodynamic macrostate changes is determined for the Néel state (and for the dimer state as well) by the condition that γ_2 becomes positive. It is natural to investigate how this scenario is modified upon tilting the initial state. Here we show that the macrostate describing the min entropy is the ground state of the XXZ chain provided that the tilting angle θ is not too large.

To clarify this issue, we numerically observed that for large Δ

$$\begin{aligned} &\gamma_1(\lambda) < 0, \\ &\gamma_3(\lambda) < 0. \end{aligned} \tag{2.70}$$

The conditions in Eq. (2.70) have important consequences for the particle densities ρ_n. In particular, it implies that the macrostate describing the min entropy is the ground state of the XXZ chain. To show that, let us consider the TBA equations for $\rho_{\mathrm{t},n}$, which are

$$\rho_{n,\mathrm{t}} = s \star [(1-\vartheta_{n-1})\rho_{\mathrm{t},n-1} + (1-\vartheta_{n+1})\rho_{\mathrm{t},n+1}]. \tag{2.71}$$

First, since $\vartheta_0 = 0$ and $\rho_0 = \delta(\lambda)$, one has that $\rho_1 = s$, which is the density of the ground state of the XXZ chain. Clearly, the conditions in (2.70) together with the system (2.71) imply that $\rho_{2,\mathrm{t}} = 0$. Another important consequence is that the first two equations in (2.71) are decoupled from the rest, which form a linear homogeneous system of integral equations. Moreover, for $n \to \infty$ one expects that $\rho_{\mathrm{t},n} \to 0$. Thus, it is natural to conjecture that $\rho_{\mathrm{t},n} = 0$ for any $n > 2$. Finally, we observe that a similar decoupling occurs for the quench from the Néel state [136], although via a different mechanism. Precisely, for the the Néel state one has that $\gamma_{2n+1} < 0$ for all n.

We now use the conditions (2.70) to characterise the behaviour of the min entropy. Our results are summarised in the "phase diagram" in Fig. 2.5. The blue region in the figure corresponds to the region in the parameter space (θ, Δ) where the thermodynamic macrostate describing the min entropy is the ground state of the XXZ chain (at that value of Δ). For $\theta = 0$ we recover the result of Ref. [136], i.e., that the ground state describes the min entropy for $\Delta > \Delta^* \approx 1.766$. The ground state remains the correct macrostate for the min entropy in a region of not too large θ. Conversely, for $\theta \gtrsim 0.1$ the macrostate is an excited state of the XXZ at any Δ. However, at smaller θ there is always an extended region where the min entropy is described by the ground state of the XXZ chain. The extension of this region shrinks upon increasing Δ, and it is likely to vanish in the limit $\Delta \to \infty$. The dashed line in Fig. 2.5 marks the "transition" between the two regimes. The line is obtained by numerically finding the values of (θ, Δ) for which either γ_1 or γ_3 vanish, violating the conditions in Eq. (2.70).

2.3 Discussion

In this Chapter we studied the Rényi entropies in the stationary state after a quantum quench. As shown in Refs. [135, 136], in the quench action approach the Rényi entropies are the generalised free energy of a macrostate that may be derived from the knowledge of the overlaps of the initial state with Bethe eigenstates. The thermodynamic limit of the overlaps provides the driving term in the TBA formalism. Here we considered the problem of determining the Rényi entropies in a generic thermodynamic macrostate of integrable models, even in those cases when the overlaps are not known. We showed that the needed driving term can be reconstructed starting from the macrostate's particle densities. Then we provided a major simplification of the expression for the generalised free energy that may be rewritten only as a function of the occupation numbers of 1-strings, cf. Eq. (2.21) which is a much simpler and manageable formula than the known sum over all string content.

We then studied accurately the stationary Rényi entropies after the quench from the dimer and the tilted Néel states in the XXZ Heisenberg spin chain. For the former initial state we employed the quench action approach, while for the latter we reconstructed the driving terms from the macrostate. The overall results for the dimer states are summarised in Fig. 2.1 which shows the Δ and α dependence of the Rényi entropies. We also analysed in details two limits that are analytically tractable, namely $\Delta \to \infty$ and $\alpha \to \infty$. In the Ising limit $\Delta \to \infty$, the result for the Rényi entropies resembles that of free-fermion models, as it should. Deviations from the free-fermion result appear already at the first non trivial order in $1/\Delta$. For the min entropy, i.e. $\alpha \to \infty$, we found that the representative state has vanishing Yang-Yang entropy for arbitrary Δ. We also found a sharp transition of this state at a critical value of Δ denoted as Δ^*. For $\Delta > \Delta^*$, the representative state contains one- and two-strings only (as a difference with the quench from Néel state where only one-strings matter) while for $\Delta < \Delta^*$ the other bound states start being present. When the initial configuration is the tilted Néel state, the results for the Rényi entropies as function of Δ, α, and the tilting angle θ are reported in Fig. 2.4. As a main difference with the other cases, the entropies as function of Δ are not always monotonic, but they may show a minimum for some values of θ. Also in this case we analytically studied the min entropy. We again found that the representative eigenstate has zero Yang-Yang entropy for arbitrary Δ and θ and that there is a sharp transition line. The resulting "phase diagram" is reported in Fig. 2.5: there is a region for small θ where the representative eigenstate is the ground state (and hence only one-strings are present), while in the rest of the phase diagram, other bound states matter. The results presented here (and the ones for the Néel state [136]) show that rather generically the representative state of the min entropy has zero Yang-Yang entropy. It would be interesting to find out the minimal conditions on the initial state for this property to be generically valid.

A major problem that remains still open is to characterise the time evolution of Rényi entanglement entropies for generic interacting integrable model, both for homogeneous quenches and quenches from piecewise homogeneous initial states (see

[140] for some results). Technically, it is not possible to generalise the semi-classical approach developed for the von Neumann entropy [141, 142] because the Rényi entropies have been written in terms of root distributions which are not the ones of the macrostate describing local properties: only the latter determines the asymptotic spreading of entanglement [141, 142] and correlations [30]. Apart from the *per se* theoretical interest, this issue is also fundamental for a comparison with cold atom experiments in which only Rényi entropies can be measured [143–146].

Chapter 3

Quench action in the Lai–Sutherland model

One of the main obstacles in using the Quench Action formalism is that the overlaps of the initial state with Bethe ansatz eigenstates need to have the form (1.74)–(1.75), where the analytical form of the density function $d_{\Psi_0,n}(\lambda)$ needs to be known. Therefore it is not trivial to find initial states in integrable models for which the quench action formalism can be carried out.

In this Chapter we consider the quench action approach for a global quantum quench in the SU(3) invariant Lai–Sutherland model, which is an integrable quantum chain solvable by nested Bethe ansatz, and which contains two distinct species of quasiparticles. We also provide predictions for the propagation of entanglement and mutual information after the quench, which can be used as signature of the quasi-particle content of the model.

3.1 The model and the Bethe ansatz solution

We consider the spin-1 Lai-Sutherland model [147, 148], described by the Hamiltonian

$$H_L = \sum_{j=1}^{L} \left[\mathbf{s}_j \cdot \mathbf{s}_{j+1} + (\mathbf{s}_j \cdot \mathbf{s}_{j+1})^2 \right] - 2L \,, \tag{3.1}$$

which acts on the Hilbert space $\mathcal{H}_L = h_1 \otimes \ldots \otimes h_L$. Here $h_j \simeq \mathbb{C}^3$ is the local (physical) Hilbert space associated with site j. The spin-1 operators s_j^a are given by the standard three-dimensional representation of the $SU(2)$ generators, explicitly

$$s^x = \frac{1}{\sqrt{2}} \begin{pmatrix} 0 & 1 & 0 \\ 1 & 0 & 1 \\ 0 & 1 & 0 \end{pmatrix}, \quad s^y = \frac{1}{\sqrt{2}} \begin{pmatrix} 0 & -i & 0 \\ i & 0 & -i \\ 0 & i & 0 \end{pmatrix}, \quad s^z = \begin{pmatrix} 1 & 0 & 0 \\ 0 & 0 & 0 \\ 0 & 0 & -1 \end{pmatrix}. \tag{3.2}$$

In the following, we define the local spin-1 basis as

$$|\Uparrow\rangle = \begin{pmatrix} 1 \\ 0 \\ 0 \end{pmatrix}, \quad |0\rangle = \begin{pmatrix} 0 \\ 1 \\ 0 \end{pmatrix}, \quad |\Downarrow\rangle = \begin{pmatrix} 0 \\ 0 \\ 1 \end{pmatrix}, \tag{3.3}$$

and will use the labeling

$$|e_1\rangle = |\Uparrow\rangle \ , \quad |e_2\rangle = |0\rangle \ , \quad |e_3\rangle = |\Downarrow\rangle \ , \tag{3.4}$$

and

$$|e_{\alpha_1} e_{\alpha_2} \dots e_{\alpha_L}\rangle = |e_{\alpha_1}\rangle \otimes |e_{\alpha_2}\rangle \otimes \dots \otimes |e_{\alpha_L}\rangle \, . \tag{3.5}$$

The Hamiltonian (3.1) is expressed in terms of the $SU(2)$ spin-1 operators (3.2) and is manifestly invariant under action of $SU(2)$. In fact, it is invariant under the action of the larger group $SU(3)$ [149].

The Lai-Sutherland model should not be confused with the different spin-1 integrable chain

$$H_L^{\mathrm{B}} = \sum_{j=1}^{L} \left[\mathbf{s}_j \cdot \mathbf{s}_{j+1} - (\mathbf{s}_j \cdot \mathbf{s}_{j+1})^2 \right] \, , \tag{3.6}$$

which is the Hamiltonian of the $SU(2)$-invariant Babujian-Takhtajan model [150, 151]. This model can be analyzed by means of the so called fusion procedure [152], starting from the Bethe ansatz solution of the spin-1/2 Heisenberg chain; quantum quenches in the model defined by (3.6) have been considered in [62]. To clarify the difference between the two Hamiltonians, it is useful to introduce the operators

$$\mathcal{N}_1 \equiv \sum_{j=1}^{L} \Big[(E_2^2)_j + (E_3^3)_j \Big] \, , \tag{3.7}$$

$$\mathcal{N}_2 \equiv \sum_{j=1}^{L} \Big[(E_3^3)_j \Big] \, , \tag{3.8}$$

where we defined

$$E_j^i \equiv |e_j\rangle\langle e_i| \, . \tag{3.9}$$

When applied to a state, the operator $\mathcal{N}_1$ counts the number of spins which are either $|0\rangle$ or $|\Downarrow\rangle$ while $\mathcal{N}_2$ counts the number of spins $|\Downarrow\rangle$. It is straightforward to see that these operators are mutually commuting and moreover commute with the Hamiltonian (3.1), which follows directly from the $SU(3)$ invariance of H_L. On the other hand, these operators *do not* separately commute with the Hamiltonian H_L^{B} (*cf.* (3.6)): only their sum does.

This seemingly innocent difference has drastic consequences on the physics of the two models. While the quasi-particle content and the structure of elementary excitations of the theory defined by (3.6) are analogous to that of the spin-1/2 case, the one of the theory described by (3.1) is completely different: two different species of elementary excitations emerge.

3.1.1 The nested Bethe anstatz solution

The Hamiltonian (3.1) is diagonalized by nested Bethe ansatz. Here we briefly sketch the main aspects relevant to our work while we refer to the specialized literature for a systematic treatment [23, 149, 153, 154].

The starting point is to construct a Bethe-state on the chain of length L. In the model at hand, this state is parametrized by *two* sets of complex parameters called rapidities, $\boldsymbol{k}_N = \{k_j\}_{j=1}^N$ and $\boldsymbol{\lambda}_M = \{\lambda_j\}_{j=1}^M$, as follows:

$$\begin{aligned} |\boldsymbol{k}_N, \boldsymbol{\lambda}_N\rangle = & \sum_{1\le n_1<\ldots<n_N\le L 1\le m_1<\ldots<m_M\le N} \sum_{\mathcal{P}\in\mathcal{S}^N} \left(\prod_{1\le r<l\le N} \frac{k_{\mathcal{P}(l)} - k_{\mathcal{P}(r)} - i}{k_{\mathcal{P}(l)} - k_{\mathcal{P}(r)}} \right) \\ & \times \langle \boldsymbol{m}|\boldsymbol{k}_{\mathcal{P}}, \boldsymbol{\lambda}\rangle \prod_{r=1}^N \left(\frac{k_{\mathcal{P}(r)} + i/2}{k_{\mathcal{P}(r)} - i/2} \right)^{n_r} \prod_{r=1}^M (E_3^2)_{n_{m_r}} \prod_{s=1}^N (E_2^1)_{n_s} |\Omega\rangle \,. \end{aligned} \tag{3.10}$$

Here we defined the reference state

$$|\Omega\rangle = |\Uparrow\Uparrow \ldots \Uparrow\rangle \,, \tag{3.11}$$

together with the functions

$$\langle \boldsymbol{m}|\boldsymbol{k}_{\mathcal{P}}, \boldsymbol{\lambda}\rangle = \sum_{\mathcal{R}\in\mathcal{S}^M} A(\boldsymbol{\lambda}_{\mathcal{R}}) \prod_{\ell=1}^M F_{\boldsymbol{k}_{\mathcal{P}}}(\lambda_{\mathcal{R}(\ell)}; m_\ell) \,, \tag{3.12}$$

$$F_{\boldsymbol{k}}(\lambda, s) = \frac{-i}{\lambda - k_s - i/2} \prod_{n=1}^{s-1} \frac{\lambda - k_n + i/2}{\lambda - k_n - i/2} \,, \tag{3.13}$$

$$A(\lambda) = \prod_{1\le r<l\le M} \frac{\lambda_l - \lambda_r - i}{\lambda_l - \lambda_r} \,. \tag{3.14}$$

The numbers of the two kinds of rapidities, N and M, must satisfy

$$L \ge N \,, \qquad N \ge 2M \,, \tag{3.15}$$

where L is the size of the chain.

In complete analogy with the Bethe ansatz solution of the spin-1/2 Heisenberg chain (see Section 1.2), one can show that the state (3.10) is an eigenstate of the Hamiltonian (3.1) provided that the rapidities satisfy a set of non-linear quantization conditions, known as nested Bethe equations, which read

$$\left(\frac{k_j + i/2}{k_j - i/2} \right)^L = \prod_{\substack{p=1 \\ p\ne j}}^N \frac{k_j - k_p + i}{k_j - k_p - i} \prod_{\ell=1}^M \frac{\lambda_\ell - k_j + i/2}{\lambda_\ell - k_j - i/2} \quad j = 1, \ldots, N \,, \tag{3.16}$$

$$1 = \prod_{j=1}^N \frac{k_j - \lambda_\ell - i/2}{k_j - \lambda_\ell + i/2} \prod_{\substack{m=1 \\ m\ne\ell}}^M \frac{\lambda_\ell - \lambda_m - i}{\lambda_\ell - \lambda_m + i} \,, \quad \ell = 1, \ldots, M \,. \tag{3.17}$$

The energy and the momentum of the eigenstate $|\boldsymbol{k}_N, \boldsymbol{\lambda}_M\rangle$ are given by

$$E = -\sum_{j=1}^N \frac{1}{k_j^2 + 1/4} \,, \qquad P = \left[\sum_{j=1}^N i \ln \left[\frac{k_j + i/2}{k_j - i/2} \right] \right] \bmod 2\pi \,. \tag{3.18}$$

Note that since the Hamiltonian (3.1) is integrable there exist infinitely many local conserved operators (or charges) beyond energy and momentum, which can be constructed by standard techniques [22]. In analogy with (3.18), the expectation value of higher conserved charges on a Bethe state are immediately obtained once the sets of rapidities characterising the state are known. This is discussed in more detail in Appendix 3.A.

The Bethe states $|\boldsymbol{k}_N, \boldsymbol{\lambda}_M\rangle$ are common eigenstates of the Hamiltonian and of the operators $\mathcal{N}_1$ and $\mathcal{N}_2$ introduced in (3.7), (3.8). In particular, one has

$$\mathcal{N}_1|\boldsymbol{k}_N, \boldsymbol{\lambda}_M\rangle = N|\boldsymbol{k}_N, \boldsymbol{\lambda}_M\rangle\,, \tag{3.19}$$

$$\mathcal{N}_2|\boldsymbol{k}_N, \boldsymbol{\lambda}_M\rangle = M|\boldsymbol{k}_N, \boldsymbol{\lambda}_M\rangle\,. \tag{3.20}$$

The physical interpretation for the state (3.10) is straightforward in the case where all the rapidities $\boldsymbol{k}_N, \boldsymbol{\lambda}_M$ are real. In this case $\boldsymbol{k}_N$ and $\boldsymbol{\lambda}_M$ can be thought as the rapidities of two different species of quasi-particles created on a vacuum represented by the reference state (3.11); we will call these two species of quasi-particles "bare quasi-particles". The state (3.10) is then nothing but a scattering state of bare quasi-particles [155]. Bare quasi-particles of the first species contribute to the energy and momentum of the state, while those of the second species do not (*cf.* Eqs. (3.18)). Note that the two species of bare quasi-particles do not directly correspond to the two spin-flips $|0\rangle$ and $|\Downarrow\rangle$. Pictorially one could imagine that $|0\rangle$ is a bare quasi-particle of the first species and $|\Downarrow\rangle$ splits into a bare quasi-particle of the first and one of the second species.

3.1.2 String hypothesis and thermodynamic description

The thermodynamics of integrable models is naturally described within the well-known thermodynamic Bethe ansatz formalism [21]. Within this framework, the quasi-particle content of the model emerges in analogy with the case of non-interacting spin chains.

The thermodynamic Bethe ansatz for the nested system of interest in this Chapter has been widely studied in the literature, see, *e.g.*, Refs. [153, 154, 156–159]. Here we review the aspects which are relevant for our work. As usual, the starting point is provided by the so called string hypothesis, according to which, for large L, both sets of rapidities arrange themselves in the complex plane forming patterns called strings. In the present case the parametrization of the strings reads

$$k_\alpha^{n,\ell} = k_\alpha^n + i\left(\frac{n+1}{2} - \ell\right), \quad \ell = 1, \dots n\,, \qquad \alpha = 1, \dots, M_n^{(1)}\,, \tag{3.21}$$

$$\lambda_\alpha^{n,\ell} = \lambda_\alpha^n + i\left(\frac{n+1}{2} - \ell\right), \quad \ell = 1, \dots n\,, \qquad \alpha = 1, \dots, M_n^{(2)}\,. \tag{3.22}$$

Here the numbers $n = 1, 2, \dots, +\infty$ are labeling the string types, the real numbers k_α^n, λ_α^n are the string centers and $\{M_n^{(1)}, M_n^{(2)}\}$ are respectively the number of strings of the first and of the second species. Note that the strings here do *not* couple the

two different species of rapidities and for each species the strings have the the well-known structure encountered in the case of XXX spin-1/2 chain [21]. Physically, the different strings are interpreted as bound states of the bare quasi-particles (see *e.g.* Chapter IV in Ref. [23]).

Under the string hypothesis, the Bethe equations (3.17) can be turned into equations for the string centers; it is convenient to consider the logarithmic form of these equations which reads as [154]

$$z_n^{(1)}(k_\alpha^n) = \frac{2\pi}{L} I_\alpha^n \,, \qquad\qquad z_n^{(2)}(\lambda_\alpha^n) = \frac{2\pi}{L} J_\alpha^n \,. \tag{3.23}$$

Here $\{I_\alpha^n\}, \{J_\alpha^n\}$ are integers or semi-integers depending on $\{M_n^{(1)}, M_n^{(2)}\}$ and we introduced the *counting functions*

$$z_n^{(1)}(\lambda) = p_n(\lambda) - \frac{1}{L}\sum_{m=1}^{+\infty}\sum_{\beta=1}^{M_m^{(1)}} \Xi_{nm}(\lambda - k_\beta^m) + \frac{1}{L}\sum_{m=1}^{+\infty}\sum_{\beta=1}^{M_m^{(2)}} \Theta_{nm}(\lambda - \lambda_\beta^m) \,, \tag{3.24}$$

$$z_n^{(2)}(\lambda) = \frac{1}{L}\sum_{m=1}^{+\infty}\sum_{\beta=1}^{M_m^{(1)}} \Theta_{nm}(\lambda - k_\beta^m) - \frac{1}{L}\sum_{m=1}^{+\infty}\sum_{\beta=1}^{M_m^{(2)}} \Xi_{nm}(\lambda - \lambda_\beta^m) \,. \tag{3.25}$$

Here

$$p_n(\lambda) = 2\arctan\left(\frac{2\lambda}{n}\right) , \tag{3.26}$$

$$\Xi_{n,m}(\lambda) = (1\text{–}\delta_{nm})p_{|n-m|}(\lambda) + 2p_{|n-m|+2}(\lambda) + \ldots + 2p_{n+m-2}(\lambda) + p_{n+m}(\lambda) \,, \tag{3.27}$$

$$\Theta_{n,m}(\lambda) = p_{|n-m|+1}(\lambda) + p_{|n-m|+3}(\lambda) + \ldots + p_{n+m-1}(\lambda) \,. \tag{3.28}$$

The counting functions (3.24) and (3.25) are assumed to be monotonic for any solution of the equations (3.23). The range of $\{I_\alpha^n, J_\beta^m\}$ can be obtained taking the $\lambda \to \infty$ limit of the counting functions (and imposing $\{I_\alpha^n, J_\beta^m\}$ to be integers or semi-integers according to the values of $\{M_n^{(1)}, M_n^{(2)}\}$). The result reads as [159]

$$|I_\alpha^n| \;\leq\; \frac{1}{4}\left(2L - 2 + M_n^{(2)} - 2\sum_{m=1}^{+\infty} t_{nm} M_m^{(1)} + \sum_{m=1}^{+\infty} t_{nm} M_m^{(2)}\right) , \tag{3.29}$$

$$|J_\alpha^n| \;\leq\; \frac{1}{4}\left(M_n^{(1)} - 2 + \sum_{m=1}^{+\infty} t_{nm} M_m^{(1)} - 2\sum_{m=1}^{+\infty} t_{nm} M_m^{(2)}\right) , \tag{3.30}$$

where $t_{nm} \equiv 2\min(n,m) - \delta_{n,m}$. The energy and the momentum of a state described by the string centers $\{k_\alpha^n\}, \{\lambda_\alpha^n\}$ are given by

$$E = \sum_{m=1}^{+\infty}\sum_{\beta=1}^{M_m^{(1)}} \varepsilon_m(k_\beta^m) \,, \qquad\qquad P = \left[\sum_{m=1}^{+\infty}\sum_{\beta=1}^{M_m^{(1)}} \Big(p_m(k_\beta^m) - \pi\Big)\right] \bmod 2\pi \,, \tag{3.31}$$

where we introduced the bare energies [153]

$$\varepsilon_n(k) = -\frac{n}{k^2 + n^2/4} \,. \tag{3.32}$$

Finally, the eigenvalues of $\mathcal{N}_1$ and $\mathcal{N}_2$ read as

$$N_1 = \sum_{n=1}^{+\infty} n M_n^{(1)} , \qquad N_2 = \sum_{n=1}^{+\infty} n M_n^{(2)} . \tag{3.33}$$

In the thermodynamic limit the string centers become continuous variables on the real line. Accordingly, we introduce the rapidity distribution functions $\rho_n^{(1)}(k)$ and $\rho_n^{(2)}(k)$ which generalize the momentum distribution functions for free systems. Analogously, we also introduce the hole distribution functions $\rho_{h,n}^{(1)}(k)$ and $\rho_{h,n}^{(2)}(k)$, which corresponds to the distribution of holes (*i.e.* values of the rapidity for which there is no particle) in free Fermi gases at finite temperature. As customary, we define

$$\rho_{t,n}^{(r)}(k) = \rho_n^{(r)}(k) + \rho_{h,n}^{(r)}(k) , \quad r = 1, 2 , \quad n = 1, \ldots, +\infty , \tag{3.34}$$

as well as the functions

$$\vartheta_n^{(r)} = \frac{\rho_n^{(r)}(x)}{\rho_{t,n}^{(r)}(x)} , \quad r = 1, 2 , \quad n = 1, 2, \ldots, +\infty , \tag{3.35}$$

$$\eta_n^{(r)}(x) = \frac{\rho_{h,n}^{(r)}(x)}{\rho_n^{(r)}(x)} , \quad r = 1, 2 , \quad n = 1, 2, \ldots, +\infty . \tag{3.36}$$

Particle and hole distribution functions of the two species can not be chosen arbitrarily, but are constrained by a set of linear integral equations which are nothing but the thermodynamic version of the Bethe equations (3.17). They are usually called Bethe-Takahashi equations and are derived in complete analogy with the XXX spin-1/2 case [21]. They read [158]

$$\rho_{t,n}^{(1)}(\lambda) = a_n(\lambda) - \sum_{m=1}^{\infty} \left(a_{n,m} * \rho_m^{(1)}\right)(\lambda) + \sum_{m=1}^{\infty} \left(b_{n,m} * \rho_m^{(2)}\right)(\lambda) , \tag{3.37}$$

$$\rho_{t,n}^{(2)}(\lambda) = -\sum_{m=1}^{\infty} \left(a_{n,m} * \rho_m^{(2)}\right)(\lambda) + \sum_{m=1}^{\infty} \left(b_{n,m} * \rho_m^{(1)}\right)(\lambda) . \tag{3.38}$$

Here we defined the convolution between two functions as

$$(f * g)(\lambda) = \int_{-\infty}^{\infty} \mathrm{d}\mu f(\lambda - \mu) g(\mu) , \tag{3.39}$$

and

$$a_{n,m}(\lambda) = (1 - \delta_{nm}) a_{|n-m|}(\lambda) + 2a_{|n-m|+2}(\lambda) + \ldots + 2a_{n+m-2}(\lambda) + a_{n+m}(\lambda) , \tag{3.40}$$

$$b_{n,m}(\lambda) = a_{|n-m|+1}(\lambda) + a_{|n-m|+3}(\lambda) + \ldots + a_{n+m-1}(\lambda) , \tag{3.41}$$

where

$$a_n(\lambda) = \frac{1}{2\pi} \frac{n}{\lambda^2 + n^2/4} . \tag{3.42}$$

Following [21], the Bethe-Takahashi equations (3.37), (3.38) can also be cast in partially decoupled form which is more convenient for numerical analysis. They read

$$\rho^{(1)}_{t,n}(\lambda) = \delta_{n,1} s(\lambda) + s * \left(\rho^{(1)}_{h,n-1} + \rho^{(1)}_{h,n+1}\right)(\lambda) + s * \rho^{(2)}_{n}(\lambda)\,, \tag{3.43}$$

$$\rho^{(2)}_{t,n}(\lambda) = s * \left(\rho^{(2)}_{h,n-1} + \rho^{(2)}_{h,n+1}\right)(\lambda) + s * \rho^{(1)}_{n}(\lambda)\,, \tag{3.44}$$

where we use the conventions

$$\rho^{(r)}_{h,0}(\lambda) \equiv 0\,, \qquad (r = 1, 2)\,, \tag{3.45}$$

and the function

$$s(\lambda) = \frac{1}{2\cosh(\pi\lambda)}\,. \tag{3.46}$$

The set of rapidity distribution functions completely characterizes the thermodynamic properties of a given macrostate. In particular, the density of the quasi-particles of the species (1) and (2) can be computed as

$$D^{(1)} = \frac{N_1}{L} = \sum_{n=1}^{+\infty} n \int_{-\infty}^{+\infty} \mathrm{d}k\ \rho^{(1)}_n(k)\,, \tag{3.47}$$

$$D^{(2)} = \frac{N_2}{L} = \sum_{n=1}^{+\infty} n \int_{-\infty}^{+\infty} \mathrm{d}\lambda\ \rho^{(2)}_n(\lambda)\,. \tag{3.48}$$

For later convenience, it is also useful to introduce the density of particles forming bound states as

$$D^{(r)}_n = n \int_{-\infty}^{+\infty} \mathrm{d}k\ \rho^{(r)}_n(k)\,. \tag{3.49}$$

Analogously, by means of the string hypothesis, one can obtain the density of energy from (3.31) as

$$\frac{E}{L} = \sum_{n=1}^{+\infty} \int_{-\infty}^{+\infty} \mathrm{d}k\ \rho^{(1)}_n(k)\varepsilon_n(k)\,. \tag{3.50}$$

3.2 The quench protocol

We are now interested in the standard quench dynamics where the system is prepared in an initial state $|\Psi_0\rangle$, which is not an eigenstate of the Hamiltonian, and then it is let evolve for $t > 0$ with the Lai-Sutherland Hamiltonian (3.1). The main goal of our analysis is not to reconstruct the entire time evolution, which is currently out of reach, but just to have an exact characterization of the stationary state.

As we have seen in Section 1.3, to tackle this problem, we have two possible strategies. Either we rely on the knowledge of the expectation value of a complete set of quasi-local charges or we construct the stationary state from the Quench Action. Concerning the former approach, while we expect that quasi-local charges might be successfully employed also in the study of quenches to the $SU(3)$ chain

(3.1), a systematic analysis of this problem (*i.e.* a systematic characterization and classification of the quasi-local charges) in the case of nested systems has not yet been carried out. As a consequence, we can only rely on the Quench Action approach [33], which can be implemented quite generally for any Bethe ansatz integrable model, but is limited to those quenches for which the overlap between the initial state and the Bethe eigenstates are known exactly. In the following we then restrict ourselves to consider a special initial state for which these overlaps are known. Indeed, an exact formula has been conjectured and tested in [160] in the context of the AdS/CFT correspondence. While the special initial state that we consider is admittedly artificial, we will see that it has a very simple structure. This, in turn, makes it possible to test our theoretical predictions by means of efficient numerical methods.

3.2.1 The Quench Action functional

As we have discussed in Section 1.3, the long-time steady state after the quench is described by the saddle point of the Quench Action functional. The Quench Action functional explicitly depends on the initial state $|\Psi_0\rangle$ and on some symmetry properties of the latter. In the case considered, it reads

$$s_{\rm QA}[\boldsymbol{\rho}] = 2\mathcal{E}[\boldsymbol{\rho}] - \frac{1}{2} s_{\rm YY}[\boldsymbol{\rho}]\,, \tag{3.51}$$

where we have indicated with compact notation $\boldsymbol{\rho}$ the sets $\{\rho_n^{(1)}\}_{n=1}^{\infty}$, $s\{\rho_n^{(2)}\}_{n=1}^{\infty}$. Here $s_{\rm YY}[\boldsymbol{\rho}]$ is the Yang-Yang entropy [153]

$$s_{\rm YY}\left[\boldsymbol{\rho}\right] = \sum_{r=1}^{2}\sum_{n=1}^{+\infty}\int_{-\infty}^{+\infty}{\rm d}\lambda\,\left\{\rho_{{\rm t},n}^{(r)}\ln\rho_{{\rm t},n}^{(r)} - \rho_n^{(r)}(\lambda)\ln\rho_n^{(r)} - \rho_{h,n}^{(r)}\ln\rho_{h,n}^{(r)}\right\}\,. \tag{3.52}$$

Note that the factor $1/2$ in front of the Yang-Yang entropy in (3.51) comes from the fact that the initial state $|\Psi_0\rangle$ has non-vanishing overlaps only with microscopically parity-symmetric Bethe states (see (1.76)). The number of parity-invariant microscopic realizations corresponding to a macrostate is the square root of the total number of realizations. The first term in (3.51) is defined in terms of the thermodynamically leading part of the overlap between the initial state $|\Psi_0\rangle$ and the Bethe state corresponding to $|\boldsymbol{\rho}\rangle$ as follows

$$\mathcal{E}[\boldsymbol{\rho}] = -\lim_{\rm th}\frac{1}{L}{\rm Re}\left[\ln\langle\Psi_0|\boldsymbol{\rho}\rangle\right]\,. \tag{3.53}$$

This expression has to be interpreted as the thermodynamic limit of the logarithm of the overlap between $|\Psi_0\rangle$ and a Bethe state which corresponds to the functions $\{\rho_n^{(1)}\}_{n=1}^{\infty}$ and $\{\rho_n^{(2)}\}_{n=1}^{\infty}$. The post-quench steady state is then described by the distributions $\bar\rho_n^{(r)}(\lambda)$ which are the saddle-point of the Quench Action (3.51), namely the solution of the system of equations

$$\left.\frac{\partial s_{QA}[\boldsymbol{\rho}]}{\partial\rho_n^{(r)}(\lambda)}\right|_{\boldsymbol{\rho}=\bar{\boldsymbol{\rho}}} = 0, \qquad r=1,2\,, \qquad n\geq 1. \tag{3.54}$$

In the next subsection, we will explicitly write the Quench Action for the initial state studied in this Chapter, and derive the corresponding saddle-point equations.

3.2.2 The initial state and the saddle-point equations

We consider the following initial state for our quench problem

$$\begin{aligned} |\Psi_0\rangle &= \frac{1}{\sqrt{\mathcal{N}}}\,\mathrm{tr}_0\left[\prod_{j=1}^{L}\left(\sigma^1\,|\Uparrow\rangle_j + \sigma^2\,|0\rangle_j + \sigma^3\,|\Downarrow\rangle_j\right)\right] \\ &= \frac{1}{\sqrt{\mathcal{N}}}\sum_{\{\alpha_j\}}\mathrm{tr}_0\left[\sigma^{\alpha_1}\sigma^{\alpha_2}\ldots\sigma^{\alpha_L}\right]|e_{\alpha_1}e_{\alpha_2}\ldots e_{\alpha_L}\rangle\,. \end{aligned} \tag{3.55}$$

Here we used the notations (3.4) and (3.5), while σ^α are the Pauli matrices

$$\sigma^1 = \begin{pmatrix} 0 & 1 \\ 1 & 0 \end{pmatrix}, \quad \sigma^2 = \begin{pmatrix} 0 & -i \\ i & 0 \end{pmatrix}, \quad \sigma^3 = \begin{pmatrix} 1 & 0 \\ 0 & -1 \end{pmatrix}, \tag{3.56}$$

so that the trace in (3.55) is over the auxiliary space $h_0 \simeq \mathbb{C}^2$. Finally, the normalization $\mathcal{N} = 3^L + 3(-1)^L$ is chosen such that $\langle\Psi_0|\Psi_0\rangle = 1$.

The initial state (3.55) is a matrix product state with local dimension 2 which satisfies cluster decomposition. The simple structure of $|\Psi_0\rangle$ allows for the investigation of its time evolution by means of efficient numerical methods such as DMRG and iTEBD simulations [161–163]. Consider a chain of length L and a Bethe state characterized by the rapidities $\{k_j\}_{j=1}^N, \{\mu_j\}_{j=1}^M$ such that L, N and M are even numbers and

$$\{k_j\}_{j=1}^N = \{-k_j\}_{j=1}^N\,, \tag{3.57}$$

$$\{\mu_j\}_{j=1}^M = \{-\mu_j\}_{j=1}^M\,. \tag{3.58}$$

Then, its overlap with the initial state (3.55) is given by [160]

$$\langle\Psi_0|\{k_j\}_{j=1}^N, \{\mu_j\}_{j=1}^M\rangle = \frac{2}{\sqrt{\mathcal{N}}}\sqrt{\left[\prod_{m=1}^{N/2}\frac{k_m^2+1/4}{k_m^2}\right]\left[\prod_{m=1}^{M/2}\frac{\mu_m^2+1/4}{\mu_m^2}\right]\frac{\det G_+}{\det G_-}}\,. \tag{3.59}$$

Here $G_\pm$ are Gaudin-like matrices defined by

$$G_\pm = \begin{pmatrix} A_\pm & B_\pm \\ B_\pm^t & C_\pm \end{pmatrix}, \tag{3.60}$$

where

$$(A_\pm)_{r,s} = \delta_{rs}\left[L\mathcal{K}_1(k_r) - \sum_{l=1}^{N/2}\mathcal{K}_2^+(k_r,k_l) + \sum_{l=1}^{M/2}\mathcal{K}_1^+(k_r,\lambda_l)\right] + \mathcal{K}_2^\pm(k_r,k_s)\,, \tag{3.61}$$

$$(B_\pm)_{r,s} = -\mathcal{K}_1^\pm(k_r,\lambda_s)\,, \tag{3.62}$$

$$(C_\pm)_{r,s} = \delta_{rs}\left[-\sum_{l=1}^{M/2}\mathcal{K}_2^+(\lambda_r,\lambda_l) + \sum_{l=1}^{M/2}\mathcal{K}_1^+(\lambda_r,k_l)\right] + \mathcal{K}_2^\pm(\lambda_r,\lambda_s)\,, \tag{3.63}$$

with the additional definitions

$$\mathcal{K}_1(u) = \frac{1}{u^2+1/4}\,, \tag{3.64}$$

$$\mathcal{K}_2(u) = \frac{2}{u^2+1}\,, \tag{3.65}$$

$$\mathcal{K}_s^{\pm}(u,w) = \mathcal{K}_s(u-w) \pm \mathcal{K}_s(u+w)\,, \quad s=1,2\,. \tag{3.66}$$

An analogous formula exists for the case where N is even, while L and M are odd, and the sets of rapidity distributions still satisfy (3.57), (3.58). Conversely, for Bethe states not satisfying (3.57), (3.58) the overlap is zero [160]. Formula (3.59) was conjectured in [160] based on an analogy with the case of the XXX spin-1/2 chain, where a similar state can be constructed and the corresponding overlaps computed [164–166].

It is not simple to extract from (3.59) the thermodynamically leading part of the overlap. In fact, due to divergences arising in the matrices $G_{\pm}$, one should take into account finite-size deviations from perfect strings (3.21), (3.22). Note however that the situation is completely analogous to the one encountered in other models displaying bound states. This is, for instance, the case for quenches from the Néel state to the XXZ spin-1/2 chain [57, 138] or from non-interacting to attractive one-dimensional Bose gases [90, 167]. Following these works, it can be argued that the ratio of the determinants in (3.59) only gives a sub-leading contribution in the thermodynamic limit and can thus be neglected. Given the similarity of the argument, we do not report it here, and refer to [57, 90, 138, 167] for more details.

Dropping the ratio of the determinants, it is straightforward to take the thermodynamic limit of (3.59). Since the calculations are analogous to the ones performed in [90, 138, 167], here we only report the final result, which reads

$$\begin{aligned}\mathcal{E}\left[\boldsymbol{\rho}\right] &\equiv -\ln\left(\langle\Psi_0|\{\rho_n^{(r)}\}_{n=1}^{\infty}\rangle\right)\\ &= \frac{1}{2}\ln 3 + \frac{1}{4}\sum_{n=1}^{\infty}\int_{-\infty}^{\infty}\mathrm{d}k\rho_n^{(1)}(k)g_n(k) + \frac{1}{4}\sum_{n=1}^{\infty}\int_{-\infty}^{\infty}\mathrm{d}\lambda\rho_n^{(2)}(\lambda)g_n(\lambda)\,,\end{aligned} \tag{3.67}$$

where we defined

$$g_n(\lambda) = \sum_{l=0}^{n-1}\Big[f_{n-1-2l}(\lambda) - f_{n-2l}(\lambda)\Big]\,, \tag{3.68}$$

$$f_n(\lambda) = \ln\left(\lambda^2 + n^2/4\right). \tag{3.69}$$

From (3.51), we see that we have now all the elements necessary to explicitly write down the saddle-point equations (3.54). Putting all together, we can explicitly perform the functional derivative in (3.54) and obtain the desired saddle-point equations. By exploiting the Bethe-Takahashi equations (3.37) and (3.38) we finally

obtain

$$\ln \eta_n^{(1)} = g_n + \sum_{m=1}^{+\infty} \left[a_{n,m} * \ln\left(1 + 1/\eta_m^{(1)}\right)\right] - \sum_{m=1}^{+\infty} \left[b_{n,m} * \ln\left(1 + 1/\eta_m^{(2)}\right)\right] , \quad (3.70)$$

$$\ln \eta_n^{(2)} = g_n + \sum_{m=1}^{+\infty} \left[a_{n,m} * \ln\left(1 + 1/\eta_m^{(2)}\right)\right] - \sum_{m=1}^{+\infty} \left[b_{n,m} * \ln\left(1 + 1/\eta_m^{(1)}\right)\right] , \quad (3.71)$$

where the functions $a_{n,m}$ and $b_{n,m}$ are defined in (3.40) and (3.41) respectively.

Once again, Eqs. (3.70) and (3.71) can be cast in a partially decoupled form which is more suitable for numerical evaluation, *i.e.*,

$$\ln \eta_n^{(1)} = d_n + s * \left(\ln[1 + \eta_{n-1}^{(1)}] + \ln[1 + \eta_{n+1}^{(1)}]\right) - s * \ln\left[1 + 1/\eta_n^{(2)}\right] , \quad (3.72)$$

$$\ln \eta_n^{(2)} = d_n + s * \left(\ln[1 + \eta_{n-1}^{(2)}] + \ln[1 + \eta_{n+1}^{(2)}]\right) - s * \ln\left[1 + 1/\eta_n^{(1)}\right] , \quad (3.73)$$

where $s(\lambda)$ is defined in (3.46), and we introduced

$$d_n(\lambda) = (-1)^{n+1} \ln\left[\tanh^2\left(\frac{\pi\lambda}{2}\right)\right] , \quad (3.74)$$

with the convention

$$\eta_0^{(r)}(\lambda) \equiv 0 . \quad (3.75)$$

One can immediately see that (3.70) are (3.71) are symmetric under exchanging the particle species (1) $\leftrightarrow$ (2). This observation allows us to simplify the saddle-point equations as follows. Suppose we find a solution $\eta_n^{(1)}(\lambda) = \Theta_n(\lambda)$, $\eta_n^{(2)}(\lambda) = \Xi_n(\lambda)$. If $\Theta_n(\lambda) \neq \Xi_n(\lambda)$, then we find another solution $\eta_n^{(1)}(\lambda) = \Xi_n(\lambda)$, $\eta_n^{(2)}(\lambda) = \Theta_n(\lambda)$. We rule out this possibility by assuming uniqueness of the solution of (3.70) and (3.71). Hence, we conclude that the two sets of functions coincide, namely

$$\eta_n^{(1)}(\lambda) = \eta_n^{(2)}(\lambda) \equiv \eta_n(\lambda) . \quad (3.76)$$

As a consequence, one can write a unique set of non-linear integral equations for $\eta_n(\lambda)$. From (3.43) and (3.44) it follows

$$\ln \eta_n = d_n + s * (\ln[1 + \eta_{n-1}] + \ln[1 + \eta_{n+1}]) - s * \ln\left[1 + \eta_n^{-1}\right] . \quad (3.77)$$

The corresponding root densities $\rho_n^{(1)}(\lambda)$ and $\rho_n^{(2)}(\lambda)$ are found by solving the Bethe-Takahashi equations (3.37)–(3.38). Note that, even if $\eta_n^{(1)}(\lambda) = \eta_n^{(2)}(\lambda)$, the root densities will generically be *different* due to the asymmetric form of (3.37)–(3.38).

The single set of decoupled equations (3.77) easily allows us to understand the asymptotic behavior of $\eta_n(\lambda)$ for large λ and n. Defining

$$\eta_{n,\infty} = \lim_{|\lambda|\to\infty} \eta_n(\lambda) , \quad (3.78)$$

and taking the limit $|\lambda| \to \infty$ in (3.77), one obtains the set of algebraic equations

$$\eta_{n,\infty}(1 + \eta_{n,\infty}) = (1 + \eta_{n-1,\infty})(1 + \eta_{n+1,\infty}), \quad (3.79)$$

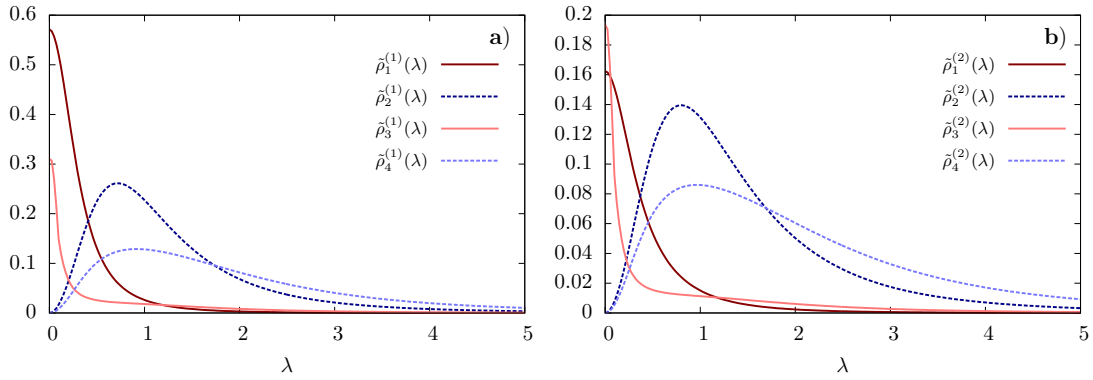

Figure 3.1: Rapidity distribution functions of the post-quench steady state. Left and right panels show the *rescaled* root densities $\tilde{\rho}_n^{(r)}(\lambda)$ of the first four string types $n = 1, 2, 3, 4$ for the two species of rapidities $r = 1, 2$ describing the eigenstates of our system. Rescaled root densities are defined as $\tilde{\rho}_n^{(r)}(\lambda) = n^2\bar{\rho}_n^{(r)}$ for odd n and $\tilde{\rho}_n^{(r)} = 10n^2\bar{\rho}_n^{(r)}(\lambda)$ for even n. The rescaling is performed to show all the root densities on the same plot. (Figure taken from [88].)

with $\eta_{0,\infty} = 0$. It is straightforward to verify that the following ansatz satisfy (3.79)

$$\eta_{n,\infty} = \frac{(n+1)(n+2)}{2} - 1\,. \tag{3.80}$$

As we discuss in the following, Eq. (3.80) is recovered by our numerical solution of (3.77).

3.3 The post-quench steady state

Our strategy to numerically determine the saddle-point root densities is straightforward. First, we solve Eq. (3.77) for $\eta_n^{(r)}(\lambda)$ and then we find $\rho_n^{(r)}(\lambda)$, $\rho_{h,n}^{(r)}(\lambda)$ by solving the partially decoupled Bethe equations (3.44) – (3.45). For the sake of presentation, details on our numerical solution of (3.77) and (3.44) – (3.45) are postponed to Sec. 3.3.2, while here we present and discuss the final result.

The rapidity distribution functions $\rho_n^{(1)}(\lambda)$, $\rho_n^{(2)}(\lambda)$ characterizing the post-quench steady state are displayed in Fig. 3.1. Note that we have rescaled the rapidity distributions corresponding to bound particles, as they are significantly smaller than those of unbound particles. The knowledge of these rapidity distributions in principle allows us to compute the long-time limit of any local observable after the quench.

The bound-state content of the post-quench steady state is displayed in Fig. 3.2. The density of unbound particles is the prominent one, even though finite densities of n-particle bound-states are non-negligible for small n. Also note that the sequence of densities is not monotonic in n, but displays an even/odd effect.

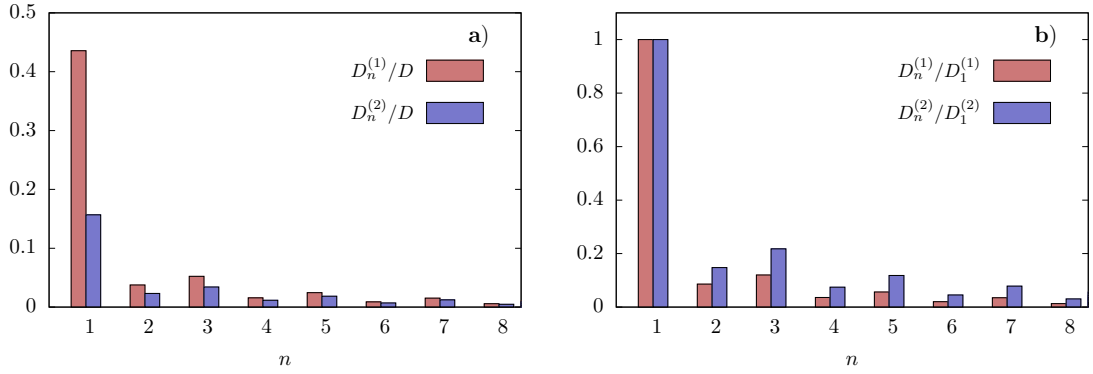

Figure 3.2: Normalized contributions $D_n^{(1)}$, $D_n^{(2)}$ [defined in (3.49)] of the bound particles to the densities $D^{(1)}$ and $D^{(2)}$. The plots show that the density of n-particle bound states rapidly decreases with n, while the value of $D_n^{(2)}$ is always comparable to that of $D_n^{(1)}$. (Figure taken from [88].)

The post-quench steady state lies in the same magnetization sector of the ground-state of the model: they both have $D^{(1)} = 2/3$ and $D^{(2)} = 1/3$ [153]. The ground-state, however, displays absence of bound-states so that $\rho_n^{(1)}(\lambda) \equiv \rho_n^{(2)}(\lambda) \equiv 0$ for $n \geq 2$. A comparison between the rapidity distributions $\rho_1^{(1)}(\lambda)$, $\rho_1^{(2)}(\lambda)$ of the ground-state and the steady state is displayed in Fig. 3.3. We see that even though higher bound-states have small densities in the steady state they significantly influence the rapidity distribution $\rho_1^{(2)}(\lambda)$ of the second species of particles.

In the next subsection, we discuss on the computation of the local conserved operators both on the initial and the post-quench steady state. This will be crucial in order to test the validity of Eq. (3.77) and the accuracy of our numerical solution. Next, we provide further details on the numerical scheme employed to solve the saddle-point integral equations.

3.3.1 The local conserved charges

Since our system is integrable, there exists an infinite number of local and quasi-local conserved operators, or charges, commuting with the Hamiltonian. Let us focus only on the local charges and indicate them as $\{Q_n\}_n$, where $Q_2 = H$ by convention. Since these operators are conserved, their expectation values on the initial state and on the long-time stationary state have to be equal. This fact provides the basis for the main test of the validity of our results.

In Appendix 3.A we derive the following expression for the expectation value of a given charge on a Bethe state

$$\lim_{L\to\infty} \frac{1}{L} \langle |\{\rho_n^{(r)}\}|Q_m|\{\rho_n^{(r)}\}\rangle = \sum_{n=1}^{\infty} \int_{-\infty}^{+\infty} \mathrm{d}\lambda \left(\rho_n^{(1)}(\lambda) c_{m,n}^{(1)}(\lambda) + \rho_n^{(2)}(\lambda) c_{m,n}^{(2)}(\lambda)\right) , \quad (3.81)$$

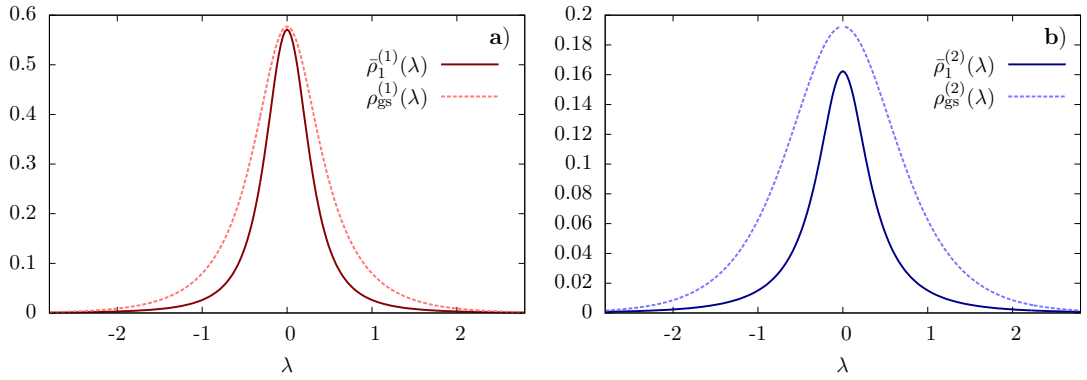

Figure 3.3: Comparison between the rapidity distribution functions $\rho_1^{(1)}(\lambda)$, $\rho_1^{(2)}(\lambda)$ of the ground-state and the post-quench steady state. The plot shows that in the steady state the density of unbound particles is smaller, as it contains non-negligible densities of bound-states, *c.f.* Fig. 3.2 (Figure taken from [88].)

where

$$c^{(1)}_{m+1,n}(k) = (-1)^m i \frac{\partial^m}{\partial \lambda^m} \log\left[\frac{k+in/2}{k-in/2}\right], \qquad m \geq 1\,, \tag{3.82}$$

$$c^{(2)}_{m+1,n}(\lambda) \equiv 0\,, \qquad m \geq 1\,. \tag{3.83}$$

We indicated with $|\{\rho_n^{(r)}\}\rangle$ a Bethe state which corresponds to the rapidity distributions $\{\rho_n^{(r)}\}$ in the thermodynamic limit. Note that the second species of particles does not contribute to the value of any of the local conserved charges. Equations (3.81), (3.82) and (3.83) immediately allow us to numerically compute, after integration, the value of the charges on the post-quench steady state.

In order to compute the expectation value of the local charges on the initial state, we exploit the method outlined in [54] for the case of the XXZ spin-1/2 chain. As discussed in Appendix 3.B, we find that the same method can straightforwardly be applied also in our case. First, we define the generating function $\Omega_{\Psi_0}(\lambda)$ such that

$$\frac{\partial^n}{\partial \lambda^n}\Omega_{\Psi_0}(\lambda)\Big|_{\lambda=0} = \lim_{L\to\infty}\frac{1}{L}\langle\Psi_0|Q_{n+2}|\Psi_0\rangle\,. \tag{3.84}$$

Then, we show (*cf.* Appendix 3.B) that the generating function has the following simple expression

$$\Omega_{\Psi_0}(\lambda) = -\frac{4(3+2\lambda^2)}{3(3+7\lambda^2+4\lambda^4)}\,. \tag{3.85}$$

From (3.85) we immediately obtain

$$\lim_{L\to\infty}\frac{1}{L}\langle\Psi_0|Q_{2k+1}|\Psi_0\rangle = 0\,, \quad k = 1,2,\ldots\infty\,, \tag{3.86}$$

together with the explicit expression of the even charges. As an example we report the first few charges, *i.e.*,

$$\lim_{L\to\infty}\frac{1}{L}\langle\Psi_0|Q_2|\Psi_0\rangle = -\frac{4}{3}\,, \tag{3.87}$$

$$\lim_{L\to\infty}\frac{1}{L}\langle\Psi_0|Q_4|\Psi_0\rangle = \frac{40}{9}\,, \tag{3.88}$$

$$\lim_{L\to\infty}\frac{1}{L}\langle\Psi_0|Q_6|\Psi_0\rangle = -\frac{736}{9}\,. \tag{3.89}$$

We can also readily write down two additional local conserved charges which are independent from the operators Q_n. These are $\mathcal{N}_1$ and $\mathcal{N}_2$ defined in (3.7) and (3.8). The expression for their expectation value on Bethe states is given in (3.47) and (3.48). In addition, by exploiting the simple matrix product form of the initial state, it is easy to compute that

$$\lim_{L\to\infty}\frac{1}{L}\langle\Psi_0|\mathcal{N}_1|\Psi_0\rangle = \frac{2}{3}\,, \tag{3.90}$$

$$\lim_{L\to\infty}\frac{1}{L}\langle\Psi_0|\mathcal{N}_2|\Psi_0\rangle = \frac{1}{3}\,. \tag{3.91}$$

As we will discuss in the next subsection, all these values are correctly recovered by our numerical solution for the steady state rapidity distributions (3.77).

3.3.2 The numerical solution

The partially decoupled version of TBA integral equations is in general more convenient from the numerical point of view. Nevertheless, as a general rule we have always solved both the coupled and partially decoupled versions for all the integral equations that we have considered. The agreement between the two results gives us a useful check for our numerical methods.

All the systems considered in this Chapter feature an infinite number of equations, therefore, to provide a numerical solution one needs to "truncate" them retaining only a finite number $N_{\rm eq}$ of equations. The solution to the truncated system, indicated by $X_n(\lambda)$, is then an approximation to the exact result and becomes exact in the limit $N_{\rm eq}\to\infty$. The partially decoupled version of the integral equations allows us to consider larger $N_{\rm eq}$ and usually allows to reach better accuracy. The agreement between the numerical solution of the coupled and partially decoupled equations is almost perfect for the functions $X_n(\lambda)$ with $n < N_{\rm eq}$ and n not too close to $N_{\rm eq}$, while small discrepancies arise for $X_n(\lambda)$ with $n \lesssim N_{\rm eq}$ due to the effect of truncation. In the following we briefly comment on our numerical solution of the partially decoupled equations, which yielded our most accurate results.

First, we solved the saddle point equations (3.77) for $\eta_n^{(r)}(\lambda)$ using successive iterations. The truncation procedure followed here is analogous to that of Refs. [57, 138]. Since the driving terms $d_n(\lambda)$ in (3.77) are all equal for n of a given parity, it is natural to expect the same even/odd effect to be present for the solutions $\eta_n(\lambda)$. In particular, one expects that for large n it holds $\eta_n/\eta_{n+2}\sim 1$. More precisely,

based on the asymptotic behavior (3.80), we truncated the equations (3.77) using the condition

$$\frac{\eta_{N_{\rm Eq}+1}(\lambda)}{\eta_{N_{\rm Eq}-1}(\lambda)} = \frac{\eta_{N_{\rm Eq}+1,\infty}}{\eta_{N_{\rm Eq}-1,\infty}} = 1 + \frac{4}{N_{\rm eq}} + O\left(\frac{1}{N_{\rm eq}^2}\right) . \tag{3.92}$$

We checked that for fixed n and λ the value $\eta_n(\lambda)$ converges to a well defined number increasing $N_{\rm eq}$. In addition, the solution obtained using (3.92) is consistent with the one of the coupled version of the integral equations (3.77).

The second step of the numerical solution is to apply the same iterative technique to the partially decoupled Bethe-Takahashi equations (3.43)-(3.44) determining $\rho_n^{(r)}(\lambda)$. The truncation in this case is performed in the standard fashion

$$\rho_{t,N_{\rm Eq}+1}(\lambda) = \rho_{t,N_{\rm Eq}}(\lambda) . \tag{3.93}$$

Note that, while the functions $\eta_n^{(r)}(\lambda)$ and $\rho_n^{(r)}(\lambda)$ live on the real line, their numerical realization is taken on an evenly distributed mesh of $N_{\rm points}$ points on a finite interval $[-\Lambda, \Lambda]$. Extrapolation of $\eta_n^{(r)}(\lambda)$ and $\rho_n^{(r)}(\lambda)$ in $N_{\rm points} \to \infty$ is necessary to obtain an accurate solution, while the other two parameters Λ and $N_{\rm eq}$ are fixed to reasonably large values. The results shown in the figures are computed using $\Lambda = 50$ and $N_{\rm eq} = 40$.

We tested our numerical solution by comparing the theoretical expectation values of the conserved charges (3.87)-(3.89) to the corresponding numerical results obtained via (3.81). After the extrapolation of $\rho_n^{(r)}(\lambda)$ to $N_{\rm points} \to \infty$, the numerical values of the charges have less than 1% error. The expectation values of $\mathcal{N}_1$ and $\mathcal{N}_2$ are slightly less accurate as they receive significant contributions from higher strings whose densities are affected by the truncation in the number of equations. Choosing the parameters as specified above, the errors in the expectation values of the particle numbers are 3.6% for the first species and 6.2% for the second. As an additional test of the numerical solution, we checked that the quench action (3.51) evaluated at the saddle point is indeed zero, *i.e.*, the two terms appearing in the difference (3.51) are equal. After the extrapolation of the densities to $N_{\rm points} \to \infty$ we find that the difference between the overlap and the entropy term in (3.51) is less than 1% of each term.

3.4 Entanglement Dynamics and Elementary Excitations

In this section we exploit the knowledge of the post-quench stationary state, determined in the above section, to investigate the finite-time dynamics of the system after the quench. We focus on the time evolution of the entanglement entropy after the quench. The amount of entanglement between a subsystem A and the rest of the system $\bar{A}$, is measured by the the entanglement entropy $S_A(t)$ defined as

$$S_A(t) = -\mathrm{Tr}[\rho_A(t) \ln \rho_A(t)] , \tag{3.94}$$

where $\rho_A(t)$ is the time evolving density matrix of the system reduced to the subsystem A, *i.e.* $\rho_A \equiv \mathrm{Tr}_{\bar{A}}|\Psi(t)\rangle\langle\Psi(t)|$. This entanglement entropy is known to give very important information about the system, both in and out of equilibrium, see, *e.g.*, the reviews [168–171].

A convenient way to describe the evolution of entanglement is by means of the quasi-particle picture originally proposed in Ref. [172–174]. In essence, one postulates that the quench creates pairs of correlated quasi-particles in any spacial point of the system. Only pairs created at the same point are correlated and carry entanglement through the system. For $t > 0$, the quasi-particles move ballistically in opposite directions and, as a consequence of momentum conservation, the two correlated quasi-particles have opposite velocities $\pm v(\lambda)$, where λ is the rapidity parametrising the dispersion relation. When moving through the system, the quasi-particles correlate regions which were initially uncorrelated as pictorially shown in Fig. 3.4. The entanglement entropy S_A is then a weighted (by a function $s(\lambda)$) measure of the number of pairs with one quasi-particle in A and the other in $\bar{A}$. It has been shown in many non-interacting models [175–179], that the predictions of the this quasi-particle picture become *exact* in the space-time scaling limit of large times and subsystem sizes. Furthermore the qualitative picture for the entanglement entropy evolution has been shown to be correct even in numerical simulations of many interacting integrable and non-integrable models, as *e.g.* in Refs. [180–184]. The same picture also provides the entanglement dynamics in local quenches [185–188] and in inhomogeneous situations [189].

In Ref. [141] it has been shown that the quasi-particle picture gives, in the space-time scaling limit, exact predictions even for interacting integrable models, provided that an appropriate choice for the functions $v(\lambda)$ and $s(\lambda)$ is made. One has to introduce multiple species of quasi-particles moving at the velocities $v_n(\lambda)$, which are the group velocities of elementary excitations over the stationary state described by $\{\bar{\rho}_n(\lambda)\}$. In interacting models the velocities $v_n(\lambda)$ are generically state-dependent and non-trivially encode the effects of the interactions – they fulfil a set of integral equations depending on $\{\bar{\rho}_n(\lambda)\}$. In the non-interacting limit they reduce to the bare velocities $v_n^0(\lambda) = \varepsilon_n'(\lambda)/p_n'(\lambda)$, where $\varepsilon_n(\lambda)$ and $p_n(\lambda)$ are respectively the bare energy and momentum. The choice of the quasi-particles' velocities is in agreement with the one found in transport problems [31, 32, 190] and it is ultimately related to the fundamental observation [30] that the group velocities of the elementary excitations are the relevant velocities for the propagation of information in interacting integrable models. The natural choice for the weighting functions $s_n(\lambda)$ is to set them equal to the Yang-Yang entropy density per rapidity and species. This choice guarantees that the extensive parts of entanglement entropy and thermodynamic entropy coincide at infinite times, in agreement with some general expectations [191, 192] as well as analytical findings in non-interacting models [176, 193, 194].

Here we assume that the quasi-particle picture holds true also for nested systems and we apply it to our case. This assumption can be independently checked numerically using methods based on matrix product states, such as the time-dependent density matrix renormalization group (tDMRG) or the infinite time-evolving block

decimation (iTEBD). Using the quasi-particle picture we write the entanglement entropy between a subsystem of contiguous spins of length ℓ and the rest of the system as

$$S_\ell(t) = 2t \sum_{r=1,2} \sum_{n=1}^{\infty} \int \mathrm{d}\lambda \; s_n^{(r)}(\lambda) |v_n^{(r)}(\lambda)| \, \Theta_{\mathrm{H}}(\ell - 2|v_n^{(r)}(\lambda)|t) \tag{3.95}$$

$$+ \ell \sum_{r=1,2} \sum_{n=1}^{\infty} \int \mathrm{d}\lambda \; s_n^{(r)}(\lambda) \, \Theta_{\mathrm{H}}(2|v_n^{(r)}(\lambda)|t - \ell) \, , \tag{3.96}$$

where $\Theta_{\mathrm{H}}(x)$ is the Heaviside function. We used the fact that the indices labeling quasi-particles are $n = 1, 2, \ldots$ and $r = 1, 2$. The Yang-Yang entropy density $s_n^{(r)}(\lambda)$ appearing in (3.96) is given by

$$s_n^{(r)}(\lambda) = \left(\rho_n^{(r)}(x) + \rho_{h,n}^{(r)}\right) \ln\left(\rho_n^{(r)}(x) + \rho_{h,n}^{(r)}\right) - \rho_n^{(r)} \ln \rho_n^{(r)} - \rho_{h,n}^{(r)} \ln \rho_{h,n}^{(r)} \, , \tag{3.97}$$

and velocities $v_n^{(1)}(\lambda)$ and $v_n^{(2)}(\lambda)$ fulfil the integral equations (cf. (1.63))

$$\rho_{t,n}^{(2)}(\lambda) v_n^{(2)}(\lambda) = \sum_k \left(b_{n,k} * v_k^{(1)} \rho_k^{(1)}\right)(\lambda) - \sum_k \left(a_{n,k} * v_k^{(2)} \rho_k^{(2)}\right)(\lambda) \tag{3.98}$$

$$\rho_{t,n}^{(1)}(\lambda) v_n^{(1)}(\lambda) = \frac{1}{2\pi} \varepsilon_n'(\lambda) - \sum_k \left(a_{n,k} * v_k^{(1)} \rho_k^{(1)}\right)(\lambda) + \sum_k \left(b_{n,k} * v_k^{(2)} \rho_k^{(2)}\right)(\lambda) \, . \tag{3.99}$$

Before discussing the predictions of (3.96) for the entaglement dynamics we briefly sketch the derivation of Equations (3.98) – (3.99).

3.4.1 Velocities of the Excitations

Similarly to the XXZ model (cf. Section 1.2.4), elementary excitations over the stationary state $\{\bar{\rho}_n^{(r)}(\lambda)\}$ are constructed by considering a microscopic representation of the stationary state, described by a configuration of integers $\{I_\alpha^n, J_\beta^m\}$ (*cf.* (3.23)), and adding or removing one integer. The operation of adding such an integer to those in the sector labelled by n and r, which we call *excitation of string type n and species r*, can be interpreted as the addition of a quasi-particle with rapidity λ, energy $\varepsilon_n^{d\,(r)}(\lambda)$ and momentum $p_n^{d\,(r)}(\lambda)$. The quantities $\varepsilon_n^{d\,(r)}(\lambda)$ and $p_n^{d\,(r)}(\lambda)$ are called dressed energy and momentum. They have a very simple physical interpretation – adding a new quasi-particle to the system has a feedback on all the others because of the interaction, so its effective dispersion relation changes.

Given the dispersion relation of an excitation, *i.e.* its dressed energy and momentum, we can find its group velocity from the formula

$$v_n^{(r)}(\lambda) \equiv \frac{\mathrm{d}\varepsilon_n^{d\,(r)}(\lambda)}{\mathrm{d}p_n^{d\,(r)}(\lambda)} = \frac{\varepsilon_n^{d\,(r)\prime}(\lambda)}{p_n^{d\,(r)\prime}(\lambda)} \, . \tag{3.100}$$

By a calculation analogous to that of the XXZ model [30], we find that

$$p_n^{d\,(r)\prime}(\lambda) = 2\pi \rho_{t,n}^{(r)}(\lambda) \, , \tag{3.101}$$

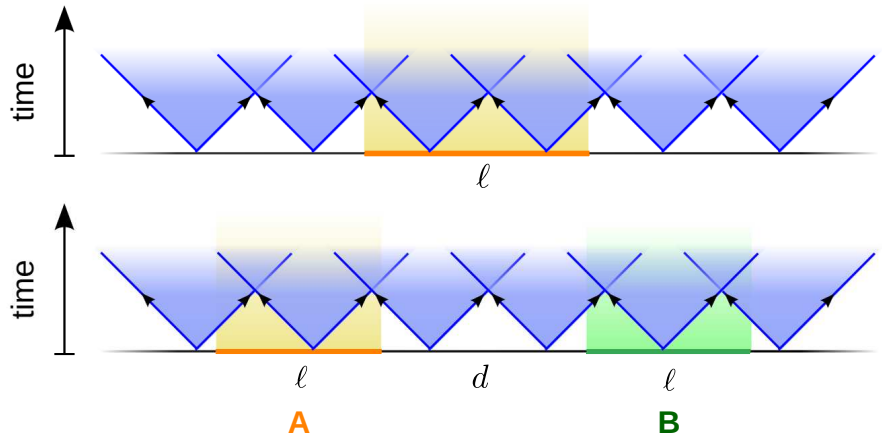

Figure 3.4: Pictorial representation of the quasi-particle interpretation of the entanglement dynamics in two different configurations. Blue solid lines represent pairs of quasi-particles moving at the maximal velocity, while slower pairs of quasi-particles are represented by a light blue halo. The top panel depicts the evolution of entanglement entropy between a subsystem of length ℓ and the rest of the infinite system, detailed in Sec. 3.4.2. The entanglement entropy is computed by counting all the pairs of quasi-particles with one quasi-particle in the subsystem and the other in the rest. The bottom panel shows the configuration considered in Sec. 3.4.3. Here we deal with two subsystems A and B of length ℓ separated by a distance d, and compute the mutual information $I_{A:B}(t)$ by counting all the pairs of quasi-particles with one quasi-particle in A and the other in B. (Figure taken from [88].)

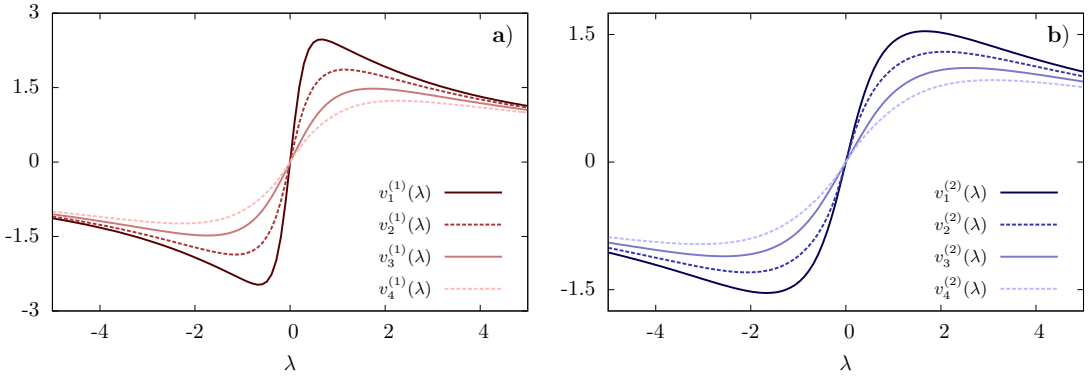

Figure 3.5: Velocities of the elementary excitations over the stationary state $\{\bar{\rho}_n^{(r)}(\lambda)\}$ (*cf.* Eq. (3.54)). Left and right panels show the velocities of elementary excitations of string type $n = 1, 2, 3, 4$, respectively of the first and second species ($r = 1, 2$). (Figure taken from [88].)

and that $\{\varepsilon_n^{d\,(r)\prime}(\lambda)\}_{r=1,2}$ fulfil the following system of integral equations

$$\varepsilon_n^{d\,(2)\prime}(\lambda) = \sum_k \left(b_{n,k} * \varepsilon_k^{d\,(1)\prime}\right)(\lambda) - \sum_k \left(a_{n,k} * \varepsilon_k^{d\,(2)\prime}\right)(\lambda)\,, \tag{3.102}$$

$$\varepsilon_n^{d\,(1)\prime}(\lambda) = \varepsilon_n'(\lambda) - \sum_k \left(a_{n,k} * \varepsilon_k^{d\,(1)\prime}\right)(\lambda) + \sum_k \left(b_{n,k} * \varepsilon_k^{d\,(2)\prime}\right)(\lambda)\,. \tag{3.103}$$

Substituting the definition (3.100) readily gives the system (3.98) – (3.99).

For the the purpose of the numerical solution, it is convenient to follow a standard TBA method [21] to write the system (3.98) – (3.99) in a partially decoupled form

$$\rho_{t,n}^{(1)}(\lambda) v_n^{(1)} = -s'\delta_{n,1} + s * \left(\rho_{h,n-1}^{(1)} v_{n-1}^{(1)} + \rho_{h,n+1}^{(1)} v_{n+1}^{(1)}\right) + s * \rho_n^{(2)} v_n^{(2)}\,, \tag{3.104}$$

$$\rho_{t,n}^{(2)}(\lambda) v_n^{(2)} = s * \left(\rho_{h,n-1}^{(2)} v_{n-1}^{(2)} + \rho_{h,n+1}^{(2)} v_{n+1}^{(2)}\right) + s * \rho_n^{(1)} v_n^{(1)}\,. \tag{3.105}$$

These integral equations can be readily solved numerically. In Fig. 3.5 we report the velocities of the two species of elementary excitations with the first four string types, constructed over the stationary state $\{\bar{\rho}_n^{(r)}(\lambda)\}$ (*cf.* Eq. (3.54)). From the plot we see that the velocities are odd functions of λ with a minimum and a maximum reached for finite values of λ. The maximal velocity for the propagation of information is given by that of excitations of the first species and string type 1, $v_{\max} = \max_\lambda v_1^{(1)}(\lambda)$. The maximal velocity for excitations of the second species is given by $v_{\max}^{(2)} = \max_\lambda v_1^{(2)}(\lambda)$ with $v_{\max}^{(2)} \approx 0.5\, v_{\max}$.

3.4.2 Entanglement Dynamics

Let us now consider the entanglement dynamics predicted by Eq. (3.96). In Fig. 3.6a, we report the time evolution of the entanglement entropy after a quench from the

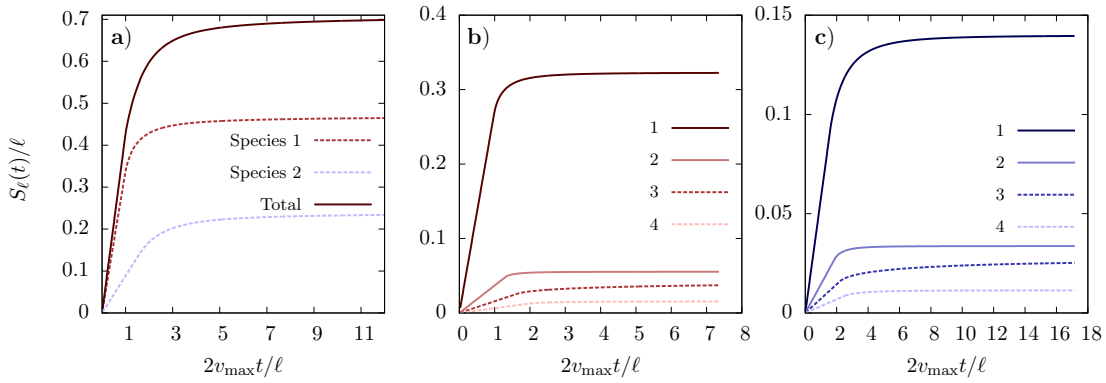

Figure 3.6: Entanglement evolution after a quench from the initial state (3.55). The left panel shows the time evolution of the entanglement entropy as a function of $2v_{\max}t/\ell$ (magenta solid line), it also shows the separate contributions carried by quasi-particles of the first (red dashed line) and second species (blue dashed line). The central and right panels show the string-type resolved ($n = 1, 2, 3, 4$) contributions to the entanglement dynamics, respectively for the first and the second species of excitations. (Figure taken from [88].)

initial state (3.55). As is customary, we plot $S_\ell(t)/\ell$ as a function of the scaling variable $2v_{\max}t/\ell$. The plot clearly shows the standard spreading of entanglement entropy [172]: there is a linear increase of the entanglement entropy for $t < \ell/2v_{\max}$ governed by the fastest quasi-particles, followed by a slow saturation dictated by all the other slower quasi-particles. For the initial state considered, the largest contribution to the entanglement is coming from the fastest quasi-particles: those of species $r = 1$ and string type $n = 1$ (*cf.* Fig. 3.2). This observation is confirmed by the species resolved lines in Fig. 3.6a, which show that the particles of the first species bring almost twice as much entanglement as those of the second species. A further confirmation comes from the string-type resolved plots in Figs 3.6b and 3.6c, which demonstrate that the contribution of bound states is strongly suppressed. A final observation is that the asymptotic value of the entanglement entropy is approximately 0.7 which is smaller than $\log 3 \approx 1.1$, the maximal density of entropy per site in the spin-1 chain (indeed $\log 3$ corresponds to the density of thermodynamic entropy in the infinite temperature state).

3.4.3 Mutual Information

The entanglement entropy is not the ideal quantity to highlight the contribution of all the different quasi-particles: the contribution of the quasi-particles bringing more entanglement covers all the others. The contribution of different quasi-particles can be resolved more effectively considering two disjoint intervals. Let us take two spin blocks A and B of length ℓ, separated by a distance d, as depicted in Fig. 3.4, and

focus on the *mutual information*

$$I_{A:B} = S_A + S_B - S_{A\cup B} \tag{3.106}$$

between the two subsystems A and B. The mutual information after a quench is also believed to signal the non-integrability and chaotic behavior of a system via the breakdown of the quasi-particle picture [195–198].

In the quasi-particle picture, the mutual information counts all the pairs of quasi-particles with one quasi-particle in A and the other in B, as pictorially shown in Fig. 3.4. Its time evolution is then simply written down generalizing the result of [141] to two species of excitations

$$\begin{aligned} I_{A:B}(t) = &\sum_{r=1,2}\sum_{n=1}^{\infty}\int \mathrm{d}\lambda \left[\left(2|v_n^{(r)}(\lambda)|t-d\right)\chi_{[d,d+\ell]}(2|v_n^{(r)}(\lambda)|t)\right] s_n^{(r)}(\lambda) \\ &+\sum_{r=1,2}\sum_{n=1}^{\infty}\int \mathrm{d}\lambda \left[\left(d+2\ell-2|v_n^{(r)}(\lambda)|t\right)\chi_{[d+\ell,d+2\ell]}(2|v_n^{(r)}(\lambda)|t)\right] s_n^{(r)}(\lambda), \end{aligned} \tag{3.107}$$

where $\chi_{[a,b]}(x)$ is the characteristic function of $[a,b]$, *i.e.* it is equal to 1 if $x\in[a,b]$ and equal to 0 otherwise.

The time evolution of the mutual information is reported in Fig. 3.7, where we plot $I_{A:B}(t)/\ell$ as a function of $2v_{\max}t/\ell$ for three different values of the ratio d/ℓ. We see that the contributions of different quasi-particles are easily detected as they give rise to peaks in $I_{A:B}(t)$ – the peak due to the quasi-particles of species r and string type n is appearing at approximately

$$t_n^{(r)} = \frac{d+\ell}{2v_{\max,n}^{(r)}} = \frac{v_{\max}}{v_{\max,n}^{(r)}} t_1^{(1)}\,, \tag{3.108}$$

where we introduced $v_{\max,n}^{(r)} = \max_\lambda v_n^{(r)}(\lambda)$. Once again, the most prominent peak corresponds to the fastest quasi-particles, as they carry the largest amount of correlations. As shown in Figs. 3.7a– 3.7c, increasing the ratio d/ℓ we can increase $2v_{\max}t_1^{(1)}/\ell$ and separate the peaks, in this way it is easier to discern the contribution of different quasi-particles.

3.5 Discussion

In this Chapter we studied a quantum quench in a nested Bethe-ansatz solvable model, the spin-1 Lai-Sutherland chain. The thermodynamic description of the latter is in terms of two different species of quasi-particles, each one forming an infinite number of bound states. We considered a simple initial matrix product state for which the overlaps with Bethe states are known [160] and determined the corresponding post-quench steady state by means of the Quench Action approach. We tested the validity of our result by checking that the expectation value of all the local conserved charges on the initial and long-time steady state are equal. Finally,

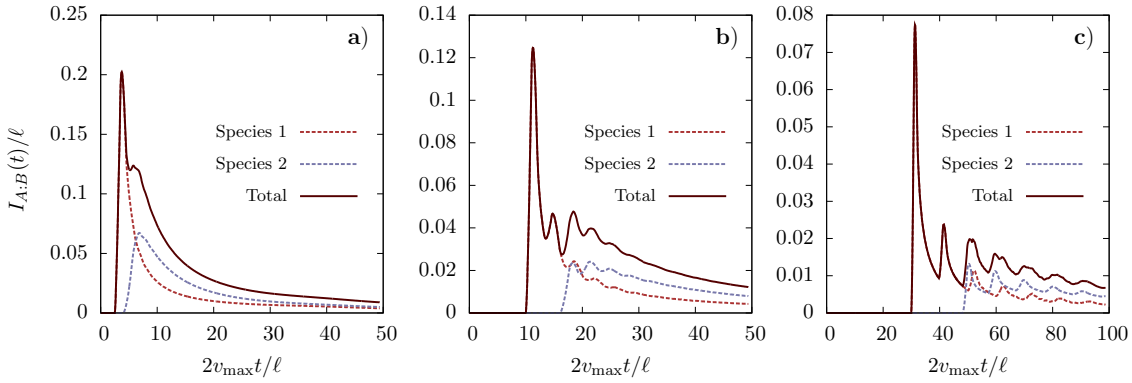

Figure 3.7: Time evolution of the mutual information starting from the initial state (3.55). The three panels correspond to increasing values of the ratio d/ℓ, respectively $2.5, 10, 30$. The plots show the total mutual information (magenta solid line) together with the separate contributions carried by quasi-particles of the first (red dashed line) and second species (blue dashed line). (Figure taken from [88].)

we investigated the post-quench entanglement dynamics using a recently proposed conjecture for interacting integrable models [141]. Importantly, due to the simple structure of our initial state, all our predictions for the entanglement dynamics can in principle be tested against efficient numerical methods such as tDMRG or iTEBD, on the same lines of what done in Ref. [141].

Our work raises a number of compelling questions. From the physical point of view, it is natural to wonder how the two different species of excitations affect the dynamics of local correlations after the quench. It is clear from our results that each species carries a non-vanishing contribution on entanglement dynamics. As a consequence, it is not possible to individually probe the dynamics of the single species by computation of entanglement entropy or mutual information. An interesting question then is whether some appropriate local correlators can be found, such that their dynamics is entirely determined by one and only one of the two species. This would result in a mechanism of effective separation in the spreading of correlations after the quench.

From the technical point of view, an interesting question stems from the structure of the overlap formula of our initial state. Since the seminal works [95, 199, 200], determinant expressions of the form (3.59) have appeared in several cases in the past few years for a variety of models. It is even more surprising to encounter a formula of this kind in the nested spin chain studied in this Chapter, possibly signalling the presence of an hidden structure common to all Bethe ansatz integrable models. Characterising the states for which such a formula exists is an important open problem, with far reaching consequences, both from the purely theoretical and practical point of view.

Our work also calls for a systematic analysis of the quasi-local charges in the spin-1 Lai-Sutherland chain. This is a necessary step towards the explicit construc-

tion of the complete GGE in this model. Such a construction would in turn lead to the possibility of considering a wider set of initial states, overcoming the technical difficulty of the computation of the overlaps required by the Quench Action approach. The explicit calculations presented in this Chapter for the initial state (3.55), provide a strict test for any future construction of the complete GGE.

Finally, it would be highly desirable to find explicit formulae for calculating expectation values of local operators on the stationary state in the spin-1 Lai Sutherland chain. Such formulae are currently known only for few non-nested Bethe ansatz integrable models, namely the Lieb-Liniger model [201, 202], the XXZ spin-1/2 chain [74, 75], and the sinh-Gordon field theory [203, 204]. A promising route is to first consider expectation values at finite temperature and then generalize them to arbitrary excited eigenstates. This approach has been found fruitful in the case of the XXZ spin-1/2 chain and of the sinh-Gordon field theory.

3.A Appendix: Algebraic Bethe ansatz

In this section we briefly sketch the algebraic Bethe ansatz analysis of the Hamiltonian (3.1), which also allows for a systematic derivation of higher local conservation laws.

The fundamental object of the algebraic Bethe ansatz is the so called R-matrix, which in our case reads

$$R_{12}(\lambda) = \frac{\lambda}{\lambda + i} + \frac{i}{\lambda + i}\mathcal{P}_{12}, \tag{3.109}$$

where $\mathcal{P}_{12}$ is the permutation matrix exchanging the local spaces h_1, h_2. The R-matrix (3.109) is invariant under $SU(3)$ and it is a simple exercise to show that it satisfies

$$R_{12}(0) = \mathcal{P}_{12} \tag{3.110}$$

$$R_{12}(u)R_{21}(-u) = \mathrm{id}\,, \tag{3.111}$$

where id is the identity operator on $h_1 \otimes h_2$. Next, introducing the Lax operator

$$L_{0j}(\lambda) = R_{0j}(\lambda)\,, \tag{3.112}$$

one can define the family of transfer matrices

$$\tau(\lambda) = \mathrm{tr}\left\{L_{0N}(\lambda)\dots L_{01}(\lambda)\right\}\,, \tag{3.113}$$

which depend on the spectral parameter λ. Crucially, different transfer matrices commute

$$[\tau(\mu), \tau(\lambda)] = 0\,, \tag{3.114}$$

and as a consequence one can define a sequence of commuting operators as

$$Q_{n+1} = i\frac{\partial^n}{\partial\lambda^n}\ln\tau(\lambda)\Big|_{\lambda=0}\,, \qquad\qquad n = 1, \dots, \infty\,. \tag{3.115}$$

These are usually called charges and can be written down explicitly by exploiting the properties of the R-matrix, as nicely explained in [205]. However, the actual expression becomes increasingly unwieldy for many practical purposes as n increases.

The importance of this algebraic construction lies in the fact that the first charge is equal to the Hamiltonian (3.1), namely

$$Q_2 = H\,. \tag{3.116}$$

Hence, the transfer matrix (3.113) can be thought of as the generator of the local conservation laws of the model.

As we have mentioned in Section 3.1.1, the knowledge of the rapidities corresponding to a given eigenstate also allows for a direct calculation of expectation values of local charges. Indeed, the analytic expression of the eigenvalue of the transfer matrix (3.113) on a Bethe state with rapidities $\{k_j\}$, $\{\lambda_j\}$ is known [149], and one can explicitly write

$$\tau(\lambda)\,|\{k_j\},\{\lambda_j\}\rangle = \nu(\{k_j\},\{\lambda_j\},\lambda)\,|\{k_j\},\{\lambda_j\}\rangle\ , \tag{3.117}$$

where

$$\begin{aligned}\nu\left(\{k_j\},\{\lambda_j\},\lambda\right) = [a(\lambda)]^L \prod_{j=1}^{N} \frac{1}{a(\lambda-k_j+i/2)}\nu_1\left(\{k_j\},\{\lambda_j\},\lambda\right)\\ + \prod_{j=1}^{N}\frac{1}{a(k_j-i/2-\lambda)}\,,\end{aligned} \tag{3.118}$$

and

$$\nu_1(\{k_j\},\{\lambda_j\},\lambda) = \prod_{j=1}^{N} a(\lambda-k_j+i/2)\prod_{r=1}^{M}\frac{1}{a(\lambda-\lambda_r+i/2)} \tag{3.119}$$

$$+\prod_{r=1}^{M}\frac{1}{a(\lambda_r-i/2-\lambda)}\,, \tag{3.120}$$

with

$$a(\lambda) = \frac{\lambda}{\lambda+i}\,. \tag{3.121}$$

Then, it is straightforward to compute the action of a charge Q_n on the state $|\{k_j\},\{\lambda_j\}\rangle$: from the definition (3.115), the calculation is reduced to taking derivatives of the expression (3.118). This calculation is completely analogous to the corresponding one in the spin-1/2 XXX chain and reads as

$$\langle\{k_j\},\{\lambda_j\}|Q_m|\{k_j\},\{\lambda_j\}\rangle = \sum_{j=1}^{N}(-1)^m i\frac{\partial^m}{\partial\lambda^m}\log\left[\frac{\lambda+i/2}{\lambda-i/2}\right]\Bigg|_{\lambda=k_j}\,. \tag{3.122}$$

In particular, note that one can neglect the first term in (3.118) since

$$\frac{\partial^m}{\partial\mu^m}\left[a(\mu)\right]^L\Big|_{\mu=0} = 0\,, \qquad\qquad m<L\,. \tag{3.123}$$

It is also possible to take the thermodynamic limit and evaluate the expectation value of conserved charges on Bethe states corresponding to the distributions $\rho_n^{(r)}(\lambda)$, with $r = 1, 2$. Starting from the expression at finite size, making use of the string hypothesis and taking the thermodynamic limit, one finally obtains

$$\lim_{L\to\infty} \frac{1}{L} \langle \{\rho_n^{(r)}\} | Q_m | \{\rho_n^{(r)}\} \rangle = \sum_{n=1}^{\infty} \int_{-\infty}^{+\infty} \mathrm{d}\lambda \left(\rho_n^{(1)}(\lambda) c_{m,n}^{(1)}(\lambda) + \rho_n^{(2)}(\lambda) c_{m,n}^{(2)}(\lambda) \right) , \tag{3.124}$$

where

$$c_{m+1,n}^{(1)}(\lambda) = (-1)^m i \frac{\partial^m}{\partial \lambda^m} \log \left[\frac{\lambda + in/2}{\lambda - in/2} \right] , \qquad m \geq 1 \tag{3.125}$$

$$c_{m+1,n}^{(2)}(\lambda) \equiv 0 , \qquad m \geq 1 , \tag{3.126}$$

while we indicated with $|\{\rho_n^{(r)}\}\rangle$ a Bethe state which corresponds to the rapidity distributions $\{\rho_n^{(r)}\}$ in the thermodynamic limit. Remarkably, we see from (3.122) and (3.126) that the second species of quasi-particles does not contribute to any of the higher local conserved charges.

3.B Appendix: Higher local conserved charges

In this appendix we discuss the computation of the initial-state expectation values of local conserved charges. More specifically, we detail the derivation of formula (3.85) for the corresponding generating function.

As we anticipated in the main text, we exploit the method used in [54] for the case of the XXZ spin-1/2 chain. The starting point of our derivation is provided by the formal expansion of the transfer matrix (3.113) in terms of the local charges (3.115), namely

$$\tau(\lambda) = U \exp \left(-i \sum_{k=1}^{\infty} Q_{k+1} \frac{\lambda^k}{k!} \right) , \tag{3.127}$$

where U is the one site shift operator, defined as

$$U | e_{i_1} \dots e_{i_L} \rangle = | e_{i_2} e_{i_3} \dots e_{i_L} e_{i_1} \rangle . \tag{3.128}$$

Since the operators Q_k are self-adjoint, Eq. (3.127) suggests that for large L one can write

$$\tau^{-1}(\lambda) = \tau^{\dagger}(\lambda) , \tag{3.129}$$

in the sense that the power series expansions in λ of the two sides of (3.129) coincide for $\lambda \in \mathbb{R}$. Here we used that $U^{-1} = U^{\dagger}$. Next, from (3.84) we observe that the generating function $\Omega_{\Psi_0}(\lambda)$ can be defined as

$$\begin{aligned} -i\Omega_{\Psi_0}(\lambda) &\equiv \lim_{L\to\infty} \frac{1}{L} \langle \Psi_0 | \frac{\partial}{\partial \mu} \log(\tau(\mu)) | \Psi_0 \rangle \Big|_{\mu=\lambda} \\ &= \lim_{L\to\infty} \frac{1}{L} \langle \Psi_0 | \tau^{-1}(\lambda) \frac{\partial}{\partial \mu} \tau(\mu) | \Psi_0 \rangle \Big|_{\mu=\lambda} . \end{aligned} \tag{3.130}$$

Using (3.129) we then obtain

$$\Omega_{\Psi_0}(\lambda) = i \lim_{L\to\infty} \frac{1}{L} \langle \Psi_0 | \tau^\dagger(\lambda) \frac{\partial}{\partial \mu} \tau(\mu) | \Psi_0 \rangle \Big|_{\mu=\lambda} . \tag{3.131}$$

The computation is then reduced to evaluating the expectation value of the product of two transfer matrices. This can be performed analytically, due to the simple structure of our initial state and exploiting the representation of transfer matrix (3.113) as a matrix product operator. In fact, the steps involved for the explicit evaluation of the r.h.s. of (3.131) are completely analogous to those explained in [53] for the case of the spin-1/2 chain and will not be reported here. Note in particular that the derivative in (3.131) can be efficiently performed by means of the Jacobi formula [53], which makes it possible to reach a closed form analytical result. The intermediate analytical calculations can be easily carried out with the program Mathematica, so that one finally derives Eq. (3.85).

Chapter 4

Molecular dynamics simulation of entanglement evolution in generalized hydrodynamics

In this Chapter we develop a numerical method that allows us to compute the predictions of the quasiparticle picture [172] for entanglement dynamics in inhomogeneous systems. We focus on the out-of-equilibrium dynamics of the von Neumann entanglement entropy, which is defined as [168–171]

$$S = -\mathrm{Tr}\rho_A \ln \rho_A, \tag{4.1}$$

with $\rho_A = \mathrm{Tr}_A \rho$ the reduced density matrix of a macroscopic subsystem A (see Fig. 4.1 (a) for a one-dimensional setup). In the quasiparticle picture, pairs of entangled quasiparticles are produced after the quench. As these pairs propagate ballistically, they entangle larger regions of the system (see Fig. 4.1 (a)). At a given time after the quench, the von Neumann entropy is the sum of the individual contributions coming from each pair that is shared between A and its complement. This picture has been explicitly verified in free-fermion models [176]. It has been shown recently that it holds true also in the presence of interactions [141].

The quasiparticle prediction for the entanglement entropy of subsystem A of length ℓ after a quench in generic integrable systems reads as [141]

$$S(t) = \sum_n \Big[2t \int\limits_{2|v_n(\lambda)|t<\ell} d\lambda |v_n(\lambda)| s_n(\lambda) + \ell \int\limits_{2|v_n(\lambda)|t>\ell} d\lambda s_n(\lambda) \Big]. \tag{4.2}$$

Here the index n labels the different types of quasiparticles present in the model. The velocities $v_n(\lambda)$ are the dressed velocities of quasiparticles in the post-quench relaxed state described by the GGE saddle point, and $s_n(\lambda)$ is the contribution of the mode λ of quasiparticle type n to the Yang–Yang entropy (1.34) of the GGE saddle point,

$$s_n(\lambda) = \rho_{\mathrm{t},n}(\lambda) \ln(\rho_{\mathrm{t},n}(\lambda)) - \rho_n(\lambda) \ln \rho_n(\lambda) - \rho_{n,\mathrm{h}}(\lambda) \ln \rho_{n,\mathrm{h}}(\lambda). \tag{4.3}$$

One of the interesting questions regarding the quasiparticle picture is whether it is possible to generalize it to inhomogeneous settings. In the standard bipartite setup (see Fig. 4.1 (b)) two homogeneous chains in a different state (L, R in Fig. 4.1) are joined together at $t = 0$. One then studies the ensuing dynamics under an integrable globally homogeneous Hamiltonian. For typical initial states, in the limit of long times and large distances x from the origin, the system is descried by the Generalized Hydrodynamics approach. By combining the quasiparticle picture with the GHD approach [142, 206–208] it is possible, in principle, to generalize the quasiparticle picture [141] to inhomogeneous settings. However, actually calculating the full-time entanglement dynamics in this case is a demanding task. The main difficulty is that, unlike in homogeneous quenches, the trajectories of the quasiparticles are not straight lines. Explicit results are available only in the short time limit $t/\ell \to 0$ and the long time limit $t/\ell \to \infty$ [208].

In order to overcome the above difficulties, we use a mapping between the GHD and the "molecular dynamics" of a system of classical particles called flea gas [105]. This mapping allows one to obtain the out-of-equilibrium dynamics in quantum integrable systems by performing classical simulations [111, 112, 118]. So far, the flea gas method has been employed only to integrable field theories, such as the Lieb-Liniger gas, but not to lattice models. In this Chapter, we discuss a generalization of the flea gas approach to the spin-1/2 anisotropic XXZ chain. An important remark is that, unlike for the Lieb-Liniger model [105], for the XXZ chain it is not straightforward to show analytically that the flea gas dynamics is fully equivalent to the GHD. However, we present robust numerical evidence that this is the case, at least in the quenches that we consider.

4.1 Quench protocol

In this Chapter we consider quenches of the gapped XXZ model (1.46) with $\Delta > 1$. We construct our initial states by joining two homogeneous blocks that are prepared in either the translationally invariant tilted Néel state or in the translationally invariant Majumdar-Ghosh (dimer) state. The method is applicable, in principle, to any low-entangled initial state.

The translationally invariant tilted Néel state is denoted as $|\mathrm{N}, \theta\rangle$, and it is obtained by rotating the Néel state $|\uparrow\downarrow\uparrow\dots\rangle$ around the $\hat{z}$ axis and making it translationally invariant, i.e.,

$$|\mathrm{N}, \theta\rangle = \left(\frac{1+\mathcal{T}}{\sqrt{2}}\right) \Big\{ [\cos(\theta/2)\,|\uparrow\rangle + i\sin(\theta/2)\,|\downarrow\rangle] \otimes \\ \otimes\, [\sin(\theta/2)\,|\uparrow\rangle - i\cos(\theta/2)\,|\downarrow\rangle] \Big\}^{\otimes L/2} . \tag{4.4}$$

Here θ is the tilting angle and $\mathcal{T}$ is the one site translation operator to the right. The Néel state is recovered for $\theta = 0$. Similarly, the translationally invariant dimer

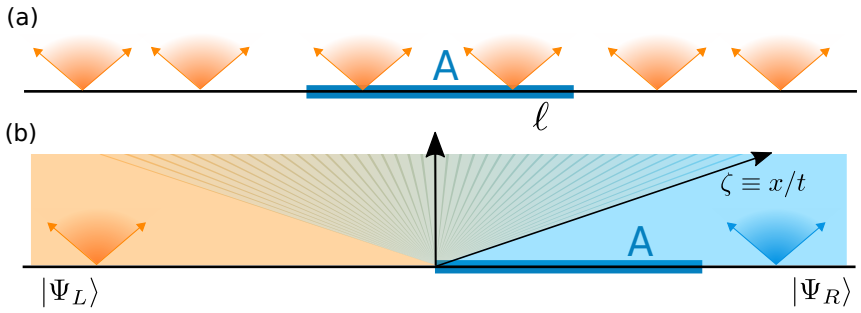

Figure 4.1: Dynamics of the entanglement entropy after a quench from a homogeneous (in (a)) and a piecewise homogeneous initial condition (in (b)). In both cases the entanglement dynamics is due to the ballistic propagation of pairs of entangled particles (shaded cones). In (a) the quasiparticles entanglement entropy is the thermodynamic entropy of the GGE that describes the steady state. In (b) the inhomogeneous initial state is obtained by joining two homogeneous systems (left and right) in the states $|\Psi_L\rangle$ and $|\Psi_R\rangle$. Entangled pairs are produced in the bulk of the two chains. A light-cone spreads from the interface between them. For each value of $\zeta \equiv x/t$ the system relaxes locally to a GGE. The entanglement entropy is obtained propagating the entropy of the GGEs describing the bulk of the left and right chains, i.e., for $\zeta \to \pm\infty$. (Figure taken from [209].)

state $|\mathrm{D}\rangle$ is defined as

$$|\mathrm{D}\rangle = \left(\frac{1+\mathcal{T}}{\sqrt{2}}\right)\left(\frac{|\uparrow\downarrow\rangle - |\downarrow\uparrow\rangle}{\sqrt{2}}\right)^{\otimes L/2}. \tag{4.5}$$

In the homogeneous setup (Fig. 4.1 (a)), the chain is prepared in one of the states (4.4) or (4.5) at $t = 0$, and the system is let to evolve under (1.46). In the inhomogeneous case (Fig. 4.1 (b)) we consider quenches from the initial state $|\Psi_0\rangle = |\mathrm{N}, \theta\rangle \otimes |\mathrm{D}\rangle$.

For the homogeneous quenches from the above states, the post-quench saddle-point state is exactly known. All the information about the relaxed is contained in $\eta_1(\lambda)$ of the GGE saddle-point (1.71). For the tilted Néel state $|\mathrm{N}, \theta\rangle$, one has [62]

$$1 + \eta_1(\lambda) = \frac{T_1(\lambda + i\frac{\eta}{2})}{\phi(\lambda + i\frac{\eta}{2})}\frac{T_1(\lambda - i\frac{\eta}{2})}{\bar{\phi}(\lambda - i\frac{\eta}{2})}, \tag{4.6}$$

where

$$\begin{aligned} T_1(\lambda) \quad &= -\tfrac{1}{8}\cot(\lambda)\{8\cosh(\eta)\sin^2(\theta)\sin^2(\lambda) - 4\cosh(2\eta) && (4.7)\\ &\quad +[\cos(2\theta)+3][2\cos(2\lambda)-1] + 2\sin^2(\theta)\cos(4\lambda)\}, && (4.8)\end{aligned}$$

and

$$\begin{aligned} \phi(\lambda) \quad &= \tfrac{1}{8}\sin(2\lambda + i\eta)[2\sin^2(\theta)\cos(2\lambda - i\eta) + \cos(2\eta) + 3], && (4.9)\\ \bar{\phi}(\lambda) \quad &= \tfrac{1}{8}\sin(2\lambda - i\eta)[2\sin^2(\theta)\cos(2\lambda + i\eta) + \cos(2\eta) + 3]. && (4.10)\end{aligned}$$

For the dimer state, the function $\eta_1(\lambda)$ reads [85]

$$\eta_{1,\lambda} = \frac{\cos(4\lambda) - \cosh(2\eta)}{\cos^2(\lambda)(\cos(2\lambda) - \cosh(2\eta))} - 1. \tag{4.11}$$

Once $\eta_1(\lambda)$ is known, one can use the Y-system [85] and the BGT equations (1.30) to reconstruct the root densities $\rho_n(\lambda)$ describing the homogeneous relaxed state.

4.2 Flea gas approach for out-of-equilibrium integrable systems

The flea gas approach was introduced in Ref. [113] as an effective numerical method to simulate the GHD by employing classical "molecular dynamics" techniques. The method allows to simulate the dynamics of a quantum system starting from any thermodynamic macrostate, both homogeneous as well as inhomogeneous. So far, the approach has been implemented for the Lieb-Liniger gas but not for lattice systems such as the XXZ model.

The method was inspired by the correspondence between the continuity equation (1.84) and the hydrodynamic equations of a system of classical particles (hard-rod gas). Hard rods are classical one-dimensional objects undergoing elastic scattering. Here we denote their length as d. The hard rods dynamics is as follows. Hard rods move like free particles with bare velocity v^{bare}. When the distance between the centers of two hard rods equals d, they exchange their velocities. Following Ref. [113], here we adopt an alternative interpretation. One can think of hard rods as point-like objects. The scattering is then implemented as follows. When two hard rods are at the same point in space they scatter. The scattering consists of an instantaneous displacement by length d of the positions of the two particles. Precisely, after assuming $d > 0$ we impose that the particle on the left (right) is shifted by d to the right (left).

Let us define the density of rods with "bare" velocity v^{bare} as $\rho(v^{\text{bare}})$. During time evolution, many scatterings occur. The net effect is a renormalization of the velocity of the hard rods. Let us define this space-time dependent renormalized or "dressed" velocity as $v_{x,t}(v^{\text{bare}})$ The dressed velocity is a function of the bare velocity v_{b}. The density $\rho(v^{\text{b}})$ obeys the continuity equation [210]

$$\partial_t \rho_{x,t}(v^{\text{bare}}) + \partial_x(v_{x,t}(v^{\text{bare}})\rho_{x,t}(v^{\text{bare}})) = 0. \tag{4.12}$$

The renormalized velocity is given by the integral equation [210]

$$v_{x,t}(v^{\text{bare}}) = v^{\text{bare}} + d\int dw \rho_{x,t}(w)(v_{x,t}(v^{\text{bare}}) - v_{x,t}(w)). \tag{4.13}$$

Equation (4.13) has the same structure as (1.64), and it admits a simple interpretation. The expression $\rho(v(v^{\text{bare}}) - v(w))$ is the number of scatterings per unit time between the hard rod with velocity v and the ones with velocity w. The second term on the right hand side in (4.13) is the total shift that happens in the unit time to the trajectory of the hard rod with bare velocity v due to the scatterings with other hard rods.

4.2.1 Flea gas for the XXZ chain and numerical implementation

We now discuss the application of the flea gas method for the XXZ chain. Before describing the method for the quenches from an inhomogeneous initial state, it is useful to consider the case of homogeneous ones. The TBA densities $\rho_n(\lambda)$ describing the steady state after the quench are stationary and homogeneous, i.e., they do not depend on x, t. The group velocity $v_n(\lambda)$ of the quasiparticles are obtained by solving system (1.64). The crucial observation is that Eq. (1.64) has the same structure as the equation for the hard rod gas (4.13). Equation (1.64) can be interpreted as the dressing equation for the velocities of a system of multi-species and point-like classical particles undergoing elastic scattering. Now each particle is identified by a double index (n, λ), and $A_{n,m}(\lambda - \mu)/a_n(\lambda)$ is interpreted as a scattering length. Thus, we define $d_{n,m}(\lambda, \mu)$ as

$$d_{n,m}(\lambda, \mu) = \frac{A_{n,m}(\lambda - \mu)}{a_n(\lambda)}. \tag{4.14}$$

Similarly to the hard rods, the particles move freely with bare velocities v^{bare} (given by the definition after (1.62)). Scatterings occur when two particles are at the same point in space. If the particle coming from the left has labels (n, ν), and the particle coming from the right has labels (m, μ), then the particle coming from the left will jump $d_{n,m}(\lambda, \mu)$, and the particle coming from the right will jump $-d_{m,n}(\mu, \lambda)$.

A crucial remark is in order. Unlike the case of the Lieb-Liniger model [105] it is not straightforward to show that the dynamics outlined above reproduces the correct dressing for the bare velocities of the particles, i.e., Eq. (1.64). First, the displacement of the trajectory of a given particle is given as $\Delta x = v_n(\lambda)\Delta t$, which defines the dressed velocity $v_n(\lambda)$. The dressing of the velocity arises from the scattering with the other particles. The number of scatterings per unit time between a particle with label (n, λ) and particles with label (m, μ) is given as $\rho_m(\mu)|v_n(\lambda) - v_m(\mu)|\Delta t$. The key issue is how to determine the direction of the jump. During the flea gas dynamics the particles move with their bare velocities. If a particle moving at $v_n^{\text{bare}}(\lambda)$ scatters with another one with velocity $v_m^{\text{bare}}(\mu)$ its trajectory gets shifted by $\text{sign}(v_n^{\text{bare}}(\lambda) - v_m^{\text{bare}}(\mu))d_{n,m}(\lambda, \mu)$. For the Lieb-Liniger gas one can show that the dressed velocities are monotonic functions of the bare ones, which implies that $\text{sign}(v_n^{\text{bare}}(\lambda) - v_m^{\text{bare}}(\mu)) = \text{sign}(v_n(\lambda) - v_m(\mu))$. This ensures that the jumped length is $\text{sign}(v_n(\lambda) - v_m(\lambda))d_{n,m}(\lambda, \mu)$. By summing over m and integrating over μ, one obtains the term on the right-hand-side in (1.64). This shows that the flea gas dynamics gives the correct dressing for the group velocities of the particles. On the other hand, for the XXZ chain the dressed velocities are not monotonically increasing functions of the bare ones. An important consequence is that now $\text{sign}(v_{n,\lambda}^{\text{bare}} - v_{m,\mu}^{\text{bare}}) \neq \text{sign}(v_n(\lambda) - v_m(\mu))$. This implies that for the XXZ chain one cannot conclude that the total jumped length is given as $(v_n(\lambda) - v_m(\mu))d_{n,m}(\lambda, \mu)$. To overcome this problem, our strategy here is to use the flea gas dynamics as outlined above, showing numerically that, at least in the quenches that we consider, it gives the correct dressing for the group velocities of the particles (see section 4.3.1).

We now discuss the details of the implementation of the flea gas method for the XXZ chain. The system is in the continuum, and it is of length L. Both space and time are treated as continuous variables. For a homogeneous quench, the initial state of the simulation is prepared as follows. First, we create a total number of particles N_p. The particles are described by the TBA densities $\rho_n(\lambda)$, which contain the full information about the post-quench GGE (see section 4.1 for the results regarding the quenches considered here). N_p is chosen such that one has the correct value of the particle density, i.e.,

$$N_p = L \sum_n \int d\lambda \rho_n(\lambda), \tag{4.15}$$

Note that N_p is not the total number of down spins N, which is given as $N = L \sum_n \int d\lambda n \rho_n(\lambda)$. This simply reflects that in the simulation multi-spin bound states are treated as individual point-like particles. The particles are labeled as $1, \ldots, N_p$. Here we restrict ourselves to the situation in which only pairs of entangled quasiparticles with opposite rapidities [141] are present. For convenience, particles forming an entangled pair are labelled by consecutive integers as $(2\gamma, 2\gamma{+}1)$ with $\gamma = 1, \ldots, N_p/2$. To each pair we assign a species label n with probability r_n given as

$$r_n = \frac{L}{N_{\rm p}} \int d\lambda \rho_n(\lambda). \tag{4.16}$$

Similarly, rapidities $\lambda_{2\gamma} = -\lambda_{2\gamma+1}$ are assigned to the pairs with probability proportional to $\rho_n(\lambda) = \rho_n(-\lambda)$. The position of each pair is uniformly random in the interval $[-L/2, L/2]$. Note that entangled particles are produced at the same point in space, implying $x_{2\gamma} = x_{2\gamma+1}$. However, to avoid spurious scatterings when the dynamics starts, we impose a tiny displacement between entangled particles. Finally, we assign to each pair their contribution to the Yang-Yang entropy, which is $s_n(\lambda)/\rho_n(\lambda)$ (cf. (4.3)).

During the time evolution, the particles move with the bare velocities $v_n^{\rm bare}(\lambda)$, given as

$$v_n^{\rm bare}(\lambda) = \frac{\sinh(\eta)\, a_n'(\lambda)}{2 a_n(\lambda)}. \tag{4.17}$$

Here $a_n(\lambda)$ are defined in (1.31) and $a_n'(\lambda), \equiv da_n(\lambda)/d\lambda$. During the simulation only the position of the particles are updated, whereas their labels, velocities, and entropies remain the same. Particles can collide, jumping backward and forward of distance $d_{n,m}(\lambda{-}\mu)$ (cf. (4.14)). This happens as follows. Let us denote two colliding particles as P_1 and P_2, P_1 being the left particle and P_2 the right one, respectively. Let us assume that P_1 and P_2 have labels (n, λ) and (n', λ'), respectively. Thus, P_1 jumps to the right of distance $d_{n,n'}(\lambda, \lambda')$, whereas particle P_2 jumps to the left of distance $d_{n',n}(\lambda', \lambda) = -d_{n,n'}(\lambda, \lambda')$. It is crucial to observe that while jumping, P_1 and P_2 can scatter with other particles that are within $d_{n,n'}(\lambda, \lambda')$. For example, if the trajectory of P_1, after scattering with P_2, crosses that of a third particle P_3 with label (n'', λ''), P_1 scatters with P_3, as well. This means that, in principle, there is a "cascade" of scatterings initiating when P_1 and P_2 collide.

```
1: procedure EVOLVE(t_max)
2:     t = 0
3:     while t < t_max do
4:         FIND(P_1, P_2, t_coll)
5:         ∀γ,  x_γ → x_γ + v_γ t_coll
6:         UNMARK(P_n)
7:         COLLIDE(P_1, P_2)
8:         t = t + t_coll
9:     end while
10: end procedure
```

```
11: procedure COLLIDE(P_1, P_2)
12:     if MARKED(P_1, P_2) then
13:         x_1 ↔ x_2
14:     else
15:         MARK(P_1, P_2)
16:         x_1 ↔ x_2
17:         JUMPRIGHT(P_1, d_12)
18:         JUMPLEFT(P_2, d_21)
19:     end if
20: end procedure
```

Figure 4.2: Flea gas dynamics. The main procedure EVOLVE evolves the system up to $t_{\max}$. The routine FIND$(P_1, P_2, t_{\rm coll})$ finds the particles P_1 and P_2 that scatter first at time $t_{\rm coll}$. The positions x_γ of the particles are evolved up to $t_{\rm coll}$. v_γ are the bare velocities (cf. Eq. (4.17)). Then, particles P_1 and P_2 scatter. The function UNMARK removes the mark assigned to the particles when they scatter for the first time. The scattering is implemented by COLLIDE: P_1 and P_2 are displaced by a distance $d_{12} = -d_{21}$ (cf. Eq. (4.14)). The functions JUMPLEFT and JUMPRIGHT implementing this shift are in Fig. 4.3. Before scattering the particles are marked. Marked particles cross each other. Note that while P_1 is scattering with P_2, a scattering with a third particle P_3 can occur, initiating a scattering "cascade".

The complete flea gas algorithm is illustrated in Fig. 4.2. The first step is to identify the pair of particles P_1 and P_2 that scatter first, and the corresponding scattering time $t_{\rm coll}$. This is performed by the routine FIND$(P_1, P_2, t_{\rm coll})$ in Fig. 4.2. This can be done efficiently by using standard methods in molecular dynamics simulations (see for instance Ref. [211]). Then, all the particles are evolved until $t_{\rm coll}$, when the scattering between P_1 and P_2 occurs. This is described by the procedure COLLIDE in Fig. 4.2. P_1 and P_2 are instantaneously displaced by a distance $d_{1,2}$ and $d_{2,1}$ (cf. (4.14)). The displacement of the particles is implemented with the procedures JUMPLEFT and JUMPRIGHT, which are described in Fig. 4.3. Note that the two scattering particles are marked before starting the collision (see procedure MARK). This is to prevent that, while scattering with near particles, P_1 and P_2 scatter again with each other. Marked particles, instead of scattering, cross each other. After the scattering cascade starting with their first collision happened, P_1 and P_2 are unmarked.

4.2.2 Entanglement dynamics in flea gas simulations

The entanglement entropy at a given time is computed by counting the entangled pairs (weighted with their Yang-Yang entropy) that are shared between the subsystem of interest A (cf. Fig. 4.1) and the rest, i.e., the number of pairs $(P_\gamma, P_{\gamma+1})$, such that x_γ and $x_{\gamma+1}$ are in different subsystems. The result for the entanglement

```
1: procedure JumpRight(P_1, d)
2:     while d > 0 do
3:         if |x_3 − x_1| > d then
4:             x_1 = x_1 + d
5:             d = 0
6:         else
7:             d = d − |x_3 − x_1|
8:             x_1 = x_3
9:             Collide(P_1, P_3)
10:        end if
11:    end while
12: end procedure
```

```
13: procedure JumpLeft(P_1, d)
14:     while d < 0 do
15:         if |x_1 − x_3| < |d| then
16:             x_1 = x_1 + d
17:             d = 0
18:         else
19:             d = d + |x_1 − x_3|
20:             x_1 = x_3
21:             Collide(P_3, P_1)
22:         end if
23:     end while
24: end procedure
```

Figure 4.3: Jump algorithms for the flea gas dynamics. When scattering with each other, particles P_1 and P_2 are instantaneously displaced by a distance d, which depends on the species and the rapidity of the particles, and it is extracted from the scattering matrix of the model (see Eq. (4.14)). The functions JumpRight and JumpLeft implement this displacement. In JumpRight and JumpLeft particle P_3 is the next particle on the right and on the left of P_1, respectively. If during the jump P_1 does not meet particle P_3, the position of P_1 is shifted by d. If $|x_1-x_3| < |d|$, then particle P_1 scatters with P_3. The procedure Collide is defined in Fig. 4.2.

entropy reads as

$$S(t) = \Big\langle \sum_{\text{shared pairs } (\lambda,\,-\lambda)} \frac{s_n(\lambda)}{\rho_n(\lambda)} \Big\rangle_t . \tag{4.18}$$

Here the average $\langle\rangle_t$ is over different realizations of the flea gas dynamics up to time t. The sum is over the pairs that are shared between the two subsystems. Importantly, the factor $1/\rho_n(\lambda)$ takes into account that different types (n,λ) of particles appear in the sum (4.18) with a frequency $\ell\rho_n(\lambda)$.

It is very straightforward to generalize the flea gas algorithm to the inhomogeneous, bipartite quenches defined in Section (4.1) (see also Fig. 4.1). The only change with respect to the homogeneous case lies in the preparation of the initial state. In the bipartite case, the particle pairs of the initial state have to be generated with the homogeneous saddle-point density of the left reservoir, $\rho_{n,-\infty}(\lambda)$ at $x < 0$, and with the saddle-point density of the right reservoir, $\rho_{n,\infty}(\lambda)$, at $x > 0$. Pairs at $x < 0$ are assigned the entanglement contribution $s_{n,-\infty}(\lambda)/\rho_{n,-\infty}(\lambda)$, and pairs with $x > 0$ are assigned the entanglement contribution $s_{n,\infty}(\lambda)/\rho_{n,\infty}(\lambda)$. The rest of the dynamics remains the same as in the homogeneous case.

4.3 Numerical results

We now provide numerical results showing the validity of the flea gas method to calculate the dynamics of the entanglement entropy after a generic quench in in-

tegrable systems. In section 4.3.1 we present some preliminary benchmarks of the approach. In Section 4.3.2 we discuss the bipartite inhomogeneous quench depicted in Fig. 4.1 (b). Finally, in section 4.3.3 we discuss the mutual information between two intervals.

4.3.1 Preliminary benchmarks

A crucial feature of the flea gas dynamics is that it gives rise to the correct dressing of the group velocities of the quasiparticles given by (1.64). While this can be proven for the flea gas algorithm for the Lieb-Liniger model, this is not the case for the XXZ chain. Here we provide numerical evidence that, at least for the quenches that we consider, the flea gas dynamics presented in Section 4.2 gives rise to the correct dressing of the group velocities.

We first consider the quench from a homogeneous chain prepared in the Néel state. Our results are presented in Fig. 4.4 (a) and (b). The results are for the XXZ chain with $\Delta = 1.5$. The figures show the dressed velocities of the first two strings $v_n(\lambda)$ with $n = 1, 2$ plotted versus the rapidity λ. The full lines are the flea gas results. These are obtained as $\Delta x_\gamma/t$, where Δx_γ is the displacement of the particles with respect to their initial position. The data are averaged over 10^4 realizations of the flea gas dynamics. As it is clear from the Figure, there are large fluctuations in the central region around $\lambda = \pi/2$. This is because the density $\rho_{1,\lambda}$ is large at the edges of the interval, whereas it is suppressed at the center, for instance, for $\Delta = 1.5$ by a factor of ~ 50. This effectively reduces the statistics for the central rapidities. For $n = 2$ the density $\rho_{2,\lambda}$ has a maximum around $\lambda = \pi/2$. However, it is in general much smaller than $\rho_{1,\lambda}$, again resulting in large fluctuations for the group velocities of the two strings. In Fig. 4.4 the dashed-dotted lines are the analytical results for the dressed velocities, which are obtained by solving numerically (1.64). Clearly, the agreement with the flea gas results is very good.

We also considered the dressed velocities in homogeneous thermal states. Panels (c) and (d) show results for the dressed velocities in the state described by the thermal density matrix

$$\rho_0 = \frac{1}{Z} e^{-\beta H + (\beta h) S^z}, \tag{4.19}$$

where β is the inverse temperature and h a transverse magnetic field. The data are for $\beta = 0.5$ and $\beta h = 0.25$. The continuous lines are flea gas results for the dressed velocities of the first two strings, which perfectly match the analytical results of TBA (dashed-dotted lines).

We now move the quenches from piecewise homogeneous states. Here we consider the initial density matrix as

$$\rho_0 = \frac{1}{Z} e^{-\beta_L H_L + (\beta_L h_L) S^z_L} \otimes e^{-\beta_R H_R + (\beta_R h_R) S^z_R}, \tag{4.20}$$

where quantities with the subscript L/R refer to the left and right chains (see Fig. 4.1 (b)). The quench from (4.20) was investigated in Ref. [106] using GHD. Here we

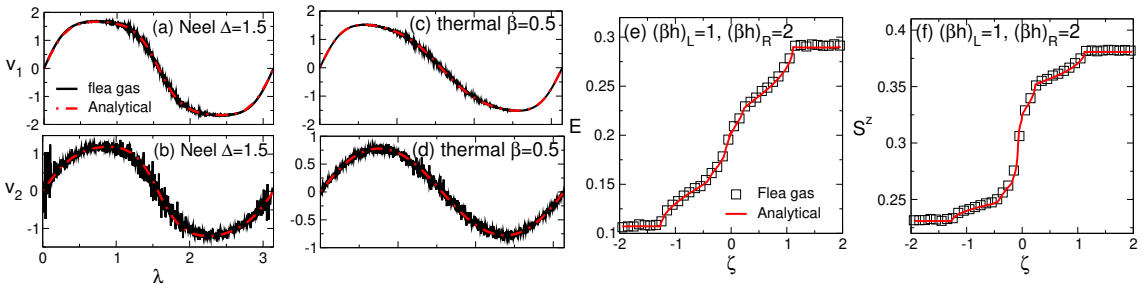

Figure 4.4: Flea gas versus GHD results. Panels (a) and (b) show the dressed group velocities $v_n(\lambda)$ for the first two strings plotted versus the quasiparticle rapidity λ. The black line is the flea gas result. The data are for a chain with $L = 2000$ sites and are averaged over 10^3 realizations of the dynamics. The dashed-dotted line is the solution of (1.64). The results shown are for the quench from the Néel state and $\Delta = 1.5$. Panels (c) and (d) show the values of v_1 and v_2 for the quench from the initial thermal density matrix (4.19). Panels (e) and (f) show profiles of observables in the quench of the XXZ chain with $\Delta = 2$ from the *bipartite thermal* state with $\beta_{\rm L} = \beta_{\rm R} = 0$, $(\beta h)_{\rm L} = 1$, $(\beta h)_{\rm R} = 2$, considered in Ref. [106]. We plot the local energy E and the magnetization S^z as a function of $\zeta \equiv x/t$. The squares represent the flea gas results. The full line was obtained in [106] by solving the GHD equations (1.84). (Figure taken from [209].)

consider $\beta_{\rm L} = 0$, $(\beta h)_{\rm L} = 1$, and $\beta_{\rm R} = 0$, $(\beta h)_{\rm R} = 2$, with h being the magnetic field ($\Delta = 2$). Due to the inhomogeneous initial condition now the dressed velocities depend on $\zeta \equiv x/t$ (see Fig. 4.1 (b)). To check the validity of the flea gas method, in principle, one has to check that the flea gas gives the correct result for $v_{n,\zeta}(\lambda)$ for any ζ. Here, instead, we consider the space-time dependence of the local energy density $E(\zeta)$ and magnetization $S^z(\zeta)$ plotted versus $\zeta = x/t$, with t the time after the quench, and x the distance from the origin of the light-cone. Both the quantities for $x, t \to \infty$ become functions of ζ. In Figure 4.4 (e) and (f) the square symbols are the results of the flea gas simulation for a chain with $L = 2000$ and $t = 100$, whereas the full lines are the analytical results obtained in Ref. [106] by solving the GHD equations. The agreement between the flea gas and the GHD results is spectacular.

As a further check of the validity of the flea gas method we now discuss results for the dynamics of the von Neumann entropy after a quench from homogeneous initial states, for which analytical results (cf. Eq. (4.2)) are available. Our results are discussed in Fig. 4.5. The figure shows data for the XXZ chain with $\Delta = 2$, quenching form the Néel state (see section 4.1). The rescaled entropy S/ℓ is plotted versus t/ℓ, with ℓ the subsystem size. In the simulation we considered $\ell = 100$ and a chain of length $L = 2000$. The data are obtained by averaging over $\sim 10^4$ independent realizations of the flea gas dynamics. The continuous line is the flea gas result (4.18) up to $t/\ell \approx 1.5$, although results for larger times can be easily obtained. The dashed-dotted line is the analytical result (4.2) obtained in Ref. [141]. The agreement between the two is excellent.

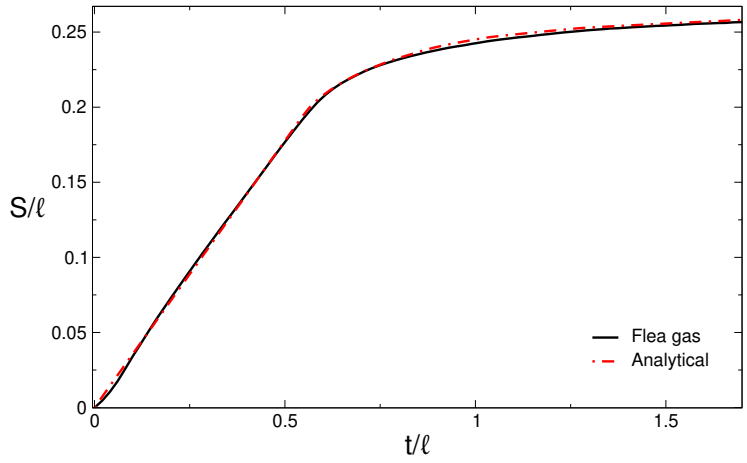

Figure 4.5: Dynamics of the von Neumann entropy after the quench from the Néel state in the XXZ chain with $\Delta = 2$. The entropy density S/ℓ is plotted versus the rescaled time t/ℓ, with ℓ the subsystem size. The continuous line corresponds to the flea gas simulation for a subsystem with $\ell = 100$. The length of the chain is $L = 2000$. The results are averaged over ~ 1000 realization of the dynamics. The dashed-dotted line is the analytical result (4.2). (Figure taken from [209].)

Some remarks are in order. First, the flea gas picture is expected to capture correctly only the ballistic part of the entanglement dynamics, i.e., the leading behavior in t/ℓ. Note that, however, subleading corrections, for instance diffusive corrections as $\mathcal{O}(\sqrt{t})$, are generically expected in the entanglement dynamics. In the flea gas framework diffusive corrections arise because of the average over the different realizations of the initial state, and are associated with the fluctuations of the particles trajectories. On the other hand, the diffusive corrections that are present in the flea gas are not expected to be the same as the quantum diffusive corrections of the XXZ chain. The origin of diffusion in interacting integrable models and in the flea gas have been under constant investigation in the last few years [119–121, 123, 212]. Finally, as it is clear from Fig. 4.5, subleading corrections are small. Only for very short times some deviations from (4.2) are present, which disappear in the scaling limit $t, \ell \to \infty$.

4.3.2 Entanglement dynamics after a quench from inhomogeneous initial conditions

Having established the validity of the flea gas method to simulate the entanglement dynamics after homogeneous quenches, we now consider the case of the inhomogeneous initial state in Fig. 4.1 (b). The calculation of the entanglement dynamics within the GHD framework is in general a complicated task. Explicit analytic results can be obtained only in few cases. For instance, the steady-state value of the von Neumann entropy for a finite subsystem placed next to the interface between

the two chains (see Fig. 4.1 (b)) can be easily calculated. This corresponds to the limit $\ell/t \to 0$. In this limit, the entire subsystem is described by the GGE at $\zeta = 0$. Following Ref. [141], the density of the steady-state von Neumann entropy coincides with that of the GGE entropy with $\zeta = 0$. One has [206]

$$S = \ell \sum_n \int d\lambda s_{n,0}(\lambda). \tag{4.21}$$

Here $s_{n,0}(\lambda)$ is the contribution to the Yang-Yang entropy (cf. (4.3)) of the GGE at $\zeta = 0$, which is obtained by using the GHD (see section 1.4). The result does not depend on which side of the system one places the interval, as long as ℓ is finite. Interestingly, one can show that the $\zeta = 0$ macrostate describes the entanglement growth at short times, i.e., the limit $1 \ll t \ll \ell$ as well [206, 208]. First, the entanglement entropy is expected to grow linearly at short times. Here we refer to the slope of the linear growth as the entanglement production rate [142, 206, 208]. The entanglement growth is due to the quasiparticles that cross the interface between the two chains. This suggests that the entanglement production rate is described by the $\zeta = 0$ GGE. Indeed, if subsystem A is the semi-infinite chain, the entanglement production rate S/t is given as [208]

$$\frac{S}{t} = \sum_n \int d\lambda \mathrm{sign}(\lambda) v_{n,0}(\lambda) s_{n,0}(\lambda). \tag{4.22}$$

Here $v_{\zeta=0,n}(\lambda)$ is the group velocities of the particle-hole excitations around the $\zeta = 0$ GGE, which are obtained from (1.64). For a finite subsystem, the slope of the linear growth depends on the details of the bipartition. For simplicity we now consider the case of a finite interval of length ℓ placed in one of the two chains next to the interface (see Fig. 4.1 (b)). Clearly, the entanglement entropy gets contributions from both the edges of the subsystem. For short enough times but still in the linear regime, i.e, for large t with $t/\ell \ll 1$, the contributions of the two edges decouple and can be summed independently. As in (4.22), one of the edges of A is described by the GGE with $\zeta = 0$. On the other hand, the other one is described by the GGE with $\zeta = \pm\infty$, depending on which side subsystem A is placed in. The entanglement production rate is given as

$$S = t \sum_n \int d\lambda \Big[\mathrm{sign}(\lambda) v_{n,0}(\lambda) s_{n,0}(\lambda) + |v_{n,\zeta\to\infty}(\lambda)| s_{n,\sigma\infty}(\lambda) \Big], \tag{4.23}$$

where $\sigma = \pm$ identifies the side in which subsystem A is placed.

To illustrate how these features emerge in the flea gas simulations, in Fig. 4.6 we present numerical results for the quench from the initial state obtained by joining the Néel state and the dimer state $|\mathrm{N}\rangle \otimes |\mathrm{D}\rangle$ (see Section 4.1 for the definition of these states). The results are for the XXZ chain with $\Delta = 2$. The full and dotted lines correspond to the bipartitions with interval A being $[-\ell, 0]$ (in the Néel region) and $[0, \ell]$ (in the dimer region) respectively. In both cases we consider $L = 2000$ and $\ell = 100$. The results are obtained by averaging over 10000 realizations of the "flea" gas dynamics (see section 4.2), and using (4.18).

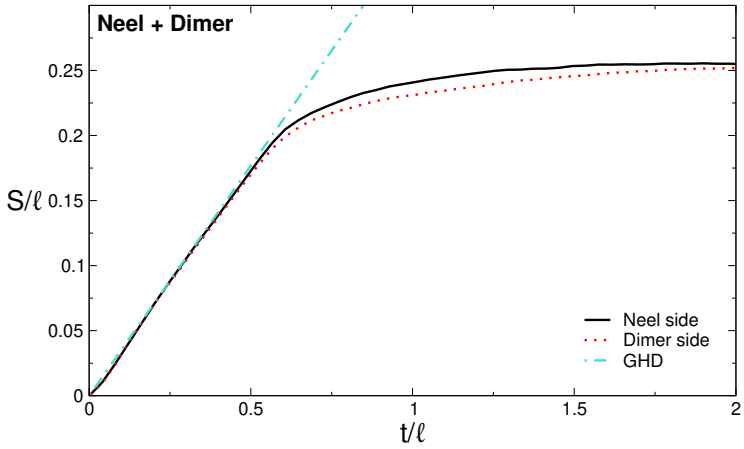

Figure 4.6: Dynamics of the von Neumann entropy after the quench from the initial state obtained by joining the Néel and the dimer state in the XXZ chain with $\Delta = 2$. The entropy density S/ℓ is plotted versus the rescaled time t/ℓ, with ℓ being the subsystem size. The interval is placed next to the interface between the two chains. Here we choose $\ell = 100$, while the total chain size is $L = 2000$. The full and the dotted lines are the flea gas results for an interval placed in the Néel and dimer part, respectively. The results are obtained by averaging over ~ 10000 realizations of the dynamics. The dashed-dotted line is the GHD prediction (4.23) valid in the space-time scaling limit. Notice that the asymptotic value of the entropy at $t \to \infty$ does not depend on the region where the subsystem is placed. (Figure taken from [209].)

For the quench from $|\mathrm{N} \otimes \mathrm{dimer}\rangle$, we observe that at $\Delta = 2$ one has $s_{n,\lambda}(+\infty) \approx s_{n,-\infty}(\lambda)$ and $v_{n,+\infty}(\lambda) \approx v_{n,-\infty}(\lambda)$. From (4.23) one obtains that the entanglement production rate depends very mildly on which region the subsystem is placed. The theory predictions (4.23) for the entanglement production rates are not distinguishable on the scale of the figure and are reported as dashed-dotted line. At intermediate $\zeta = t/\ell$, the entanglement entropy depends on all the values of ζ. This happens because the entangling quasiparticles explore macrostates with different ζ as they travel in subsystem A (see Fig. 4.1). Although it is possible, in principle, to write an analytic formula [208] for the evolution of the entanglement entropy at any time, its numerical evaluation is a demanding task. In contrast, the flea gas method allows to access easily the full-time entanglement dynamics, as it is clear from Fig. 4.6.

In Fig. 4.7 we present further checks of the validity of the flea gas method for inhomogeneous quenches. We consider the initial state obtained by joining the tilted Néel state and the dimer state, i.e., $|\mathrm{N}, \theta\rangle \otimes |\mathrm{dimer}\rangle$ (see section 4.1), where θ is the tilting angle. Panel (a) and (b) show results for $\theta = \pi/3$, whereas in (c) and (d) we consider $\theta = \pi/6$. In all the cases we choose $\ell = 100$ and total system size $L = 2000$. In (a) and (d) the subsystem is placed on the Néel side ($A = [-\ell, 0]$), whereas in (b)

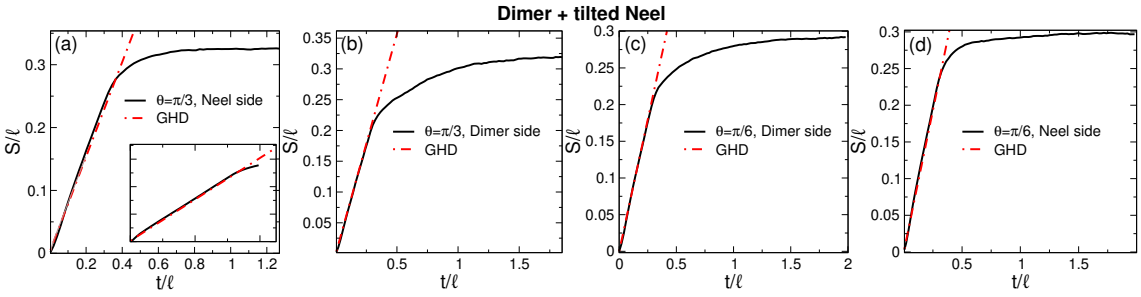

Figure 4.7: The same as in Fig. 4.6 for the quench from the state obtained by joining the tilted Néel and the dimer state. The data are for the XXZ chain at $\Delta = 2$ and for tilting angles $\theta = \pi/3$ (in (a) and (b)) and $\theta = \pi/6$ (in (c) and (d)). The curves show the flea gas results for a subsystem of size $\ell = 100$ and chain size $L = 2000$. The data are averaged over ~ 10000 realizations of the flea gas dynamics. In (a) and (d) the subsystem is placed on the Néel side, whereas in (b) and (c) it is in the dimer side. The dashed-dotted lines are the GHD predictions in the space-time scaling limit. The inset in (a) shows results for $\ell = 500$ and chain size $L = 2000$. (Figure taken from [209].)

and (c) is in the dimer side ($A = [0, \ell]$). The fact that the production rate depends on the position of the interval is now apparent. The dashed-dotted lines are the theory predictions (cf. (4.23)) for the entanglement production rates. In Fig. 4.7 (a) some deviations from (4.23) are visible. These, however, are due to finite-size and finite-time effects. In the inset of Fig. 4.7 we report results for $\ell = 500$, which are now in perfect agreement with (4.23). We observe that in general very large subsystems are needed to provide a robust numerical check of the GHD prediction (4.23).

4.3.3 Mutual information after quenches from inhomogeneous initial conditions

It is interesting to investigate the dynamics of the mutual information between two intervals. To this purpose, we now consider a tripartite system. Subsystem A is made of two intervals A_1 and A_2 at a distance d. Here we consider only $d = 0$, although the method works also for $d > 0$. The two subsystems are embedded in an infinite system. The mutual information $I_{A_1:A_2}$ is a measure of the correlation shared between A_1 and A_2, although it is not a proper measure of the entanglement between them. $I_{A_1:A_2}$ is defined as

$$I_{A_1:A_2} \equiv S_{A_1} + S_{A_2} - S_{A_1 \cup A_2}, \tag{4.24}$$

where S_{A_1}, S_{A_2}, and $S_{A_1 \cup A_2}$ are the von Neumann entanglement entropies of A_1, A_2 and $A_1 \cup A_2$ with the rest of the system.

In the quasiparticle picture, the mutual information is proportional to the entangled pairs that are shared only between A_1 and A_2. On the other hand, the

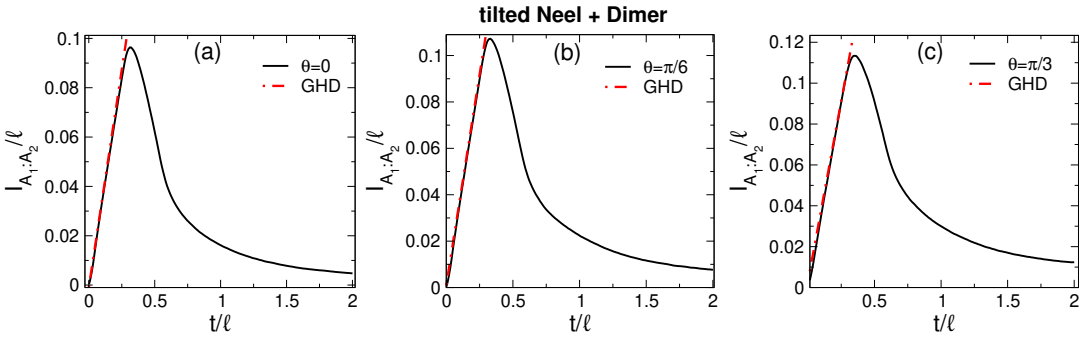

Figure 4.8: Dynamics of the mutual information between two intervals after the quench from the state $|\text{Néel}, \theta\rangle \otimes |\text{dimer}\rangle$ in the XXZ chain with $\Delta = 2$. Here we show the mutual information between two adjacent intervals next to the interface between the two chains. The data are for two intervals with $\ell = 100$ embedded in a chain with . The different panels are for different tilting angles θ. The dashed-dotted lines are the GHD predictions for the slope of the linear growth at short times. Notice that the slope depends on the macrostate with $\zeta = 0$ that describes the interface between the two chains. (Figure taken from [209].)

contribution of the quasiparticles to the mutual information is, again, the GGE thermodynamic entropy. Thus, the flea gas formula for $I_{A_1:A_2}$ is the same as (4.18) where the sum is restricted to the pairs of quasiparticles shared between A_1 and A_2.

The qualitative behavior of the mutual information is as follows. For two disjoint intervals at a distance d, the mutual information is zero at short times. At $t \sim d/t$, $I_{A_1:A_2}$ exhibits a linear increase. This corresponds to entangled pairs starting to be shared between A_1 and A_2. The growth persists up to $t \sim (d + \ell)/t$, when the mutual information starts to decrease. In systems with only one quasiparticle with perfect linear dispersion (as in CFT systems), the decrease is linear. In generic integrable models a much slower decrease is observed [142]. This is due to the fact that quasiparticles have a nontrivial dispersion, and slow quasiparticles entangle the two subsystems at long times. The mutual information can, in principle, be used as a tool to reveal the quasiparticle content of an integrable model. Typically, different species have different maximum velocities $v_n(\lambda_{\max})$. This implies that if the distance between the two intervals is large enough, the mutual information exhibits a multi-peak structure in time, each peak corresponding to a different species [88, 213].

The mutual information after quenches from inhomogeneous initial states has not been investigated yet. In contrast with homogeneous global quenches [142], deriving the quasiparticle picture for the mutual information in inhomogeneous settings is a formidable task. Again, the reason is that the quasiparticles trajectories are non trivial functions of time. We now show that the flea gas approach allows to simulate effectively the full-time dynamics of the mutual information. We restrict ourselves to the case of two adjacent intervals, although the method works for disjoint intervals

as well.

We present our results in Fig. 4.8, focusing on the XXZ chain with $\Delta = 2$. The initial state that we consider is $|\mathrm{N}, \theta\rangle \otimes |\mathrm{D}\rangle$. Different panels show different values of θ. The data are for two equal-length adjacent intervals $[-\ell, 0]$ and $[0, \ell]$ with $\ell = 100$. The total chain length is $L = 2000$. As expected, the mutual information is initially zero, it grows linearly at intermediate times, and it eventually decays to zero at asymptotically long times. Importantly, the initial slope of the mutual information depends only on the GGE with $\zeta = 0$ because the interface between A_1 and A_2 is at the origin. In particular, the slope of the initial growth of the mutual information coincides with the entanglement production rate for the two semi-infinite chains (see Eq. (4.22)). This initial growth is reported in Fig. 4.8 as dashed-dotted line, and it perfectly describes the behavior of the flea gas results.

4.4 Discussion

In this Chapter we showed that the so-called flea gas method put forward in Ref. [113] provides a versatile tool for simulating the entanglement dynamics after quenches from generic initial states in integrable systems. We benchmarked the method in the Heisenberg XXZ chain, although it can be applied, in principle, to any integrable model. The method works for arbitrary initial states, both globally homogeneous as well as piecewise homogeneous. For globally homogeneous quenches the approach requires only the GGE macrostate that describes the steady-state. For piecewise homogeneous states, the key ingredients are the GGE macrostates describing the steady-state in the bulk of the two systems. Although in this case the entanglement dynamics can be obtained, in principle, by combining the quasiparticle picture with the Generalized Hydrodynamics, obtaining explicit formulas [208] is a demanding task because the trajectories of the quasiparticles are non trivial functions of time. Indeed, results can be obtained only in some limits. In contrast, in this Chapter we showed that the flea gas approach allows to obtain easily the full-time dynamics of the entanglement entropy and of the mutual information between two intervals. Thus, the method paves the way to the study of entanglement dynamics using "molecular dynamics" simulations.

Our results open several possible new research directions. First, it would be important to investigate whether it is possible to prove analytically that for the XXZ chain the flea gas dynamics as described in section 4.2.1 gives the correct dressing for the group velocities.

Also, it would be useful to apply the method to more complicated setups, such as multipartite systems, or different initial states. Also, it would be important to go beyond the ballistic regime, studying corrections to the linear entanglement growth. This requires first to understand the subleading diffusive corrections in the flea gas method. Second, it requires to modify the flea gas dynamics to correctly reproduce the diffusive corrections that arise from the quantum fluctuations [119, 120]. An interesting direction would be to generalize the flea gas approach to study the entanglement dynamics in the presence of defects or impurities. Finally, it would

be enlightening to understand whether it is possible to treat the entanglement of operators in integrable spin chains by using the flea gas approach, generalizing the results of Ref. [214] for the Rule 54 chain.

Chapter 5

Spin–charge separation effects in the generalized hydrodynamics of the Yang–Gaudin model

In this Chapter we study the generalized hydrodynamics of the repulsive Yang–Gaudin model, which is a system of one-dimensional spin-1/2 fermions with repulsive delta-function interactions. The Hamiltonian of the model is

$$\begin{aligned} H = &- \int_{-L/2}^{L/2} dx \left[\sum_{\sigma=\pm} \Psi_\sigma^\dagger(x)(\partial_x^2 + A + \sigma h)\Psi_\sigma(x) \right] \\ &+ c \int_{-L/2}^{L/2} dx \left[\sum_{\sigma,\sigma'=\pm} \Psi_\sigma^\dagger(x)\Psi_{\sigma\prime}^\dagger(x)\Psi_{\sigma\prime}(x)\Psi_\sigma(x) \right], \end{aligned} \tag{5.1}$$

where A is the chemical potential and h is the magnetic field, and c is the interaction strength. The fermionic field $\Psi_\sigma(x)$ satisfies canonical anticommutation relations. A salient feature of this model is that its Bethe ansatz solution has a nested structure, and thus it admits two different species of quasiparticles. One species corresponds to the charge and the other corresponds to the spin degrees of freedom. In this Chapter we investigate whether the existence of these two species carries a signature in the hydrodynamics of the model.

In order to study the hydrodynamics of the Yang–Gaudin model, we consider the bipartite quench protocol with the initial state described by the density matrix

$$\rho_0 = \frac{1}{Z}\left(e^{-\beta_L H_L} \bigotimes e^{-\beta_R H_R}\right), \tag{5.2}$$

illustrated in Fig. 1.1. By generalizing the GHD framework to the Yang–Gaudin model, we compute the space-time dependent density profiles of various conserved quantities. We show that at generic temperatures the existence of two species is not apparent in the structure of the space-time profiles. We show, however, that at low temperatures, the profile of the energy density and the energy current density can be described by the superposition of two uncoupled CFTs, one corresponding

to the charge degrees of freedom, and the other corresponding to the spin degrees of freedom. Thus a notion of spin–charge separation appears in the low-temperature hydrodynamics of the Yang–Gaudin model.

The organization of this Chapter is the following. We begin by summarizing the Bethe ansatz solution of the Yang–Gaudin model together with its thermodynamics in Section 5.1. Then in Section 5.2 we generalize the GHD framework to the Yang–Gaudin model and show that the presence of two particle species is not apparent in the hydrodynamics at general temperatures. Finally, in Section 5.3 we carry out the low temperature expansion of GHD and interpret the results as a spin–charge separation effect. Some technical details of the calculations are relegated to appendices.

5.1 The Yang–Gaudin model

In this Section we summarize the Bethe ansatz solution and the thermodynamics of the Yang–Gaudin model. The general solution for the spectrum of was given by Gaudin and Yang [215, 216], after partial results for the special case of $M = 1$ [217] and $M = 2$ [218] down spins. The thermodynamics of the model was first described by Takahashi [219].

The Hamiltonian (5.1) has $U(2) = U(1) \times SU(2)$ symmetry. It commutes with the number of particles and the number of down spins

$$\hat{N} = \int_{-L/2}^{L/2} dx \sum_{\sigma=\pm} \Psi_\sigma^\dagger(x)\Psi_\sigma(x), \tag{5.3}$$

as well as the number of down spins

$$\hat{M} = \int_{-L/2}^{L/2} dx\, \Psi_-^\dagger(x)\Psi_-(x). \tag{5.4}$$

In the sector of N particles with M down spins, the first quantized Hamiltonian corresponding to (5.1) is

$$\mathcal{H} = -\sum_{j=1}^{N} \left[\left(\frac{\partial}{\partial x_j} \right)^2 + A \right] - h(N - 2M) + 2c \sum_{j \neq k}^{N} \delta(x_j - x_k). \tag{5.5}$$

This Hamiltonian is solvable by nested Bethe ansatz. The particles are labeled $1, \ldots, N$, their positions are $x_1, \ldots, x_N$ and their spins are $s_1, \ldots, s_N$, with M spins pointing downwards and $N - M$ upwards. Then the eigenfunctions are superpositions of plane wave functions [215, 216]

$$\psi_{\mathbf{k},\boldsymbol{\lambda}}(\mathbf{x}) = \sum_P [Q, P] \exp\left[i \left(k_{P_1} x_{Q_1} + k_{P_2} x_{Q_2} + \ldots k_{P_N} x_{Q_N} \right) \right], \tag{5.6}$$

where Q is the permutation for which $x_{Q_1} < x_{Q_2} < \cdots < x_{Q_N}$ and the summation over P is a summation over all possible permutations of N labels. The coefficients of the plane wave functions are

$$[Q, P] = (-1)^{\sigma(P)} \Phi(y_1, y_2, \ldots, y_M; P). \tag{5.7}$$

where $\sigma(P)$ is the inversion number of the permutation P and $y_1, \ldots, y_M$ are the position of the labels of down spin particles in the sequence of labels $Q_1, Q_2, \ldots, Q_N$. The functions $\Phi(y_1, y_2, \ldots, y_M)$ have again a Bethe ansatz structure

$$\Phi(y_1, \ldots, y_M) = \sum_R A(R) F_P(\lambda_{R_1}, y_1) F_P(\lambda_{R_2}, y_2) \ldots F_P(\lambda_{R_M}, y_M), \tag{5.8}$$

which is the namesake of 'nested Bethe ansatz'. However, the functions $F_P(\lambda, y)$ are not plane waves, they are

$$F_P(\lambda, y) = \prod_{j=1}^{y-1} (k_{P_j} - \lambda + ic/2) \prod_{\ell=y+1}^{N} (k_{P_\ell} - \lambda - ic/2). \tag{5.9}$$

Finally, the coefficients $A(R)$ of the inner wave function (5.8) are

$$A(R) = (-1)^{\sigma(R)} \prod_{j<\ell} (\lambda_{R_j} - \lambda_{R_\ell} - ic), \tag{5.10}$$

which is the usual structure of Bethe ansatz coefficients.

In the following, we will not need to consider the complicated structure of the nested wave functions (5.6)–(5.10), for the sake of thermodynamics and hydrodynamics it is sufficient to *enumerate the wave functions*. Different wave functions are labelled by the sets of parameters $\boldsymbol{k} = \{k_1, \ldots, k_N\}$ and $\boldsymbol{\lambda} = \{\lambda_1, \ldots, \lambda_N\}$, which together identify the eigenstate. The periodic boundary conditions constrain the parameters, yielding the *nested* Bethe equations [215, 216]

$$e^{ik_j L} = \prod_{\alpha=1}^{M} \frac{k_j - \lambda_\alpha + ic/2}{k_j - \lambda_\alpha - ic/2}, \tag{5.11}$$

$$\prod_{j=1}^{N} \frac{\lambda_\alpha - k_j + ic/2}{\lambda_\alpha - k_j - ic/2} = \prod_{\substack{\beta=1 \\ \beta \neq \alpha}} \frac{\lambda_\alpha - \lambda_\beta + ic}{\lambda_\alpha - \lambda_\beta - ic}. \tag{5.12}$$

In the solution of (5.11)–(5.12), the physical wave numbers k_j are real, while the auxiliary rapidities λ_α are in general complex.

5.1.1 Thermodynamics

The thermodynamics of the Yang–Gaudin model was developed by Takahashi [219], where the standard Thermodynamic Bethe Ansatz was generalized to the Bethe ansatz equations (5.11)–(5.12).

In the thermodynamic limit

$$N \to \infty, \quad N/L = \text{const.}, \quad M/L = \text{const.}, \tag{5.13}$$

the solutions of the BAE satisfy the string hypothesis. The string hypothesis states that in the solution of (5.11)–(5.12) the physical rapidities k_j are real and the auxiliary rapidities λ_j form strings of complex numbers. An n-string consists of n complex

rapidities distributed symmetrically around the real axis, with the jth rapidity in the αth n-string being

$$\lambda^n_{\alpha,j} = \lambda^n_\alpha + \frac{ic}{2}(n+1-2j) \qquad \lambda^n_\alpha \in \mathbb{R}. \tag{5.14}$$

Here, the real number λ^n_α is the string centre. In the thermodynamic limit, the total number of wave numbers k_j and string centres λ^n_α tends to infinity and both develop a nonzero density over the real line. Similarly to the procedure in the XXZ model (see Section 1.2.2 for details), it is useful to introduce the density of particles for both species,

$$\rho^{(1)}_1(k_j) \sim \frac{1}{L}\frac{1}{k_{j+1}-k_j}\,, \tag{5.15}$$

$$\rho^{(2)}_n(\lambda^n_\alpha) \sim \frac{1}{L}\frac{1}{\lambda^n_{\alpha+1}-\lambda^n_\alpha}. \tag{5.16}$$

In the rest of the Thesis the physical particles will be labeled *species 1* and the auxiliary particles will be labeled *species 2*, as seen in the upper index of $\rho^{(1)}(\lambda)$ and $\rho^{(2)}_n(\lambda)$.

The densities define thermodynamic macrostates in the sense that a given set of density functions $\boldsymbol{\rho} = \{\rho^{(1)}, \rho^{(2)}_n\}$ uniquely determines the expectation values of local observables. However, a set of density functions corresponds to an extensive number of eigenstates (or microstates). The number of such eigenstates is given by the Yang–Yang entropy

$$s_{\mathrm{YY}}[\boldsymbol{\rho}] = \int_{-\infty}^{\infty} d\lambda \, \left[s^{(1)}(\lambda) + s^{(2)}_n(\lambda) \right], \tag{5.17}$$

where

$$s^{(1)}(\lambda) \equiv \rho^{(1)}_{\mathrm{t}}(\lambda)\ln\rho^{(1)}_{\mathrm{t}}(\lambda) - \rho^{(1)}(\lambda)\ln\rho^{(1)}(\lambda) - \rho^{(1)}_{\mathrm{h}}(\lambda)\ln\rho^{(1)}_{\mathrm{h}}(\lambda), \tag{5.18}$$

$$s^{(2)}_n(\lambda) \equiv \rho^{(2)}_{\mathrm{t},n}(\lambda)\ln\rho^{(2)}_{\mathrm{t},n}(\lambda) - \rho^{(2)}_n(\lambda)\ln\rho^{(2)}_n(\lambda) - \rho^{(2)}_{\mathrm{h,n}}(\lambda)\ln\rho^{(2)}_{\mathrm{h,n}}(\lambda). \tag{5.19}$$

In these equations the hole densities $\rho^{(1)}_{\mathrm{h}}(\lambda)$ and $\rho^{(2)}_{n,\mathrm{h}}(\lambda)$ denote the density of unoccupied quantum numbers in rapidity space, and

$$\rho^{(1)}_{\mathrm{t}}(\lambda) \equiv \rho^{(1)}(\lambda) + \rho^{(1)}_{\mathrm{h}}(\lambda)\,, \qquad \rho^{(2)}_{n,\mathrm{t}}(\lambda) \equiv \rho^{(2)}_n(\lambda) + \rho^{(2)}_{\mathrm{h,n}}(\lambda)\,. \tag{5.20}$$

are the density of states. By virtue of the Bethe equations (5.11)–(5.12), they satisfy the Bethe–Gaudin–Takahashi equations

$$\rho^{(1)}_{\mathrm{t}}(\lambda) = \frac{1}{2\pi} + \sum_{m=1}^{\infty} a_m \star \rho^{(2)}_m(\lambda), \tag{5.21}$$

$$\rho^{(2)}_{\mathrm{t},n}(\lambda) = a_n \star \rho^{(1)}(\lambda) - \sum_{m=1}^{\infty} A_{nm} \star \rho^{(2)}_m(\lambda). \tag{5.22}$$

In these BGT equations $f \star g$ means the convolution

$$f \star g(\lambda) = \int_{-\infty}^{\infty} \mathrm{d}\mu f(\lambda - \mu) g(\mu), \tag{5.23}$$

and the special functions $a_n(\lambda)$, $A_{nm}(\lambda)$ are

$$a_n(x) \equiv \frac{1}{\pi} \frac{2nc}{(nc)^2 + 4x^2}, \tag{5.24}$$

$$\begin{aligned} A_{nm}(x) \equiv{}& (1 - \delta_{nm}) a_{|n-m|}(x) \\ &+ 2a_{|n-m|+2}(x) + 2a_{|n-m|+4}(x) + \cdots + 2a_{n+m-2}(x) + a_{n+m}(x). \end{aligned} \tag{5.25}$$

Despite the large number of eigenstates corresponding to the state $\boldsymbol{\rho}$, it is generally accepted that the expectation values of local observables are fully determined by the densities alone. For example, the number of particles, the magnetization and the energy are expressed as

$$n[\boldsymbol{\rho}] = d^{(1)}[\boldsymbol{\rho}], \tag{5.26}$$

$$m[\boldsymbol{\rho}] = d^{(1)}[\boldsymbol{\rho}]/2 - d^{(2)}[\boldsymbol{\rho}]\,, \tag{5.27}$$

$$e[\boldsymbol{\rho}] = \int_{-\infty}^{\infty} \mathrm{d}k\, \rho_1^{(1)}(k)\, e(k) - 2m[\boldsymbol{\rho}]h\,, \tag{5.28}$$

where the bare energy $e(k) = k^2 - A$ is introduced and

$$d^{(1)}[\boldsymbol{\rho}] = \int_{-\infty}^{\infty} \mathrm{d}\lambda\, \rho_1^{(1)}(\lambda), \tag{5.29}$$

$$d^{(2)}[\boldsymbol{\rho}] = \sum_{n=1}^{\infty} \int_{-\infty}^{\infty} \mathrm{d}\lambda\, \rho_n^{(2)}(\lambda) n \tag{5.30}$$

are the density of the physical and the auxiliary species.

The thermodynamics of the system is described by a single macrostate $\boldsymbol{\rho}_T = \{\rho_T^{(1)}, \rho_{n,T}^{(2)}\}$ that minimizes the free energy

$$f_{T,A,h}[\boldsymbol{\rho}] = e[\boldsymbol{\rho}] - T\, s_{\mathrm{YY}}[\boldsymbol{\rho}]\,. \tag{5.31}$$

The saddle-point equations describing the minimum are [219]

$$\varepsilon_T^{(1)}(\lambda) = e(\lambda) - h - T \sum_{n=1}^{\infty} a_n \star \log(1 + e^{-\varepsilon_{n,T}^{(2)}/T})(\lambda)\,, \tag{5.32}$$

$$\begin{aligned} \varepsilon_{n,T}^{(2)}(\lambda) ={}& 2nh - T a_n \star \log(1 + e^{-\varepsilon_T^{(1)}/T})(\lambda) \\ &+ \sum_{m=1}^{\infty} A_{nm} \star \log(1 + e^{-\varepsilon_{m,T}^{(2)}/T})(\lambda)\,, \end{aligned} \tag{5.33}$$

where thermal dressed energies $\varepsilon_{n,T}^{(r)}(\lambda) \equiv T \log(\rho_{n,\mathrm{h},T}^{(r)}(\lambda)/\rho_{n,T}^{(r)}(\lambda))$ are introduced. Once the solution of (5.32)–(5.33) is known, one can use the definition of $\varepsilon_{n,T}^{(r)}(\lambda)$

and the BGT equations (5.21)–(5.22) to compute the thermal string densities $\boldsymbol{\rho}_T$, and then (5.26)–(5.28) to compute thermal expectation values of charges.

There is a decoupled form of the saddle-point equations (5.32)–(5.33), which reads [219]

$$\varepsilon^{(1)}_{1,T} = (\lambda^2 - A) - T\Big[r \star \log(1 + e^{-\varepsilon^{(1)}_{1,T}/T}) - s \star \log(1 + e^{\varepsilon^{(2)}_{1,T}/T})\Big], \tag{5.34}$$

$$\varepsilon^{(2)}_{1,T} = T\left[s \star \log\left(\frac{1 + e^{\varepsilon^{(2)}_{2,T}/T}}{1 + e^{-\varepsilon^{(1)}_{1,T}/T}}\right)\right], \tag{5.35}$$

$$\varepsilon^{(2)}_{n,T} = T\left[s \star \log\Big((1+e^{\varepsilon^{(2)}_{n-1,T}/T})(1+e^{\varepsilon^{(2)}_{n+1,T}/T})\Big)\right], \qquad (n \geq 2), \tag{5.36}$$

$$\lim_{n\to\infty} \frac{\log \varepsilon^{(2)}_{n,T}}{n} = \frac{2h}{T}\,, \tag{5.37}$$

where the special functions $s(x)$ and $r(x)$ are

$$s(x) \equiv \frac{1}{2c}\mathrm{sech}\left(\frac{\pi x}{c}\right)\,, \qquad\qquad r(x) = a_1 \star s(x)\,. \tag{5.38}$$

The decoupled equations (5.34)–(5.37) are equivalent to (5.32)–(5.33). Moreover, (5.36) shows explicitly that $\varepsilon^{(2)}_{n,T}(\lambda)$ is positive for $n \geq 2$, that is, the pseudoenergies of the bound states are always positive. Therefore bound states are absent from the ground state, and they are exponentially suppressed in the low-temperature thermodynamics. This fact is discussed in detail in Section 5.3.

5.1.2 Conserved currents

Similarly to the conserved currents of other integrable models, such as the XXZ model described in Section 1.2.4, it is possible to conjecture integral formulas for the conserved currents of the Yang–Gaudin model. Let us consider a generic conserved charge Q, whose the density in the TDL is given by

$$q[\boldsymbol{\rho}] \equiv \int_{-\infty}^{\infty} \mathrm{d}\lambda\, \rho^{(1)}(\lambda)\, q^{(1)}(\lambda) + \sum_{n=1}^{\infty} \int_{-\infty}^{\infty} \mathrm{d}\lambda\, \rho^{(2)}_n(\lambda)\, q^{(2)}_n(\lambda)\,, \tag{5.39}$$

where $\{q^{(1)}(\lambda), q^{(2)}_n(\lambda)\}$ are some known functions, which depend on Q. The expectation value of the current density of the charge is then

$$j_q[\boldsymbol{\rho}] = \int_{-\infty}^{\infty} \mathrm{d}\lambda\, v^{(1)}(\lambda)\rho^{(1)}(\lambda)\, q^{(1)}(\lambda) \,+ \sum_{n=1}^{\infty} \int_{-\infty}^{\infty} \mathrm{d}\lambda\, v^{(2)}_n(\lambda)\rho^{(2)}_n(\lambda)\, q^{(2)}_n(\lambda)\,. \tag{5.40}$$

Here the velocities $\{v^{(1)}(\lambda), v^{(2)}_n(\lambda)\}$ are defined as

$$v^{(1)}(\lambda) \equiv \frac{\partial \varepsilon^{(1)}(\lambda)}{\partial p^{(1)}(\lambda)} = \frac{\varepsilon^{(1)\prime}(\lambda)}{2\pi\rho^{(1)}_{\mathrm{t}}(\lambda)}, \qquad v^{(2)}_n(\lambda) \equiv \frac{\partial \varepsilon^{(2)}_n(\lambda)}{\partial p^{(2)}_n(\lambda)} = \frac{\varepsilon^{(2)\prime}_n(\lambda)}{2\pi\rho^{(2)}_{n,\mathrm{t}}(\lambda)}\,, \tag{5.41}$$

where the prime denotes the derivative with respect to λ, and they can be obtained by solving the system of linear integral equations

$$v^{(1)}\rho^{(1)}_{\mathrm{t}}(\lambda) = \frac{e'(\lambda)}{2\pi} + \sum_{m=1}^{\infty} a_m \star v^{(2)}_m \rho^{(2)}_m(\lambda), \tag{5.42}$$

$$v^{(2)}_n \rho^{(2)}_{n,\mathrm{t}}(\lambda) = a_n \star v^{(1)}\rho^{(1)}(\lambda) - \sum_{m=1}^{\infty} A_{nm} \star v^{(2)}_m \rho^{(2)}_m(\lambda). \tag{5.43}$$

We derived these equations analogously to the derivation in the XXZ model [31]. We stress that (5.40)–(5.43) is a conjecture, which has yet to be proved in this particular model. Proofs of analogous formulas exist in the Lieb–Liniger model [32], generic integrable field theories [133], and very recently, the XXZ model [134]. We expect the formulas to be valid generally in Bethe ansatz solvable systems.

As special cases of (5.40), the mean values of the currents associated to the conserved charges (5.26)–(5.30) can be computed by

$$j_n[\boldsymbol{\rho}] = \int_{-\infty}^{\infty} \mathrm{d}\lambda\, v^{(1)}(\lambda)\rho^{(1)}(\lambda)\,, \tag{5.44}$$

$$j_m[\boldsymbol{\rho}] = j_n[\boldsymbol{\rho}]/2 - \sum_{n=1}^{\infty} \int_{-\infty}^{\infty} \mathrm{d}\lambda\, v^{(2)}_n(\lambda)\rho^{(2)}_n(\lambda)\, n\,, \tag{5.45}$$

$$j_e[\boldsymbol{\rho}] = \int_{-\infty}^{\infty} \mathrm{d}k\, v^{(1)}(k)\rho^{(1)}(k)\,(k^2 - A) + 2h j_m[\boldsymbol{\rho}]\,. \tag{5.46}$$

In Section 5.3, we will consider the low-temperature expansion of the energy current density (5.46), along with the energy density (5.28), to study the question of spin–charge separation.

5.2 Generalized Hydrodynamics of the Yang–Gaudin model

In this section we show the generalization of the GHD framework to the Yang–Gaudin model and discuss that the nested structure of the model is not apparent in its hydrodynamics at general temperatures. The validity of the GHD description is based only on the fact that the system varies slowly in space and time, therefore it can be divided into small, homogeneous cells described by a local, quasi-stationary GGE. It is straightforward to generalize the argument for the XXZ model presented in Section 1.4, and derive continuity equations for the particle densities

$$\begin{aligned} \partial_t \rho^{(1)}_{x,t}(\lambda) + \partial_x(v^{(1)}_{x,t}(\lambda)\rho^{(1)}_{x,t}(\lambda)) = 0, \\ \partial_t \rho^{(2)}_{n;x,t}(\lambda) + \partial_x(v^{(2)}_{n;x,t}(\lambda)\rho^{(2)}_{n;x,t}(\lambda)) = 0, \end{aligned} \tag{5.47}$$

which are analogous to 1.84. In the bipartite setting, the densities will depend only on $\zeta = x/t$. Similarly to the XXZ model, it can be shown that the normal modes of

the continuity equations turn out to be the filling functions

$$\vartheta_\zeta^{(1)}(\lambda) = \frac{\rho_\zeta^{(1)}(\lambda)}{\rho_{\mathrm{t},\zeta}^{(1)}(\lambda)}, \qquad \vartheta_{n,\zeta}^{(2)}(\lambda) = \frac{\rho_{n,\zeta}^{(2)}(\lambda)}{\rho_{n,\mathrm{t},\zeta}^{(2)}(\lambda)}. \tag{5.48}$$

Using the filling functions, (5.47) can be transformed into

$$\begin{aligned} \left(\zeta - v_\zeta^{(1)}(\lambda)\right) \partial_\zeta \vartheta_\zeta^{(1)}(\lambda) = 0, \\ \left(\zeta - v_{n,\zeta}^{(2)}(\lambda)\right) \partial_\zeta \vartheta_{n,\zeta}^{(2)}(\lambda) = 0. \end{aligned} \tag{5.49}$$

In the bipartite setting (5.2), the solution to these equations is

$$\begin{aligned} \vartheta_\zeta^{(1)}(\lambda) &= \vartheta_{T_\mathrm{L}}^{(1)}(\lambda)\Theta_H(v_\zeta^{(1)}(\lambda) - \zeta) + \vartheta_{T_\mathrm{R}}^{(1)}(\lambda)\Theta_H(\zeta - v_\zeta^{(1)}(\lambda))\,, \\ \vartheta_{n,\zeta}^{(2)}(\lambda) &= \vartheta_{n,T_\mathrm{L}}^{(2)}(\lambda)\Theta_H(v_{n,\zeta}^{(2)}(\lambda) - \zeta) + \vartheta_{n,T_\mathrm{R}}^{(2)}(\lambda)\Theta_H(\zeta - v_{n,\zeta}^{(2)}(\lambda))\,, \end{aligned} \tag{5.50}$$

where $\Theta_H(x)$ is the Heaviside step function

$$\Theta_H(x) = \begin{cases} 1 & \text{if } x > 0, \\ 0 & \text{if } x \leq 0. \end{cases} \tag{5.51}$$

The functions $\vartheta_{n,T}^{(r)}$ in (5.50) are the filling functions at the temperatures of the bath on the left and right side (i.e., the temperatures at $\zeta \to \pm\infty$). The solution (5.50) is implicit, since the velocities $\boldsymbol{v}_\zeta$ depend on the filling fractions $\boldsymbol{\vartheta}_\zeta = \{\vartheta_{1,\zeta}^{(1)}, \vartheta_{m,\zeta}^{(2)}\}$. Similarly to the case of non-nested systems, one can solve this set of equations numerically by iteration. The solution $\boldsymbol{\vartheta}_\zeta$ can then be used to compute the root densities by solving the BGT equations (5.21)–(5.22).

5.2.1 The absence of nested structure at general temperatures

The main question of this Chapter is whether the nested structure of the Yang–Gaudin model appears in its hydrodynamics. In order to answer this question, the solution (5.50) of the continuity equations and the corresponding space-time profiles of observables have to be studied at different quench parameters. Fig. 5.1 reports the spatial profiles of the density $d^{(r)}(\zeta)$ of the first and second particle species at generic quench parameters.

Similarly to the XXZ model [31, 106], the density profiles should have non-analyticities at certain rays $\zeta_n^\pm$, which correspond to the fastest-moving modes of different bound states and species. In the Yang–Gaudin model, these rays correspond to different bound states of spins, and they are computed as

$$\begin{aligned} \zeta_n^- &= \min\left[v_{n,\zeta_n^-}^{(2)}(\lambda)\right], \\ \zeta_n^+ &= \max\left[v_{n,\zeta_n^+}^{(2)}(\lambda)\right]. \end{aligned} \tag{5.52}$$

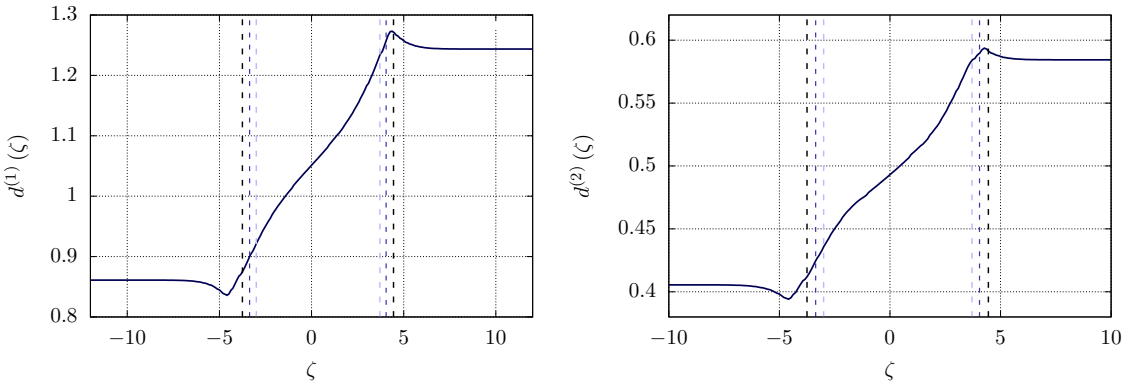

Figure 5.1: Density of different particle species as a function of $\zeta = x/t$. Vertical lines indicate the non-analyticities of the density profiles at $\zeta_n^{\pm}$ (5.52), which correspond to the fastest-moving modes of different spin bound states. (Figure taken from [109].)

The rays corresponding to the spin bound states with $n = 1, 2, 3$ spins are shown as vertical lines in Fig. 5.1. As expected, the unbound state $n = 1$ has the highest maximal velocity, and the maximal velocity diminishes with n. However, the expected non-analyticities at the corresponding rays are difficult to observe. We checked that the occupation number of the maximal velocity modes is very small, and this explains why the non-analyticities are not visible in the profiles.

The velocity function $v_\zeta^{(1)}(\lambda)$ of the first species has no maximum or minimum as it tends to $\pm\infty$ at $\lambda \to \pm\infty$. Therefore the first species does not give rise to a non-analyticity in the spatial profiles of observables. An effective maximal velocity can be defined as the ray $\zeta^{\pm}$ where the spatial profiles of observables start to deviate from their constant values at $\zeta = \pm\infty$.

At general temperatures, the nested structure is not apparent in the profiles of observables. Naively, one could expect that the density of species 2, $d^{(2)}(\zeta)$, would evolve independently from species 1. However, as it is apparent from the density profile in Fig. 5.1, this is not the case. Even for $\zeta < \zeta_1^-$, $d^{(2)}(\zeta)$ is not constant. This means that even before the non-analyticity associated to the maximum velocity of species 2 arrives $d^{(2)}(\zeta)$ starts changing. This is due to the fact that the root densities $\rho^{(1)_\zeta(\lambda)}$ and $\rho_{n,\zeta}^{(2)}(\lambda)$ of the two species are coupled by the BGT equations (5.21)–(5.22). So a change in $\rho_\zeta^{(1)}(\lambda)$ causes a change in $\rho_\zeta^{(2)}(\lambda)$ as well. Thus at generic temperatures the profiles are not qualitatively different from those appearing in the hydrodynamics of the XXZ model [31, 106]. Therefore the nested structure of the Bethe ansatz is not apparent in the hydrodynamics of the system at general temperatures.

5.3 Spin–charge separation in the low-temperature expansion of GHD

We have seen that at general temperatures it is not possible to detect the nested structure of the Bethe ansatz in the Generalized Hydrodynamics of the Yang–Gaudin model because of the existence of bound states of spins. The effects of the bound states are indistinguishable from the effects caused by the existence of spin and charge degrees of freedom. However, these bound states are absent at low temperatures, so it is reasonable to expect detectable spin–charge separation effects in the low-temperature expansion.

In the following, we show the low temperature expansion of the GHD of the Yang–Gaudin model. First we summarize the equations describing the ground state and the low-temperature expansion in the homogeneous system, to the lowest non-trivial order. The final results for this homogeneous expansion were first reported in [220]. However, we write the expansion in such a way that makes it easier to generalize to the inhomogeneous case. Then we show the low-temperature expansion of charge density and current profiles in the inhomogeneous case, and see that the result can be interpreted as a spin–charge separation effect.

5.3.1 The ground state

We start by summarising Takahashi's procedure to obtain the description of the ground state of the model [219]. In the ground state, the occupation number of a mode is

$$\begin{aligned}\vartheta_0^{(1)}(\lambda) &\equiv \lim_{T\to 0}\frac{1}{1+e^{\varepsilon^{(1)}(\lambda)/T}} = \Theta_{\mathrm{H}}(-\varepsilon_0^{(1)}(\lambda)),\\ \vartheta_{n,0}^{(2)}(\lambda) &\equiv \lim_{T\to 0}\frac{1}{1+e^{\varepsilon_n^{(2)}(\lambda)/T}} = \Theta_{\mathrm{H}}(-\varepsilon_{n,0}^{(2)}(\lambda)).\end{aligned} \tag{5.53}$$

This means that the occupation number is one if the corresponding pseudoenergy is negative and zero otherwise. As a consequence, bound states are absent from the ground state, since by (5.36) their pseudoenergies are always positive. In the following, we will drop the lower index n pertaining to bound states from our notation.

The ground state pseudoenergies appearing in (5.53) can be obtained from the $T\to 0$ limit of the saddle-point equations (5.32)–(5.33), which reads [219]

$$\varepsilon_0^{(1)}(\lambda) = \lambda^2 - h - A + a_1 * \varepsilon_0^{(2)}(\lambda)\Big|_2, \tag{5.54}$$

$$\varepsilon_0^{(2)}(\lambda) = 2h + a_1 * \varepsilon_0^{(1)}(\lambda)\Big|_1 - a_2 * \varepsilon_0^{(2)}(\lambda)\Big|_2, \tag{5.55}$$

where we introduced the notation for convolutions

$$f * g(\lambda)\Big|_r \equiv \int_{-B^{(r)}}^{B^{(r)}} \mathrm{d}\mu\, f(\lambda-\mu)g(\mu)\,. \tag{5.56}$$

In writing (5.54)-(5.55) we used that $\varepsilon_{1,0}^{(r)}(\lambda)$ are monotonic functions of λ^2 (see Fig. 5.2 for an illustration and the Appendix of [219] for a proof). The intervals

$[-B^{(r)}, B^{(r)}]$ are the intervals in which $\varepsilon^{(r)}_{1,0}(\lambda)$ are negative. In other words, the rapidities $B^{(r)}$ are the "Fermi rapidities" bounding the Fermi sea at zero temperature.

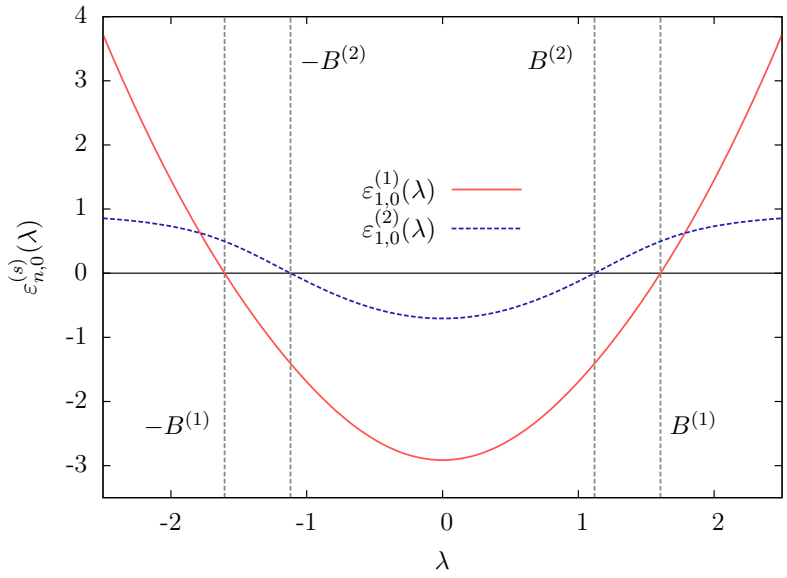

Figure 5.2: Ground-state pseudoenergies (5.54)–(5.55) at $c = 1$, $h = 0.5$, and $A = 2$. The values $B^{(1)}$ and $B^{(2)}$, corresponding to the Fermi rapidities, are highlighted with vertical dotted lines. Note that the pseudoenergies are monotonous in λ^2. (Figure taken from [109].)

The equations (5.54)–(5.55) can be used to determine the ground state phase diagram of the system, which we report in Fig. 5.3. The main features of the diagram are as follows. At zero magnetic field $B^{(2)} = \infty$ and the magnetisation is zero. Increasing the magnetic field $B^{(2)}$ becomes finite and the magnetisation increases. There is a critical magnetic field $h_{\rm crit}(A)$ above which $B^{(2)} = 0$ and the ground state becomes fully polarised. Since $\varepsilon^{(2)}_{1,0}(\lambda)$ has its global minimum in zero, this critical field is found by imposing $\varepsilon^{(2)}_{1,0}(0) = 0$, which yields [220]

$$0 = 2h_{\rm crit} + \frac{1}{2\pi}\left[2c\sqrt{A+h_{\rm crit}} - \left(4A + c^2 + 4h_{\rm crit}\right) \times \arctan\left(\frac{2\sqrt{A+h_{\rm crit}}}{c}\right)\right]. \tag{5.57}$$

The critical line $h_{\rm crit}(A)$ implicitly defined here is shown in the phase diagram of Fig. 5.3. In the following we will be interested in the partially polarized phase $0 < h < h_{\rm crit}$.

Let us now take the zero temperature limit of the BGT equations (5.21)–(5.22), which determine the root densities. Since $\vartheta^{(2)}_{n,0}(\lambda)$ is 0 for $n \geq 2$, we only have to consider non-bound particles. By using (5.53), the $T \to 0$ limit of (5.21)–(5.22) is

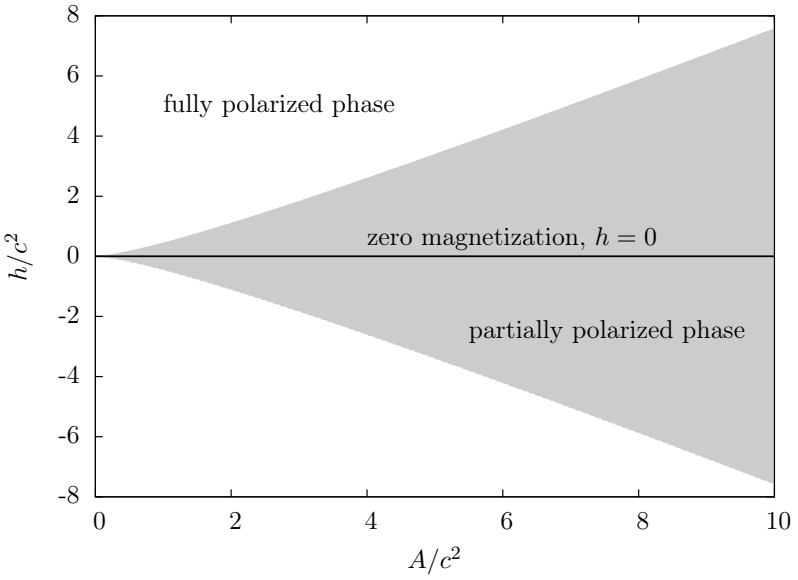

Figure 5.3: Ground-state phase diagram of the repulsive Yang–Gaudin model. The critical line between the partially and fully polarised phase is given by (5.57). (Figure taken from [109].)

obtained as [219]

$$\rho^{(1)}_{\mathrm{t},0}(\lambda) = \frac{1}{2\pi} + a_1 * \rho^{(2)}_{\mathrm{t},0}(\lambda)\Big|_2 , \tag{5.58}$$

$$\rho^{(2)}_{\mathrm{t},0}(\lambda) = a_1 * \rho^{(1)}_{\mathrm{t},0}(\lambda)\Big|_1 - a_2 * \rho^{(2)}_{\mathrm{t},0}(\lambda)\Big|_2 , \tag{5.59}$$

where we have dropped lower indices indicating bound states. Proceeding analogously we find the following expression for the zero temperature limit of (5.42)-(5.43) [219]

$$\rho^{(1)}_{\mathrm{t},0} v^{(1)}_0(\lambda) = \frac{\lambda}{\pi} + a_1 * \rho^{(2)}_{\mathrm{t},0} v^{(2)}_0(\lambda)\Big|_1, \tag{5.60}$$

$$\rho^{(2)}_{\mathrm{t},0} v^{(2)}_{1,0}(\lambda) = a_1 * \rho^{(1)}_{\mathrm{t},0} v^{(1)}_0(\lambda)\Big|_1 - a_2 * \rho^{(2)}_{\mathrm{t},0} v^{(2)}_0(\lambda)\Big|_2. \tag{5.61}$$

Note that the above equations imply $\rho^{(r)}_{\mathrm{t},0}(-\lambda) = \rho^{(r)}_{\mathrm{t},0}(\lambda)$ while $v^{(r)}_0(-\lambda) = -v^{(r)}_0(\lambda)$.

The ground state expectation values of charges and currents are found by plugging the solutions of (5.58)-(5.61) into (5.26)-(5.28) for the charges and into (5.44)–(5.46) for the currents. In particular

$$j_n[\boldsymbol{\rho}_0] = 0, \quad j_m[\boldsymbol{\rho}_0] = 0, \quad j_e[\boldsymbol{\rho}_0] = 0, \tag{5.62}$$

because the integrand in (5.44)–(5.46) is odd in λ. This can be understood by considering the parity operator

$$\mathcal{P}\Psi(x) = \Psi(-x). \tag{5.63}$$

The even charges, satisfying $\mathcal{P}Q = Q$, have odd currents, which satisfy $\mathcal{P}J = -J$. The thermal expectation value of odd currents is always zero because the Hamiltonian (5.1) is even. Since we have obtained the ground state properties by taking the limit $T \to 0$ of the thermodynamics, this property continues to hold in the ground state as well.

5.3.2 Low-temperature expansion of equilibrium thermodynamics

Let us now compute the first nonzero correction to the thermodynamics of the equilibrium model. We will compute quantities of the type

$$\delta f(\lambda) = f_T(\lambda) - f_0(\lambda)\,, \tag{5.64}$$

i.e., the difference between the finite-T and the ground-state value of functions in the thermodynamic Bethe ansatz. First we compute the pseudoenergy correction $\delta\varepsilon_T^{(r)}(\lambda)$, then the correction to the total densities $\delta\rho_{t,T}^{(r)}(\lambda)$ and the velocities $\delta\rho_{t,T}^{(r)}(\lambda)v_T^{(r)}(\lambda)$. Finally, we give the expression for the correction to the energy density δe. All of these corrections are second order in T.

The pseudo-Fermi-factors (5.53) show that the modes with $\varepsilon_{m,T}^{(n)}(\lambda) > 0$ are still exponentially suppressed at small but finite T. Therefore we can describe the state using only the thermal dressed energies $\varepsilon_{1,T}^{(r)}(\lambda)$: the bound states of the particles of the second species have positive pseudoenergy, therefore they can be neglected from the integral equations. In the following, we will suppress the lower index n for bound states.

We find the leading finite-T corrections $\delta\varepsilon_T^{(n)}(\lambda)$ by following the method of Refs. [107, 221]. The result, whose derivation is reported in Appendix 5.A.1, reads as

$$\delta\varepsilon_T^{(1)}(\lambda) = \frac{\pi^2 T^2}{6\,\varepsilon_0^{(2)\prime}(B^{(2)})} U^{(1)}(\lambda) + O(T^4), \tag{5.65}$$

$$\delta\varepsilon_T^{(2)}(\lambda) = \frac{\pi^2 T^2}{6\,\varepsilon_0^{(2)\prime}(B^{(2)})} U^{(2)}(\lambda) + O(T^4), \tag{5.66}$$

where the functions $U^{(r)}(\lambda)$ satisfy the linear system

$$U^{(1)}(\lambda) = d_U^{(1)}(\lambda) + a_1 * U^{(2)}(\lambda)\Big|_2, \tag{5.67}$$

$$U^{(2)}(\lambda) = d_U^{(2)}(\lambda) + a_1 * U^{(1)}(\lambda)\Big|_1 - a_2 * U^{(2)}(\lambda)\Big|_2\,. \tag{5.68}$$

This system of equations is independent of T, and it depends only on the parameters c, h A of the Hamiltonian (5.1). The driving functions appearing here can be written in the convenient form

$$d_U^{(1)}(\lambda) = a_1 * z_U^{(2)}(\lambda)\Big|_2, \tag{5.69}$$

$$d_U^{(2)}(\lambda) = a_1 * z_U^{(1)}(\lambda)\Big|_1 - a_2 * z_U^{(2)}(\lambda)\Big|_2, \tag{5.70}$$

where we introduced

$$z_U^{(r)}(\lambda) \equiv \sum_{\sigma=\pm} z_{U,\sigma}^{(r)}(\lambda)\,, \tag{5.71}$$

and finally

$$z_{U,\sigma}^{(r)}(\lambda) \equiv z^{(r)}(C_{U,\sigma}^{(r)}, D_{U,\sigma}^{(r)}, \lambda) = C_{U,\sigma}^{(r)}\delta(\lambda - \sigma B^{(r)-}) + D_{U,\sigma}^{(r)}\delta'(\lambda - \sigma B^{(r)-})\,. \tag{5.72}$$

Here $\delta(x)$ and $\delta'(x)$ are respectively the Dirac delta and its first derivative. The infinitesimal shift in the Fermi rapidity $B^{(r)-} = B^{(r)}e^{-\epsilon}$ ensures that the Dirac deltas of (5.72) are picked up the by the convolution integrals in (5.69)–(5.70). The constants in (5.72) are given by $C_{U,\sigma}^{(2)} = -1$, $C_{U,\sigma}^{(1)} = \varepsilon_0^{(2)\prime}(B^{(2)})/\varepsilon_0^{(1)\prime}(B^{(1)})$, and $D_{U,\sigma}^{(r)} = 0$.

Let us now sketch how to find the correction to the total root densities whose full derivation is relegated to Appendix 5.A.2. Neglecting the contribution of bound states, we can rewrite (5.21)-(5.22) on a thermal state as follows

$$\rho_{\mathrm{t},T}^{(1)}(\lambda) = \frac{1}{2\pi} + a_1 \star \vartheta_T^{(2)}\rho_{\mathrm{t},T}^{(2)}(\lambda), \tag{5.73}$$

$$\rho_{\mathrm{t},T}^{(2)}(\lambda) = a_1 \star \vartheta_T^{(1)}\rho_{\mathrm{t},T}^{(1)}(\lambda) - a_2 \star \vartheta_T^{(2)}\rho_{\mathrm{t},T}^{(2)}(\lambda), \tag{5.74}$$

where the sign $\star$ denotes the convolution (5.23) introduced in the finite-temperature thermodynamics. The system (5.73)–(5.74) features many Sommerfeld-like integrals of the form

$$I_f^{(r)} = \int_{-\infty}^{\infty} \mathrm{d}\lambda\ \ \vartheta_T^{(r)}(\lambda) f(\lambda) \tag{5.75}$$

with appropriate functions $f(\lambda)$. The expansion of such integrals is carried out in Appendix A of Ref. [107], where the expansion is carried out in the gapless phase of the XXZ spin-1/2 chain but it applies to all TBA-solvable models where $\varepsilon_0^{(r)}(\lambda)$ has two symmetric zeros) and reads as

$$I_f^{(r)} = \int_{-B^{(r)}}^{B^{(r)}} \mathrm{d}\lambda\ \left[1 + \frac{\pi^2 T^2}{6} z_I^{(r)}(\lambda)\right] f(\lambda) + O(T^4)\,. \tag{5.76}$$

Here $z_I^{(r)}(\lambda)$ has the form similar to (5.71)-(5.72)

$$z_I^{(r)}(\lambda) \equiv \sum_{\sigma=\pm} z_{I,\sigma}^{(r)}(\lambda)\,, \tag{5.77}$$

$$z_{I,\sigma}^{(r)}(\lambda) \equiv z^{(r)}(C_{I,\sigma}^{(r)}, D_{I,\sigma}^{(r)}, \lambda) = C_{I,\sigma}^{(r)}\delta(\lambda - \sigma B^{(r)-}) + D_{I,\sigma}^{(r)}\delta'(\lambda - \sigma B^{(r)-})\,. \tag{5.78}$$

with the coefficients being

$$D_{I,\sigma}^{(r)} = \frac{-\sigma}{(\varepsilon_0^{(r)\prime}(B^{(r)}))^2}, \tag{5.79}$$

$$\frac{C_{I,\sigma}^{(2)}}{D_{I,+}^{(2)}} = \left[\frac{\varepsilon_0^{(2)\prime\prime}(B^{(2)})}{\varepsilon_0^{(2)\prime}(B^{(2)})} + U^{(2)}(B^{(2)})\right], \tag{5.80}$$

$$\frac{C_{I,\sigma}^{(1)}}{D_{I,+}^{(1)}} = \left[\frac{\varepsilon_0^{(1)\prime\prime}(B^{(1)})}{\varepsilon_0^{(1)\prime}(B^{(1)})} + \tilde{U}^{(1)}(B^{(1)})\right], \tag{5.81}$$

where we introduced

$$\tilde{U}^{(1)}(B^{(1)}) = U^{(1)}(B^{(1)})\frac{\varepsilon_0^{(1)\prime}(B^{(1)})}{\varepsilon_0^{(2)\prime}(B^{(2)})}\,. \tag{5.82}$$

Using the expansion (5.76)–(5.82) we can turn (5.73)-(5.74) into a set of linear integral equations for the corrections to the total root densities. At the leading order in T we find

$$\delta\rho^{(1)}_{\mathrm{t},T}(\lambda) = \frac{\pi^2 T^2}{6}R^{(1)}(\lambda) + O(T^4), \tag{5.83}$$

$$\delta\rho^{(2)}_{\mathrm{t},T}(\lambda) = \frac{\pi^2 T^2}{6}R^{(2)}(\lambda) + O(T^4), \tag{5.84}$$

where $R^{(r)}(\lambda)$ fulfil the system (5.67)-(5.68) with drivings $d_R^{(r)}(\lambda)$. The drivings are given by (5.69)-(5.70), where $z_U^{(r)}(\lambda)$ is replaced by $z_{R,I}^{(r)}(\lambda)$ of the form (5.71)-(5.72) and coefficients

$$D^{(r)}_{R,\sigma} = -\sigma\frac{\rho^{(r)}_{\mathrm{t},0}(B^{(r)})}{(\varepsilon_0^{(r)\prime}(B^{(r)}))^2}, \tag{5.85}$$

$$\frac{C^{(2)}_{R,\sigma}}{D^{(2)}_{R,-}} = \left[\frac{\rho_0^{(2)\prime}(B^{(2)})}{\rho^{(2)}_{\mathrm{t},0}(B^{(2)})} - \frac{\varepsilon_0^{(2)\prime\prime}(B^{(2)})}{\varepsilon_0^{(2)\prime}(B^{(2)})} - U^{(2)}(B^{(2)})\right], \tag{5.86}$$

$$\frac{C^{(1)}_{R,\sigma}}{D^{(1)}_{R,-}} = \left[\frac{\rho_0^{(1)\prime}(B^{(1)})}{\rho^{(1)}_{\mathrm{t},0}(B^{(1)})} - \frac{\varepsilon_0^{(1)\prime\prime}(B^{(1)})}{\varepsilon_0^{(1)\prime}(B^{(1)})} - \tilde{U}^{(1)}(B^{(1)})\right]. \tag{5.87}$$

Similarly to $U^{(r)}(\lambda)$, $R^{(r)}(\lambda)$ is independent of the temperature and depends only on the parameters of the Hamiltonian.

The expansion of the velocities (5.42)–(5.43) is similar to the above. First, the bound states can be neglected, resulting in

$$\rho^{(1)}_{\mathrm{t},T}v^{(1)}_T(\lambda) = \frac{\lambda}{\pi} + a_1 \star \vartheta^{(2)}_T\rho^{(2)}_{\mathrm{t},T}v^{(2)}_T(\lambda), \tag{5.88}$$

$$\rho^{(2)}_{\mathrm{t},T}v^{(2)}_T(\lambda) = a_1 \star \vartheta^{(1)}_T\rho^{(1)}_{\mathrm{t},T}v^{(1)}_T(\lambda) - a_2 \star \vartheta^{(2)}_T\rho^{(2)}_{\mathrm{t},T}v^{(2)}_T(\lambda). \tag{5.89}$$

Then using the expansion (5.76)–(5.82) for the convolutions of (5.88)–(5.89) we obtain

$$\delta\rho^{(1)}_{\mathrm{t},T}v^{(1)}_T(\lambda) = \frac{\pi T^2}{6}W^{(1)}(\lambda) + O(T^4), \tag{5.90}$$

$$\delta\rho^{(2)}_{\mathrm{t},T}v^{(2)}_T(\lambda) = \frac{\pi T^2}{6}W^{(2)}(\lambda) + O(T^4). \tag{5.91}$$

The functions $W^{(r)}(\lambda)$ fulfil the system (5.67)-(5.68) with drivings $d_W^{(r)}(\lambda)$ again given by (5.69)-(5.70). This time the function $z_U^{(r)}(\lambda)$ is replaced by $z_{W,I}^{(r)}(\lambda)$ of the

form (5.71)-(5.72) and coefficients

$$D^{(r)}_{W,\sigma} = \frac{-1}{\varepsilon_0^{(r)\prime}(B^{(r)})}, \tag{5.92}$$

$$\frac{C^{(2)}_{W,\sigma}}{D^{(2)}_{W,-}} = \sigma U^{(2)}(B^{(2)}), \tag{5.93}$$

$$\frac{C^{(1)}_{W,\sigma}}{D^{(1)}_{W,-}} = \sigma \tilde{U}^{(1)}(B^{(2)}). \tag{5.94}$$

We see that the driving functions $d^{(r)}_W(\lambda)$ are odd, implying that also the functions $W^{(r)}(\lambda)$ are odd.

Using these expressions we can finally write the first non-trivial corrections to the charge densities at finite temperature. First let us consider a generic charge of the form (5.39). Neglecting exponentially small corrections in $1/T$ coming from the bound states, we have

$$\delta q = \sum_{r=1,2} \int_{-\infty}^{\infty} \mathrm{d}\lambda\, \rho^{(r)}_{\mathrm{t},T}(\lambda)\vartheta^{(r)}(\lambda)q^{(r)}(\lambda) + O(e^{-C_q/T}). \tag{5.95}$$

Using the expansion (5.75)–(5.76) and the expressions (5.83)-(5.84) in (5.95), we have

$$\begin{aligned}\delta q &= \sum_{r=1,2} \int_{-\infty}^{\infty} \mathrm{d}\lambda\, (R^{(r)}(\lambda) + z^{(r)}_{R,I}(\lambda))q^{(r)}(\lambda) + O(T^4) \\ &= \sum_{r=1,2}\sum_{\sigma=\pm} \left\{C^{(r)}_{R,\sigma} f^{(r)}_q(\sigma B^{(r)}) - D^{(r)}_{R,\sigma} f^{(r)\prime}_q(\sigma B^{(r)})\right\} + O(T^4),\end{aligned} \tag{5.96}$$

where the functions $f^{(r)}_q(\lambda)$ fulfil

$$f^{(1)}_q(\lambda) = q^{(1)}(\lambda) + a_1 * f^{(2)}_q(\lambda)\Big|_2, \tag{5.97}$$

$$f^{(2)}_q(\lambda) = q^{(2)}(\lambda) + a_1 * f^{(1)}_q(\lambda)\Big|_1 - a_2 * f^{(2)}_q(\lambda)\Big|_2. \tag{5.98}$$

The second line of (5.96) is proven by inverting the integral system (5.67)–(5.68) for $R^{(r)}(\lambda)$, which is shown in Appendix 5.A.3. As a particular case of (5.96), let us consider the first finite-temperature correction to the energy density

$$\delta e = \int_{-\infty}^{\infty} \mathrm{d}\lambda\, \left[\delta\rho^{(1)}_T(\lambda)\, e(\lambda) + 2h\delta\rho^{(2)}_T(\lambda)\right] + O(e^{-C_e/T}). \tag{5.99}$$

Using the expansion (5.96), we have

$$\begin{aligned}\delta e &= \frac{\pi^2 T^2}{6} \sum_{r=1,2}\sum_{\sigma=\pm} \left\{C^{(r)}_{R,\sigma} f^{(r)}_q(\sigma B^{(r)}) - D^{(r)}_{R,\sigma} f^{(r)\prime}_q(\sigma B^{(r)})\right\} + O(T^4) \\ &= \frac{\pi^2 T^2}{6} \sum_{r=1,2}\sum_{\sigma=\pm} \left\{C^{(r)}_{R,\sigma} \varepsilon^{(r)}_0(\sigma B^{(r)}) - D^{(r)}_{R,\sigma} \varepsilon^{(r)\prime}_0(\sigma B^{(r)})\right\} + O(T^4).\end{aligned} \tag{5.100}$$

In the second line we used the fact that that, for $q^{(1)}(\lambda) = e(\lambda)$ and $q^{(2)}(\lambda) = h$, equations (5.97)-(5.98) coincide with (5.54)-(5.55), and therefore $f_q^{(r)}(\lambda) = \varepsilon_0^{(r)}(\lambda)$. Finally, by substituting the definitions of $C_{R,\sigma}^{(r)}$, $D_{R,\sigma}^{(r)}$ (5.85)–(5.87), we can write

$$\delta e = \frac{\pi^2 T^2}{3} \sum_{r=1,2} \frac{\rho_{\mathrm{t},0}^{(r)}(B^{(r)})}{\varepsilon_0^{(r)\prime}(B^{(r)})} + O(T^4) = \frac{\pi T^2}{6} \sum_{r=1,2} \frac{1}{v_0^{(r)}(B^{(r)})} + O(T^4). \tag{5.101}$$

Here in the last step we used the definition (5.41) of the velocities.

It was reported in [220] that the finite temperature correction (5.101) agrees with that of two independent conformal field theories (CFTs) with central charge equal to one and velocity of light respectively equal to $v_{1,0}^{(1)}(B^{(1)})$ and $v_{1,0}^{(2)}(B^{(2)})$: the "Fermi velocities" of the two components. This is in accordance with the well-known fact that the low energy description of (5.1) is in terms of two decoupled CFTs. In the next Section we take this analysis further to the case of an inhomogeneous system.

Before concluding the analysis of the homogeneous case we note that the corrections to the currents (5.44)–(5.46) are all zero, because $W^{(r)}(\lambda)$ and $d_W^{(r)}(\lambda)$ are both odd. This is in accordance with the fact that the expectation values of the currents of even charges vanish in a thermal state.

5.3.3 Low-temperature expansion of GHD far from the light-cones

Let us now consider the low-temperature expansion of the GHD after a bipartite quench. More precisely, we take the initial state (5.2) with

$$T_{\mathrm{L}} \equiv T, \quad T_{\mathrm{R}} = \mathfrak{r}T, \tag{5.102}$$

and expand for small T (with $A_R = h_R = 0$, $A_L = h_L = 0$). At $T = 0$, we trivially find that the system is globally in the ground state described in Section 5.3.1, and specifically the currents (5.44)–(5.46) are all zero.

To find the first finite temperature corrections we use the form of the implicit solution (5.50). Both terms in (5.50) are multiplied by a filling function $\vartheta_{1,T}^{(r)}$ of a homogeneous thermal state. Similarly to the homogeneous case, it follows from (5.53) that bound states of spins have exponentially small filling numbers because their pseudoenergy (5.36) is positive. We can then conclude that all bound states of the spin rapidities can be neglected, as they give exponentially small corrections in T. We are then left to consider reduced systems of integral equations for the string densities

$$\rho_{\mathrm{t},\zeta}^{(1)}(\lambda) = \frac{1}{2\pi} + a_1 \star \vartheta_\zeta^{(2)} \rho_{\mathrm{t},\zeta}^{(2)}(\lambda), \tag{5.103}$$

$$\rho_{\mathrm{t},\zeta}^{(2)}(\lambda) = a_1 \star \vartheta_\zeta^{(1)} \rho_{\mathrm{t},\zeta}^{(1)}(\lambda) - a_2 \star \vartheta_\zeta^{(2)} \rho_{\mathrm{t},\zeta}^{(2)}(\lambda), \tag{5.104}$$

where the lower indices corresponding to bound states are omitted. Similarly, the quasiparticle velocities satisfy

$$\rho^{(1)}_{\mathrm{t},\zeta} v^{(1)}_\zeta(\lambda) = \frac{\lambda}{\pi} + a_1 \star \vartheta^{(2)}_\zeta \rho^{(2)}_{\mathrm{t},\zeta} v^{(2)}_\zeta(\lambda), \tag{5.105}$$

$$\rho^{(2)}_{\mathrm{t},\zeta} v^{(2)}_\zeta(\lambda) = a_1 \star \vartheta^{(1)}_\zeta \rho^{(1)}_{\mathrm{t},\zeta} v^{(1)}_\zeta(\lambda) - a_2 \star \vartheta^{(2)}_\zeta \rho^{(2)}_{\mathrm{t},\zeta} v^{(2)}_\zeta(\lambda). \tag{5.106}$$

In order to find the leading low-temperature correction to the systems (5.103)–(5.105) and (5.105)–(5.106), we need to expand integrals of the form

$$I^{(r)}_{\zeta,f} = \int_{-\infty}^{\infty} \mathrm{d}\lambda\, \vartheta^{(r)}_{1,\zeta}(\lambda) f^{(r)}(\lambda), \tag{5.107}$$

for some appropriate functions $f^{(r)}(\lambda)$. The expansion of (5.107) up to $O(T^3)$ is thoroughly carried out in Appendix A of Ref. [107]; below we discuss the main features. Let us now restrict ourselves to the case where the ray ζ is far from the light-cones associated to the Fermi velocities, i.e.,

$$\lim_{T\to 0} |\zeta - v^{(r)}_0(B^{(r)})| \neq 0. \tag{5.108}$$

In this case, the expansion reads as [107]

$$I^{(r)}_{\zeta,f} = \int_{-B^{(r)}}^{B^{(r)}} \mathrm{d}\lambda\, f^{(r)}(\lambda) \left[1 + \frac{\pi^2 T^2}{6} z^{(r)}_{I,\zeta}(\lambda)\right] + O(T^4)\,, \tag{5.109}$$

where we introduced

$$z^{(r)}_{I,\zeta}(\lambda) = \begin{cases} z^{(r)}_I(\lambda), & \text{if } \zeta < -v^{(r)}_{1,0}(B^{(r)}) \\ z^{(r)}_{I,+}(\lambda) + \mathfrak{r}^2 z^{(r)}_{I,-}(\lambda), & \text{if } -v^{(r)}_0(B^{(r)}) < \zeta < v^{(r)}_0(B^{(r)}) \\ \mathfrak{r}^2 z^{(r)}_I(\lambda) & \text{if } \zeta > v^{(r)}_0(B^{(r)}) \end{cases} \tag{5.110}$$

The functions $z^{(r)}_I$ and $z^{(r)}_{I,\pm}$ are respectively of the form (5.71) and (5.72) and are specified by the coefficients (5.79)–(5.81). In words: far away from the light cone edges, the $O(T^2)$ correction to the integral is piecewise constant in ζ, consisting of three plateaux.

Using the expansion (5.109), it is possible to write linear equations for the first nonzero corrections to $\rho^{(r)}_{\mathrm{t},\zeta}$ and $\rho^{(r)}_{\mathrm{t},\zeta} v^{(r)}_\zeta(\lambda)$ as we did in the previous section for the homogeneous case. Proceeding as in (5.95)–(5.96), these expressions can be used to find the first correction to the profiles of local observables. Since the procedure is very similar to the one outlined in the previous section, we omit it here (it is reported for completeness in Appendix 5.B.1). For a generic even charge, the result up to $O(T^2)$ reads as

$$\delta q(\mathfrak{r},\zeta) = \frac{\pi^2 T^2}{6} \left\{ \sum_{r=1}^{2} \nu^{(r)}(\mathfrak{r},\zeta) \sum_{\sigma=\pm} \left[C^{(r)}_{R,\sigma} f^{(r)}_q(\sigma B^{(r)}) - D^{(r)}_{R,\sigma} f^{(r)\prime}_q(\sigma B^{(r)}) \right] \right\}, \tag{5.111}$$

$$\delta j_q(\mathfrak{r},\zeta) = \frac{\pi^2 T^2}{6} \left\{ \sum_{r=1}^{2} \omega^{(r)}(\mathfrak{r},\zeta) \sum_{\sigma=\pm} \left[C^{(r)}_{W,\sigma} f^{(r)}_q(\sigma B^{(r)}) - D^{(r)}_{W,\sigma} f^{(r)\prime}_q(\sigma B^{(r)}) \right] \right\}, \tag{5.112}$$

where $\nu^{(r)}(\mathfrak{r},\zeta)$ and $\omega^{(r)}(\mathfrak{r},\zeta)$ are piecewise constant functions in ζ

$$\nu^{(r)}(\mathfrak{r},\zeta) \equiv \begin{cases} 1, & \text{if } \zeta < -v_0^{(r)}(B^{(r)}), \\ (\mathfrak{r}^2+1)/2, & \text{if } -v_0^{(r)}(B^{(r)}) < \zeta < v_0^{(r)}(B^{(r)}), \\ \mathfrak{r}^2, & \text{if } \zeta > v_0^{(r)}(B^{(r)}) \end{cases} \tag{5.113}$$

$$\omega^{(r)}(\mathfrak{r},\zeta) \equiv \begin{cases} 0, & \text{if } \zeta < -v_0^{(r)}(B^{(r)}), \\ (1-\mathfrak{r}^2)/2, & \text{if } -v_0^{(r)}(B^{(r)}) < \zeta < v_0^{(r)}(B^{(r)}), \\ 0, & \text{if } \zeta > v_0^{(r)}(B^{(r)}). \end{cases} \tag{5.114}$$

In (5.111)–(5.112) the function $f_q^{(r)}(\lambda)$ is defined via the integral equations (5.97)-(5.98). The coefficients $C_{R,\sigma}^{(r)}, D_{R,\sigma}^{(r)}, C_{W,\sigma}^{(r)}, D_{W,\sigma}^{(r)}$ are defined in (5.85)–(5.87) and (5.92)–(5.94). Note that the charge density expression (5.111) is similar to the homogeneous case (5.96), the only difference being the appearance of the profile function $\nu^{(r)}(\mathfrak{r},\zeta)$. The profile function $\omega^{(r)}(\mathfrak{r},\zeta)$ corresponding to the current density (5.112) is zero outside the light cone associated to the Fermi velocity. This is in accordance with the fact that the thermal expectation values of the currents of even charges is zero.

As an application of the expansion (5.111)–(5.112), let us focus on the profiles of the energy density (5.28) and energy current density (5.46). In this case we have $f_q^{(r)}(\lambda) = \varepsilon_{1,0}^{(r)}(\lambda)$. Plugging this in (5.111)-(5.112) we see that the leading contribution to the profiles reads as

$$e(\zeta,\mathfrak{r}) = e_0 + \frac{\pi T^2}{6}\sum_{r=1}^{2}\frac{\nu^{(r)}(\mathfrak{r},\zeta)}{v_{1,0}^{(r)}(B^{(r)})}, \tag{5.115}$$

$$j_e(\zeta,\mathfrak{r}) = \frac{\pi T^2}{6}\sum_{r=1}^{2}\omega^{(r)}(\mathfrak{r},\zeta). \tag{5.116}$$

This result is compared with the numerical solution of the generalised hydrodynamic equations in the left panels of Figs. 5.4 and 5.5. It is of interest to write down explicitly these functions for $\zeta = 0$, which corresponds to the celebrated non-equilibrium steady state (NESS)

$$e(0,\mathfrak{r}) - e_0 = \frac{\pi(T_{\mathrm{L}}^2+T_{\mathrm{R}}^2)}{12}\sum_{r=1}^{2}\frac{1}{v_{1,0}^{(r)}(B^{(r)})}, \tag{5.117}$$

$$j_e(0,\mathfrak{r}) = \frac{\pi(T_{\mathrm{L}}^2-T_{\mathrm{R}}^2)}{6}\,. \tag{5.118}$$

We note that the dependence on the temperatures of the two halves is the one expected from the CFT analysis of the bipartition protocol [222, 223]: the results correspond to the sum of two CFTs with central charge equal to 1.

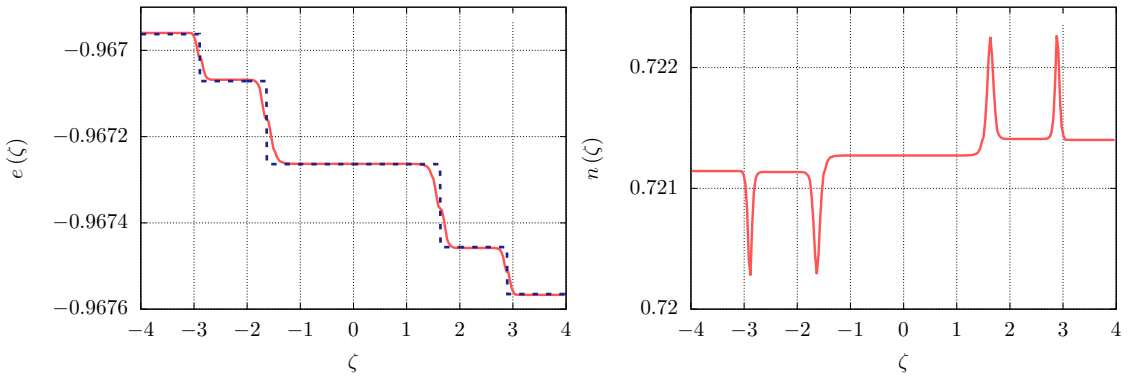

Figure 5.4: Profiles of energy (Left) and particle (Right) densities as a function of the ray $\zeta = x/t$ at infinite times after a quench from the bipartite state. Full lines are obtained as a numerical solution of Eq. (5.49) while dashed lines are the result of the analytical low-temperature expansion (5.115)-(5.116). The Hamiltonian has $c = 1$, while the parameters of the initial state (5.102) are $\beta_{\rm L} = 25$ and $\beta_{\rm R} = 50$ (with $A_R = h_R = 0$, $A_L = h_L = 0$). (Figure taken from [109].)

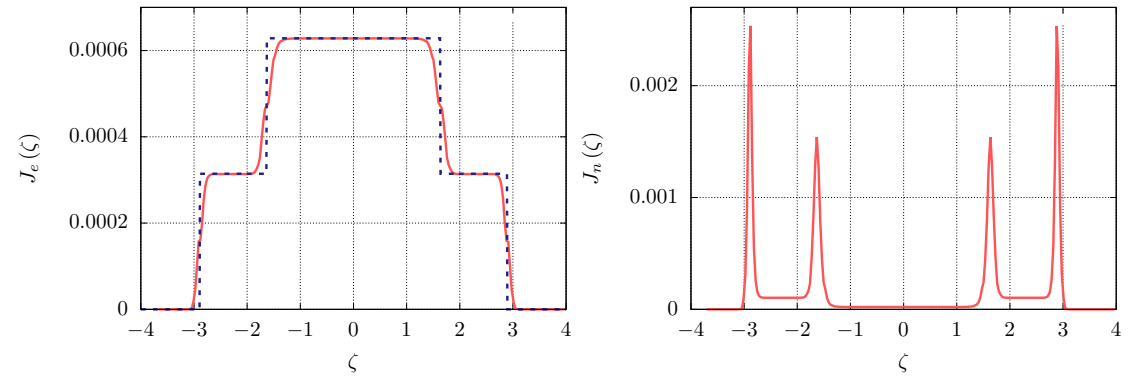

Figure 5.5: Profiles of energy (Left) and particle (Right) currents as a function of the ray $\zeta = x/t$ at infinite times after a quench from the bipartite state. Full lines are obtained as a numerical solution of Eq. (5.49) while dashed lines are the result of the analytical low-temperature expansion (5.115)-(5.116). The Hamiltonian has $c = 1$, while the parameters of the initial state (5.102) are $\beta_{\rm L} = 25$ and $\beta_{\rm R} = 50$ (with $A_R = h_R = 0$, $A_L = h_L = 0$). (Figure taken from [109].)

5.3.4 Low-temperature expansion of GHD near the light-cones

Now let us consider the low-temperature expansion of the hydrodynamics in the region

$$\lim_{T\to 0} |\zeta - v_0^{(r)}(B^{(r)})| = O(T), \tag{5.119}$$

i.e., in the vicinity of the light cones associated to the Fermi velocities. In this region, the expansion of integrals (5.107) is [107]

$$I^{(r)}_{\zeta,f} = \int_{-B^{(r)}}^{B^{(r)}} \mathrm{d}\lambda\ f^{(r)}(\lambda)\left[1 + \frac{\pi^2 T(1-\mathfrak{r}^2)}{6} z^{(r)}_{II}(\lambda,\zeta)\right] + O(T^2)\,, \tag{5.120}$$

where

$$z^{(r)}_{II}(\lambda,\zeta) = \sum_{\sigma=\pm} z^{(r)}_{II,\sigma}(\lambda)\mathcal{D}_{\mathfrak{r}}\left[\frac{\zeta - \sigma v^{(r)}_{1,0}(B^{(r)})}{v^{(r)}_{1,0}(B^{(r)}))T|m^{(r)}_*|^{-1}}\right]. \tag{5.121}$$

In (5.120) the effective mass is introduced as

$$m^{(r)}_* = \frac{\partial^2 \varepsilon^{(r)\prime}_{1,0}(\lambda)}{\partial p^{(r)}_{1,T}(\lambda)^2}\Big|_{\lambda=B^{(r)}} = \frac{\varepsilon^{(r)\prime}_{1,0}(B^{(r)}) v^{(r)}_{1,0}(B^{(r)})}{v^{(r)\prime}_{1,0}(B^{(r)})}\,, \tag{5.122}$$

where $p^{(r)}_{n,T}(\lambda)$ is the dressed momentum appearing in (5.41). The shape function $\mathcal{D}_{\mathfrak{r}}(z)$ is

$$\mathcal{D}_{\mathfrak{r}}[z] \equiv \frac{6\log(1+e^z)}{\pi^2(1-\mathfrak{r}^2)} - \frac{6\mathfrak{r}\log(1+e^{z/\mathfrak{r}})}{\pi^2(1-\mathfrak{r}^2)}\,. \tag{5.123}$$

This function is positive and peaked around $z=0$, in particular we have

$$\lim_{T\to 0^+} \frac{1}{T}\mathcal{D}_{\mathfrak{r}}[z/T] = \delta(z)\,. \tag{5.124}$$

In (5.120) the functions $z^{(r)}_{II,\sigma}(\lambda)$ are of the form (5.72) with coefficients

$$C^{(r)}_{II,\sigma} = \sigma\,\mathrm{sgn}(v_1^{0\prime}(B^{(r)}))/\varepsilon_1'(B^{(r)}), \qquad D^{(r)}_{II,\sigma} = 0. \tag{5.125}$$

We see that in the region (5.119) the first correction to the integral (5.107) is $O(T)$. As a function of ζ it has a peaked form described by the function $\mathcal{D}_{\mathfrak{r}}[z]$.

Using the above expansion, one can derive the profiles of conserved charge and current densities in the region (5.119). The profiles, whose derivation is reported in Appendix 5.B.2, read up to $O(T)$ as

$$q(\mathfrak{r},\zeta) = \sum_{r=1}^{2}\sum_{\sigma=\pm} \sigma \frac{\pi T \mathrm{sgn}(v^{(r)\prime}_{1,0}(B^{(r)}))}{12 v^{(r)}_{1,0}(B^{(r)})}(1-\mathfrak{r}^2) f_q(B^{(r)})\mathcal{D}_{\mathfrak{r}}\left[\frac{\zeta - \sigma v^{(r)}_{1,0}(B^{(r)})}{v^{(r)}_{1,0}(B^{(r)}))T|m^{(r)}_*|^{-1}}\right], \tag{5.126}$$

$$j_q(\mathfrak{r},\zeta) = \sum_{r=1}^{2}\sum_{\sigma=\pm} \frac{\pi T \mathrm{sgn}(v^{(r)\prime}_{1,0}(B^{(r)}))}{12}(1-\mathfrak{r}^2) f_q(B^{(r)})\mathcal{D}_{\mathfrak{r}}\left[\frac{\zeta - \sigma v^{(r)}_{1,0}(B^{(r)})}{v^{(r)}_{1,0}(B^{(r)}))T|m^{(r)}_*|^{-1}}\right], \tag{5.127}$$

in which $f_q^{(r)}(B^{(r)})$ are the dressed charges (5.97)–(5.98). In particular, for the energy density

$$f_e^{(r)}(B^{(r)}) = \varepsilon_0^{(r)}(B^{(r)}) = 0, \tag{5.128}$$

so the peaks described by (5.126)–(5.127) are absent from the spatial profiles. This absence can be seen in the numerical solutions presented in the left panels of Fig. 5.4 for the energy density, and in Fig. 5.5 for the energy current density. In the case of the particle density (5.26) and particle current density (5.44), the peaks can be observed in the numerical solution, presented in the right panels of Figs. 5.4 and 5.5.

5.4 Discussion

Before concluding this Chapter, let us summarize and discuss our results. Our aim was to see whether the multi-species particle content and the nested structure of the Yang–Gaudin model was apparent in its hydrodynamics. In order to see this, we generalized the GHD framework to the Yang–Gaudin model and solved the GHD equations numerically at different temperatures. We have seen that at high temperatures the spatial profiles of observables is indistinguishable from a system having a non-nested structure with bound states. However, by carrying out a low-temperature expansion we have detected the signs of a nested structure and spin–charge separation effects.

The form of the low-temperature profiles (5.111)-(5.112) and (5.126)-(5.127) can be reproduced by considering two decoupled *non-linear* Luttinger liquids in the spirit of Ref. [108]. In particular, in the bulk region (5.108) the structure is that given by two decoupled *linear* Luttinger liquids, namely two decoupled CFTs. Each of the CFTs is described separately by the theory of non–equilibrium CFT [222, 223]. The resulting profiles are piecewise constant functions of ζ, and change value every time that the absolute value of the ray equals one of the two Fermi velocities $v_{1,0}^{(r)}(B^{(r)})$. This generically results in a five step form, as it can be seen from Figs. 5.4 and 5.5.

In the region (5.119), which is the transition region between two plateaux, the non-linearity of the dispersion relations (quantified by $1/m^{(r)}$ (5.122)) becomes relevant [108]: the profiles have a peaked form determined by the function $\mathcal{D}_{\mathfrak{r}}[z]$ (5.123). Note that the width of the peak around $\zeta = v_{1,0}^{(r)}(B^{(r)})$ depends on the species r. This form of the profiles was first described in [108] for a single Luttinger liquid, where it was shown to be a remarkable example of *universality* beyond the linear Luttinger approximation [224]. The calculations presented in this Chapter give a non-trivial test of the validity of this prediction in the case of interacting nested systems.

The peculiar structure of the profiles described above, five steps with peaks in correspondence of the transitions, gives an indication of a spin-charge separation. Indeed, observing profiles with this structure one can argue that they are produced by two decoupled non-linear Luttinger liquids. Note, however, that the local observables couple the two theories: it is impossible to find an observable sensitive to

a single Luttinger liquid only. This means that one cannot determine the physical content of the two separated degrees of freedom and distinguish them by looking at the profiles: the signature of spin-charge separation that one can obtain from the profiles is only an indirect one. Still, these are qualitatively different from the profiles that one would obtain in the low-temperature regime of non-nested systems, such as the XXZ Heisenberg chain [107, 108], and highlight that the model has two species of quasi-particles.

The calculations presented in this Chapter generalise to nested systems the calculations of [107], and together provide a comprehensive analysis of low-temperature ballistic transport properties in non-relativistic integrable systems.

5.A Appendix: Low-temperature expansion of the homogeneous TBA

In this Appendix we derive the formulae of the low temperature expansion of the equilibrium thermodynamics of the Yang–Gaudin model, which appear in Section 5.3.2. The main goal is to derive the expansion (5.96) for a generic conserved charge.

5.A.1 Expansion of the pseudoenergy

In the following we present the derivation of the expansions (5.65)–(5.66) of the pseudoenergies. We start from the TBA equations (5.32)–(5.33)

$$\varepsilon^{(1)}_{1,T} = e - h - T\sum_{m=1}^{\infty} a_m \star \log(1+e^{-\varepsilon^{(2)}_{m,T}/T}), \tag{5.129}$$

$$\varepsilon^{(2)}_{n,T} = 2nh - Ta_n \star \log(1+e^{-\varepsilon^{(1)}_{1,T}/T}) + T\sum_{m=1}^{\infty} A_{nm} \star \log(1+e^{-\varepsilon^{(2)}_{m,T}/T}). \tag{5.130}$$

Since the pseudoenergy of the bound states is always positive (see (5.36)), the $n \geq 2$ terms of the sums are exponentially suppressed at small temperatures. After subtracting the ground state equations (5.54)–(5.55), we have

$$\begin{aligned}\delta\varepsilon^{(1)}_{1,T}(\lambda) = &-T\, a_1 \star \log(1+e^{-\varepsilon^{(2)}_{1,T}/T})(\lambda) - \int_{-B^{(2)}}^{B^{(2)}} \mathrm{d}\mu\, a_1(\lambda-\mu)\varepsilon^{(2)}_{1,0}(\mu) \\ &+ O(e^{-A^{(2)}/T}),\end{aligned} \tag{5.131}$$

$$\begin{aligned}\delta\varepsilon^{(2)}_{1,T}(\lambda) = &-T\, a_1 \star \log(1+e^{-\varepsilon^{(1)}_{1,T}/T})(\lambda) - \int_{-B^{(1)}}^{B^{(1)}} \mathrm{d}\mu\, a_1(\lambda-\mu)\varepsilon^{(1)}_{1,0}(\mu) \\ &+ T\, a_2 \star \log(1+e^{-\varepsilon^{(2)}_{1,T}/T})(\lambda) + \int_{-B^{(2)}}^{B^{(2)}} \mathrm{d}\mu\, a_2(\lambda-\mu)\varepsilon^{(2)}_{1,0}(\mu) \\ &+ O(e^{-A^{(2)}/T}),\end{aligned} \tag{5.132}$$

with some $A^{(r)} > 0$. Now we plug in the relation

$$\log(1+e^{-f(\lambda)}) = -f^-(\lambda) + \log(1+e^{-|f(\lambda)|}), \tag{5.133}$$

where

$$f^{\pm}(\lambda) = (f(\lambda) \pm |f(\lambda)|)/2, \tag{5.134}$$

obtaining

$$\begin{aligned}
\delta\varepsilon^{(1)}_{1,T}(\lambda) = &- \int_{-B^{(2)}}^{B^{(2)}} d\mu\, a_1(\lambda-\mu)\delta\varepsilon^{(2)}_{1,T}(\mu) - \int_{-B^{(2)\prime}}^{-B^{(2)}} d\mu\, a_1(\lambda-\mu)\varepsilon^{(2)}_{1,T}(\mu) \\
&- \int_{B^{(2)}}^{B^{(2)\prime}} d\mu\, a_1(\lambda-\mu)\varepsilon^{(2)}_{1,T}(\mu) \\
&+ T\int_{-\infty}^{\infty} d\mu\, a_1(\lambda-\mu)\log(1+e^{-|\varepsilon^{(2)}_{1,T}(\mu)|/T}) + O(e^{-A^{(2)}/T}),
\end{aligned} \tag{5.135}$$

$$\begin{aligned}
\delta\varepsilon^{(2)}_{1,T}(\lambda) = &- \int_{-B^{(1)}}^{B^{(1)}} d\mu\, a_1(\lambda-\mu)\delta\varepsilon^{(1)}_{1,T}(\mu) - \int_{-B^{(1)\prime}}^{-B^{(1)}} d\mu\, a_1(\lambda-\mu)\varepsilon^{(1)}_{1,T}(\mu) \\
&- \int_{B^{(1)}}^{B^{(1)\prime}} d\mu\, a_1(\lambda-\mu)\varepsilon^{(1)}_{1,T}(\mu) \\
&+ T\int_{-\infty}^{\infty} d\mu\, a_1(\lambda-\mu)\log(1+e^{-|\varepsilon^{(1)}_{1,T}(\mu)|/T}) \\
&+ \int_{-B^{(2)}}^{B^{(2)}} d\mu\, a_2(\lambda-\mu)\delta\varepsilon^{(2)}_{1,T}(\mu) + \int_{-B^{(2)\prime}}^{-B^{(2)}} d\mu\, a_2(\lambda-\mu)\varepsilon^{(2)}_{1,T}(\mu) \\
&+ \int_{B^{(2)}}^{B^{(2)\prime}} d\mu\, a_2(\lambda-\mu)\varepsilon^{(2)}_{1,T}(\mu) \\
&- T\int_{-\infty}^{\infty} d\mu\, a_2(\lambda-\mu)\log(1+e^{-|\varepsilon^{(2)}_{1,T}(\mu)|/T}) + O(e^{-A^{(2)}/T}),
\end{aligned} \tag{5.136}$$

where $B^{(r)\prime}$ is defined by

$$\varepsilon^{(r)}_{1,T}(B^{(r)\prime}) = 0. \tag{5.137}$$

Here we assume that $\varepsilon^{(r)}_{1,T}(\lambda)$ remain even and have two zeros, similarly to $\varepsilon^{(r)}_{1,0}(\lambda)$ (see Fig. 5.2). However, the locations of the zeros are shifted from the Fermi rapidities $\pm B^{(r)}$ to $\pm B^{(r)\prime}$.

Let us now analyse the terms in the RHS of (5.135). The first term does not explicitly depend on T. The second and third terms will be shown later to be $O(T^4)$. Hence (5.135) is dominated by the fourth term, which can be expanded as

$$\begin{aligned}
&\int_{-\infty}^{\infty} d\mu\, a_1(\lambda-\mu)\log(1+e^{-|\varepsilon^{(2)}(\mu)|/T}) = \\
&\quad = \frac{T}{|\varepsilon'(B^{(2)\prime})|}\sum_{\sigma=\pm} a_1(\lambda-\sigma B^{(2)\prime})\int_0^{\infty} dx\log(1+e^{-x}) + O(T^2) \\
&\quad = \frac{T\pi^2}{6|\varepsilon'(B^{(2)})|}\sum_{\sigma=\pm} a_1(\lambda-\sigma B^{(2)}) + O(T^2).
\end{aligned} \tag{5.138}$$

In this expansion we used that $|B^{(2)} - B^{(2)\prime}|$ changes smoothly in the vicinity of

$T=0$. After plugging (5.138) into (5.135), we obtain

$$\begin{aligned}\delta\varepsilon^{(1)}_{1,T}(\lambda) = \frac{\pi T^2}{6|\varepsilon^{(2)}_{1,T}(B^{(2)})|}\sum_{\sigma=\pm} a_1(\lambda-\sigma B^{(2)}) \\ -\int_{-B^{(2)}}^{B^{(2)}} d\mu\, a_1(\lambda-\mu)\delta\varepsilon^{(2)}_{1,T}(\mu) + o(T^2)\,,\end{aligned} \tag{5.139}$$

where $o(T^2)$ is such that

$$\lim_{T\to 0}\frac{o(T^2)}{T^2} = 0\,. \tag{5.140}$$

By repeating the above procedure for $\delta\varepsilon^{(2)}_{1,T}$, we obtain

$$\begin{aligned}\delta\varepsilon^{(2)}_{1,T}(\lambda) = \frac{\pi T^2}{6|\varepsilon^{(1)}_{1,T}(B^{(1)})|}\sum_{\sigma=\pm} a_1(\lambda-\sigma B^{(1)}) - \int_{-B^{(1)}}^{B^{(1)}} d\mu\, a_1(\lambda-\mu)\delta\varepsilon^{(1)}_{1,T}(\mu) \\ - \frac{\pi T^2}{6|\varepsilon^{(2)}_{1,T}(B^{(2)})|}\sum_{\sigma=\pm} a_2(\lambda-\sigma B^{(2)}) + \int_{-B^{(2)}}^{B^{(2)}} d\mu\, a_2(\lambda-\mu)\delta\varepsilon^{(2)}_{1,T}(\mu) \\ + o(T^2),\end{aligned} \tag{5.141}$$

where we used that the second, third, sixth, and seventh terms on the RHS of (5.136) are $O(T^4)$.

The equations (5.139)–(5.141) are identical to the system (5.65)-(5.72) of the main text.

Let us now prove that the second and third terms in the r.h.s. of (5.135) and the second, third, sixth, and seventh terms on the RHS of (5.136) are $O(T^4)$. By expanding these terms for $B^{(r)\prime}\sim B^{(r)}$ and using $\varepsilon^{(r)}_{1,0}(B^{(r)})=0$ we have

$$-\int_{-B^{(2)\prime}}^{-B^{(2)}} d\mu\, a_1(\lambda-\mu)\varepsilon^{(2)}_{1,T}(\mu) - \int_{B^{(2)}}^{B^{(2)\prime}} d\mu\, a_1(\lambda-\mu)\varepsilon^{(2)}_{1,T}(\mu) = O((B^{(2)\prime}-B^{(2)})^2)\,, \tag{5.142}$$

$$-\int_{-B^{(1)\prime}}^{-B^{(1)}} d\mu\, a_1(\lambda-\mu)\varepsilon^{(1)}_{1,T}(\mu) - \int_{B^{(1)}}^{B^{(1)\prime}} d\mu\, a_1(\lambda-\mu)\varepsilon^{(1)}_{1,T}(\mu) = O((B^{(1)\prime}-B^{(1)})^2)\,, \tag{5.143}$$

$$\int_{-B^{(2)\prime}}^{-B^{(2)}} d\mu\, a_2(\lambda-\mu)\varepsilon^{(2)}_{1,T}(\mu) + \int_{B^{(2)}}^{B^{(2)\prime}} d\mu\, a_2(\lambda-\mu)\varepsilon^{(2)}_{1,T}(\mu) = O((B^{(2)\prime}-B^{(2)})^2)\,. \tag{5.144}$$

We now assume that

$$B^{(r)\prime} - B^{(r)} = O(T^{\alpha_r}) \qquad\qquad \alpha_r > 0\,. \tag{5.145}$$

Let us prove that $\alpha_r>0$ by *reductio ad absurdum*. Suppose that $0<\alpha_2\le 1$. Then, using (5.135) we have

$$\delta\varepsilon^{(1)}_{1,T}(\lambda) = T^{2\alpha_2}F^{(1)}(\lambda) + O(T^2), \tag{5.146}$$

for some $F^{(1)}(\lambda)$ independent of T. If we then take $\delta\varepsilon^{(1)}_{1,T}(B^{(1)\prime})$ and expand around $\lambda=B^{(1)}$, we get

$$\begin{aligned}\delta\varepsilon^{(1)}_{1,T}(B^{(1)\prime}) &= -\varepsilon^{(1)\prime}_{1,T}(B^{(1)})(B^{(1)\prime}-B^{(1)}) + O((B^{(1)\prime}-B^{(1)})^2) \\ &= T^{2\alpha_2}F^{(1)}(\lambda) + O(T^2).\end{aligned} \tag{5.147}$$

So we conclude $\alpha_1 = 2\alpha_2$. Using now (5.136) we have

$$\delta\varepsilon^{(2)}_{1,T}(\lambda) = T^{2\alpha_2} F^{(2)}(\lambda) + O(T^{4\alpha_2}). \tag{5.148}$$

Expanding $\delta\varepsilon^{(2)}_{1,T}(B^{(2)\prime})$ for $B^{(2)\prime}$ around $\lambda = B^{(2)}$ we then get

$$\begin{aligned}\delta\varepsilon^{(2)}_{1,T}(B^{(2)\prime}) &= -\varepsilon^{(2)\prime}_{1,T}(B^{(2)})(B^{(2)\prime} - B^{(2)}) + O((B^{(2)\prime} - B^{(2)})^2) \\ &= T^{2\alpha_2} F^{(2)}(\lambda) + O(T^{4\alpha_2}).\end{aligned} \tag{5.149}$$

This is, however, not compatible with the hypothesis because it would require $\varepsilon^{(2)\prime}_{1,0}(B^{(2)}) = 0$. So we must have $\alpha_2 > 1$, implying that Eq. (5.139) holds. This in turn implies that $\alpha_1 > 1$, indeed by expanding $\delta\varepsilon^{(1)}_{1,T}(B^{(1)\prime})$ for $B^{(1)\prime}$ around $\lambda = B^{(1)}$ we have

$$\delta\varepsilon^{(1)}_{1,T}(B^{(1)\prime}) = -\varepsilon^{(1)\prime}_{1,T}(B^{(1)})(B^{(1)\prime} - B^{(1)}) + O((B^{(1)\prime} - B^{(1)})^2) = O(T^2). \tag{5.150}$$

Since $\alpha_r > 1$ for $r = 1, 2$ we have that Eqs. (5.139) hold (5.141) hold. Expanding then $\delta\varepsilon^{(r)}_{1,T}(B^{(r)\prime})$ for $B^{(r)\prime}$ around $\lambda = B^{(r)}$ we have

$$B^{(r)\prime} - B^{(r)} = -\frac{\pi^2 T^2}{6(\varepsilon^{(r)\prime}_{1,0}(B^{(r)}))^2} U^{(r)}(B^{(r)}) + o(T^2) \tag{5.151}$$

where the functions $U^{(r)}(x)$ are defined in the main text (*cf.* Eqs. (5.67)-(5.68)). This proves that (5.142)-(5.144) are $O(T^4)$.

5.A.2 Expansion of the particle density and velocity

Now we show how the low temperature corrections (5.83)–(5.84) and (5.90)–(5.91) are derived for the particle density $\rho^{(r)}_{n,T}(\lambda)$ and the particle velocity $v^{(r)}_{n,T}(\lambda)$. This derivation is based the expansion (5.75)–(5.76) of the integral

$$I^{(r)}_f = \int_{-\infty}^{\infty} \mathrm{d}\lambda \;\; \vartheta^{(r)}_{1,T}(\lambda) f(\lambda), \tag{5.152}$$

which is reported in [107]. In explicit notation the expansion reads as

$$\begin{aligned}I^{(r)}_f = &\int_{-B^{(r)}}^{B^{(r)}} d\lambda f(\lambda) + \frac{\pi^2 T^2}{6(\varepsilon^{(r)\prime}_{1,0}(B^{(2)}))^2} \left[f'(B^{(r)}) - f'(-B^{(r)})\right] \\ &- \frac{\pi^2 T^2}{6(\varepsilon^{(r)\prime}_{1,0}(B^{(2)}))^2} \left[\left(\frac{\varepsilon^{(r)\prime\prime}_{1,0}(B^{(r)})}{\varepsilon^{(r)\prime}(B^{(r)})} + U(B^{(r)})\right)(f(B^{(r)}) + f(-B^{(r)}))\right],\end{aligned} \tag{5.153}$$

where we neglected sub-leading contributions.

Now, considering (5.73)–(5.74) and separating the ground state root densities $\rho^{(r)}_{1,\mathrm{t},0}$ from the corrections $\delta\rho^{(r)}_{1,\mathrm{t}}$ we have

$$\rho^{(1)}_{1,\mathrm{t},0}(\lambda)+\delta\rho^{(1)}_{1,\mathrm{t}}(\lambda)=\frac{1}{2\pi}+a_1\star\vartheta^{(2)}_{1,T}\rho^{(2)}_{1,\mathrm{t},0}(\lambda)+a_1\star\vartheta^{(2)}_{1,T}\delta\rho^{(2)}_{1,\mathrm{t}}(\lambda), \tag{5.154}$$

$$\begin{aligned}\rho^{(2)}_{1,\mathrm{t},0}(\lambda)+\delta\rho^{(2)}_{1,\mathrm{t}}(\lambda)=&\,a_1\star\vartheta^{(1)}_{1,T}\rho^{(1)}_{1,\mathrm{t},0}(\lambda)+a_1\star\vartheta^{(1)}_{1,T}\delta\rho^{(1)}_{1,\mathrm{t}}(\lambda)\\&-a_2\star\vartheta^{(2)}_{1,T}\rho^{(2)}_{1,\mathrm{t},0}(\lambda)-a_2\star\vartheta^{(2)}_{1,T}\delta\rho^{(2)}_{1,\mathrm{t}}(\lambda).\end{aligned} \tag{5.155}$$

Applying now (5.153) to the convolutions and retaining corrections up to $O(T^2)$ we have

$$a_r\star\vartheta^{(s)}_{1,T}\delta\rho^{(s)}_{1,\mathrm{t}}(\lambda)=a_r*\delta\rho^{(s)}_{1,\mathrm{t}}(\lambda)\Big|_s\,, \tag{5.156}$$

$$a_r\star\vartheta^{(s)}_{1,T}\rho^{(s)}_{1,\mathrm{t},0}(\lambda)=a_r*\rho^{(s)}_{1,\mathrm{t},0}(\lambda)\Big|_s+\frac{\pi^2T^2}{6}a_r*z^{(s)}_U(\lambda)\Big|_s\,,\qquad r,s=1,2\,, \tag{5.157}$$

where we used the definition (5.56) for the ground state convolution and the function $z^{(s)}_U(\lambda)$ is of the form (5.71) with the coefficients (5.85)–(5.87). Plugging into (5.154)–(5.155) the expressions (5.157) for the convolutions and subtracting the ground state equations (5.58)–(5.59) we finally obtain (5.83)–(5.84).

The low-temperature expansion for the excitation velocities is obtained in a similar manner. One has to remove the exponentially suppressed bound state terms from the system (5.42)–(5.43), obtaining

$$v^{(1)}_{1,T}\rho^{(1)}_{1,\mathrm{t},T}(\lambda)=\frac{e'(\lambda)}{2\pi}+a_1\star\vartheta^{(2)}_{1,T}v^{(2)}_{1,T}\rho^{(2)}_{1,\mathrm{t},T}(\lambda), \tag{5.158}$$

$$v^{(2)}_{1,T}\rho^{(2)}_{1,\mathrm{t},T}(\lambda)=a_1\star\vartheta^{(1)}_{1,T}v^{(1)}_{1,T}\rho^{(1)}_{1,\mathrm{t},T}(\lambda)-a_2\star\vartheta^{(2)}_{1,T}v^{(2)}_{1,T}\rho^{(2)}_{1,\mathrm{t},T}(\lambda). \tag{5.159}$$

Then by applying (5.153) to the convolutions we find (5.90)–(5.91).

5.A.3 The first correction to the energy

In this Appendix we derive (5.96), which is necessary to derive the low temperature correction to the energy density, δe (5.100). First, it is necessary to introduce a vectorial notation for the sake of compactness. To a function $w^{(r)}(\lambda)$ we associate the vector w, whose components are

$$[w]_{r,\lambda}=w^{(r)}(\lambda). \tag{5.160}$$

Operators $\hat{K}$ acting on these vectors are defined as

$$[\hat{K}\,w]_{r,\lambda}=\sum_{s=1}^{2}\int_{-B^{(s)}}^{B^{(s)}}d\mu K_{rs}(\lambda-\mu)w^{(s)}(\mu). \tag{5.161}$$

In this notation, the low temperature BGT equations (5.73)–(5.74) read

$$\rho_{\mathrm{t}}=d_\rho-\hat{A}\hat{\vartheta}\rho_{\mathrm{t}}, \tag{5.162}$$

where

$$\rho_{\rm t} = \begin{bmatrix} \rho^{(1)}_{1,{\rm t},T}(\lambda) \\ \rho^{(2)}_{1,{\rm t},T}(\lambda) \end{bmatrix}, \qquad [\hat{\vartheta}] = \begin{bmatrix} \vartheta^{(1)}_1(\lambda-\mu) & 0 \\ 0 & \vartheta^{(2)}_1(\lambda-\mu) \end{bmatrix} \cdot \delta(\lambda-\mu), \tag{5.163}$$

$$d_\rho = \begin{bmatrix} \frac{1}{2\pi} \\ 0 \end{bmatrix}, \qquad [\hat{A}] = \begin{bmatrix} 0 & -a_1(\lambda-\mu) \\ -a_1(\lambda-\mu) & a_2(\lambda-\mu) \end{bmatrix}. \tag{5.164}$$

In the same notation, the first correction to the densities (5.83)–(5.84) reads

$$\delta\rho_{{\rm t},T} = \frac{\pi^2 T^2}{6} R, \qquad R = d_R - \hat{A}R, \tag{5.165}$$

where

$$\delta\rho_{{\rm t},T} = \begin{bmatrix} \delta\rho^{(1)}_{1,{\rm t},T}(\lambda) \\ \delta\rho^{(2)}_{1,{\rm t},T}(\lambda) \end{bmatrix}, \qquad d_R = -\hat{A} z_{R,I}, \qquad z_{R,I} = \begin{bmatrix} z^{(1)}_{R,I}(\lambda) \\ z^{(2)}_{R,I}(\lambda) \end{bmatrix}. \tag{5.166}$$

The functions $z^{(r)}_{R,I}(\lambda)$ are given by the coefficients (5.85)–(5.87).

To prove (5.96), we start from the left hand side of (5.96)

$$\sum_{r=1}^{2} \int_{-\infty}^{\infty} {\rm d}\lambda (R^{(r)}(\lambda) + z^{(r)}_{R,I}(\lambda)) q^{(r)}(\lambda). \tag{5.167}$$

Using the vector notation and (5.165)– (5.166), this correction can be written as the scalar product

$$q \cdot (-(\hat{1}+\hat{A})^{-1}\hat{A} z_{R,I} + z_{R,I}) = q \cdot (\hat{1}+\hat{A})^{-1} z_{R,I}, \tag{5.168}$$

where the scalar product is defined as

$$a \cdot b = \sum_{r=1}^{2} \int_{-B^{(r)}}^{B^{(r)}} {\rm d}\lambda\, a^{(r)}(\lambda) b^{(r)}(\lambda). \tag{5.169}$$

Since $\hat{A}$ is symmetric, we can write (5.168) as

$$((\hat{1}+\hat{A})^{-1} q) \cdot z_{R,I} \equiv f_q \cdot z_{R,I}, \qquad f_q = q - \hat{A} f_q. \tag{5.170}$$

Writing this result in the standard TBA notation yields exactly the identity (5.96).

5.B Appendix: Expansion of the density and current profiles in the inhomogeneous case

In this Appendix we show the derivation of the low temperature expansions (5.111)–(5.112) and (5.126)–(5.127) of the charge and current density profiles after a bipartite quench. In other words, we will evaluate

$$q(\mathfrak{r},\zeta) = \sum_{r=1,2} \int_{-\infty}^{\infty} {\rm d}\lambda \rho^{(r)}_{1,{\rm t},\zeta}(\lambda) \vartheta^{(r)}_{1,\zeta}(\lambda) q^{(r)}(\lambda), \tag{5.171}$$

$$j(\mathfrak{r},\zeta) = \sum_{r=1,2} \int_{-\infty}^{\infty} {\rm d}\lambda \rho^{(r)}_{1,{\rm t},\zeta}(\lambda) \vartheta^{(r)}_{1,\zeta}(\lambda) v^{(r)}_{1,\zeta}(\lambda) q^{(r)}(\lambda), \tag{5.172}$$

at low temperatures. In (5.171)–(5.172) we have already used the fact that bound states are exponentially suppressed at small enough temperatures.

The basis of the evaluation of (5.171)–(5.172) is the expansion (5.108)–(5.120), carried out in detail in [107]. This expansion has two cases according to whether the ray ζ is close to one of the light cones $\pm v_{1,0}^{(r)}(B^{(r)})$ or not. We treat these two cases separately. Our computations below are valid up to $O(T^2)$.

5.B.1 The case $\lim_{T\to 0} |\zeta - v_{1,0}^{(r)}(B^{(r)})| \neq 0$

Far away from the light cones, one can use the low temperature expansion (5.109). First we compute the correction to the charge density

$$\delta q(\mathfrak{r},\zeta) = \sum_{r=1,2} \int_{-\infty}^{\infty} \mathrm{d}\lambda \rho_{1,\mathrm{t},\zeta}^{(r)}(\lambda)\vartheta_{1,\zeta}^{(r)}(\lambda)q^{(r)}(\lambda) - \sum_{r=1,2} \int_{-B^{(r)}}^{B^{(r)}} \mathrm{d}\lambda \rho_{1,\mathrm{t},0}^{(r)}(\lambda)q^{(r)}(\lambda). \quad (5.173)$$

The vectorial form of the $O(T^2)$ expansion (5.109) is

$$I_{\zeta,f} = f\cdot j + \frac{\pi T^2}{6} f\cdot z_{I,\zeta}, \quad (5.174)$$

where

$$I_{\zeta,f} = \begin{bmatrix} I_{\zeta,f}^{(1)} \\ I_{\zeta,f}^{(2)} \end{bmatrix}, \quad f = \begin{bmatrix} f^{(1)} \\ f^{(2)} \end{bmatrix}, \quad j = \begin{bmatrix} 1 \\ 1 \end{bmatrix}, \quad z_{I,\zeta} = \begin{bmatrix} z_{I,\zeta}^{(r)} \\ z_{I,\zeta}^{(r)} \end{bmatrix}. \quad (5.175)$$

Using expansion (5.174) on the BGT equations (5.73)–(5.74) yields

$$\delta\rho_{\mathrm{t},\zeta} = \frac{\pi^2 T^2}{6} R_\zeta, \qquad R_\zeta = d_{R,\zeta} - \hat{A} R_\zeta, \quad (5.176)$$

where

$$\delta\rho_{\mathrm{t},\zeta} = \begin{bmatrix} \delta\rho_{1,\mathrm{t},\zeta}^{(1)}(\lambda) \\ \delta\rho_{1,\mathrm{t},\zeta}^{(2)}(\lambda) \end{bmatrix}, \qquad d_{R,\zeta} = -\hat{A} z_{R,I,\zeta}, \qquad z_{R,I,\zeta} = \begin{bmatrix} z_{R,I,\zeta}^{(1)}(\lambda) \\ z_{R,I,\zeta}^{(2)}(\lambda) \end{bmatrix}, \quad (5.177)$$

and the symbol δ denotes difference from the ground state value, i.e.,

$$\delta\rho_{1,\mathrm{t},\zeta} = \rho_{1,\mathrm{t},\zeta} - \rho_{1,\mathrm{t},0}. \quad (5.178)$$

The function $z_{R,I,\zeta}^{(r)}(\lambda)$ is

$$\begin{aligned} z_{R,I,\zeta}^{(r)}(\lambda) = {} & z_{R,I}^{(r)}(\lambda)\Theta_H[-v_{1,0}^{(r)}(B^{(r)}) - \zeta] \\ & + \left(\mathfrak{r}^2 z_{R,I,-}^{(r)}(\lambda) + z_{R,I,+}^{(r)}(\lambda)\right)\Theta_H[v_{1,0}^{(r)}(B^{(r)}) - |\zeta|] \\ & + \mathfrak{r}^2 z_{R,I}^{(r)}(\lambda)\Theta_H[\zeta - v_{1,0}^{(r)}(B^{(r)})], \end{aligned} \quad (5.179)$$

with $z_{R,I}^{(r)}(\lambda)$ and $z_{R,I,\pm}^{(r)}(\lambda)$ given by the coefficients (5.85)–(5.87).

Plugging (5.176) in (5.173) and using the expansion (5.174), we get

$$\delta q(\mathfrak{r},\zeta) = \frac{\pi^2 T^2}{6} q \cdot (-(\hat{1}+\hat{A})^{-1}\hat{A} z_{R,I,\zeta} + z_{R,I,\zeta}) = \frac{\pi^2 T^2}{6} q \cdot ((\hat{1}+\hat{A})^{-1} z_{R,I,\zeta}). \quad (5.180)$$

Since $\hat{A}$ is symmetric, we can write (5.180) as

$$\delta q(\mathfrak{r},\zeta) = \frac{\pi^2 T^2}{6}((\hat{1}+\hat{A})^{-1} q) \cdot z_{R,I,\zeta} \equiv \frac{\pi^2 T^2}{6} f_q \cdot z_{R,I,\zeta}, \qquad f_q = q - \hat{A} f_q. \quad (5.181)$$

This is exactly (5.111) in vectorial notation, which is valid up to $O(T^2)$. We note that the above expansion is analogous to the homogeneous case shown in Appendix 5.A.3. The only difference is the dependence of the vector $z_{R,I,\zeta}$ on ζ.

In the case of the charge current density $\delta j(\mathfrak{r},\zeta)$, the logic of the derivation is the same. We have

$$\begin{aligned}\delta j(\mathfrak{r},\zeta) = &\sum_{r=1,2} \int_{-\infty}^{\infty} \mathrm{d}\lambda \rho^{(r)}_{1,\mathrm{t},\zeta}(\lambda) \vartheta^{(r)}_{1,\zeta}(\lambda) v^{(r)}_{1,\zeta}(\lambda) q^{(r)}(\lambda) \\ &- \sum_{r=1,2} \int_{-\infty}^{\infty} \mathrm{d}\lambda \rho^{(r)}_{1,\mathrm{t},0}(\lambda) v^{(r)}_{1,\zeta}(\lambda) q^{(r)}(\lambda).\end{aligned} \quad (5.182)$$

In vectorial notation, the equations (5.158)–(5.159) for the velocities become

$$w_\zeta = d_w - \hat{A}\hat{\vartheta}_\zeta w_\zeta, \quad (5.183)$$

with

$$w_\zeta = \begin{bmatrix} \rho^{(1)}_{1,\mathrm{t},\zeta}(\lambda) v^{(1)}_{1,\zeta}(\lambda) \\ \rho^{(2)}_{1,\mathrm{t},\zeta}(\lambda) v^{(2)}_{1,\zeta}(\lambda) \end{bmatrix}, \quad d_w = \begin{bmatrix} \lambda/(2\pi) \\ 0 \end{bmatrix}. \quad (5.184)$$

Using the expansion (5.174) on (5.183) yields

$$\delta w_\zeta = \frac{\pi T^2}{6} W_\zeta, \quad W_\zeta = d_{W,\zeta} - \hat{A} W_\zeta, \quad (5.185)$$

where

$$d_{W,\zeta} = \hat{A} z_{W,I,\zeta}, \quad z_{W,I,\zeta} = \begin{bmatrix} z^{(1)}_{W,I,\zeta}(\lambda) \\ z^{(2)}_{W,I,\zeta}(\lambda) \end{bmatrix}. \quad (5.186)$$

The functions $z^{(r)}_{W,I,\zeta}(\lambda)$ are given by

$$\begin{aligned} z^{(r)}_{W,I,\zeta}(\lambda) = &\, z^{(r)}_{W,I}(\lambda) \Theta_H[-v^{(r)}_{1,0}(B^{(r)}) - \zeta] \\ &+ (\mathfrak{r}^2 z^{(r)}_{W,I,-}(\lambda) + z^{(r)}_{W,I,+}(\lambda))\, \Theta_H[v^{(r)}_{1,0}(B^{(r)}) - |\zeta|] \\ &+ \mathfrak{r}^2 z^{(r)}_{W,I}(\lambda) \Theta_H[\zeta - v^{(r)}_{1,0}(B^{(r)})], \end{aligned} \quad (5.187)$$

with $z^{(r)}_{W,I}(\lambda)$ and $z^{(r)}_{W,I,\pm}(\lambda)$ given by the coefficients (5.92)–(5.94).

Plugging (5.185) into (5.182) and using the expansion (5.174), we get

$$\delta j(\mathfrak{r},\zeta) = \frac{\pi^2 T^2}{6} q \cdot (-(\hat{1}+\hat{A})^{-1}\hat{A} z_{W,I,\zeta} + z_{W,I,\zeta}) = \frac{\pi^2 T^2}{6} q \cdot ((\hat{1}+\hat{A})^{-1} z_{W,I,\zeta}). \quad (5.188)$$

Since $\hat{A}$ is symmetric, we can write (5.180) as

$$\delta j(\mathfrak{r},\zeta) = \frac{\pi T^2}{6}((\hat{1}+\hat{A})^{-1}q)\cdot z_{W,I,\zeta} \equiv \frac{\pi^2 T^2}{6} f_q \cdot z_{W,I,\zeta}, \qquad f_q = q - \hat{A} f_q. \quad (5.189)$$

This is exactly (5.112) in vectorial notation, which is valid up to $O(T^2)$.

5.B.2 The case $\zeta \pm v_{1,0}^{(r)}(B^{(r)}) \sim O(T)$

Close to the light cones, we use the expansion (5.120) instead of (5.109) but otherwise the procedure is the same as in the far-from-lightcone case of Appendix 5.B.1. We can get the final results by replacing $z_{R,I,\zeta}$ and $z_{W,I,\zeta}$ with $z_{II,\zeta}$ in Eqs. (5.181) and (5.189). The final result is

$$\delta q(\mathfrak{r},\zeta) = \frac{\pi^2 T(1-\mathfrak{r}^2)}{6}((\hat{1}+\hat{A})^{-1}q)\cdot z_{II,\zeta} \equiv \frac{\pi^2 T(1-\mathfrak{r}^2)}{6} f_q \cdot z_{II,\zeta}, \quad (5.190)$$

$$\delta j(\mathfrak{r},\zeta) = \frac{\pi^2 T(1-\mathfrak{r}^2)}{6}((\hat{1}+\hat{A})^{-1}q)\cdot z_{II,\zeta} \equiv \frac{\pi^2 T(1-\mathfrak{r}^2)}{6} f_q \cdot z_{II,\zeta}, \quad (5.191)$$

where $f_q = q - \hat{A} f_q$. These are exactly (5.126)–(5.127) in vectorial notation, valid up to $O(T)$.

Chapter 6

Conclusions

The results presented in this Thesis fall into two categories: first, the *generalization* of existing approaches, including the Quench Action [33] and the Generalized Hydrodynamics [31, 32] to more complex integrable quantum models; and second, the development of new computational *methods*, which are tested in the paradigmatic case of XXZ Heisenberg spin chain.

The first category contains our analysis of a global quantum quench in the spin-1, SU(3) invariant Lai–Sutherland chain (see Chapter 3). We *generalized* the Quench Action formalism to this nested Bethe ansatz solvable model. We used this generalization to characterize the post-quench relaxed state by its root densities, and then to compute the evolution of entanglement entropy in the quasiparticle picture. Since then, a class of other integrable initial states have been found in the same model for which the Quench Action formalism can be carried out [89, 225, 226]. An interesting research direction would be generalizing the analytical formulas for correlation functions existing in the XXZ model [74, 75] to this nested model. This would make it possible to compute analytically local correlation functions in the post-quench stationary state.

The other result falling in the first category is the *generalization* of the low-temperature expansion of GHD to a nested Bethe ansatz solvable system, the Yang–Gaudin model (see Chapter 5). By carrying out this low-temperature expansion, we demonstrated that not only the thermodynamics [220], but also the transport properties of the model is described by the superposition of two CFT. Possible future research includes making the GHD formalism more robust by proving analytically the existence of quasilocal charges pertaining to the spin degrees of freedom, and generalizing existing proofs [133, 134] for the TBA formulae for the expectation values of the currents.

As we have written, the second category of our includes new computational *methods,* tested in the XXZ model. One of these *methods* allows us to compute the Rényi entropy of the GGE describing a thermodynamic macrostate (see Chapter 2). In principle, this method works in any integrable model. Further research could involve these methods in generalizing the quasiparticle picture [141, 172] from the von Neumann entropy to Rényi entropies. However, it is not clear yet whether this

generalization is possible.

Finally, we have also reported on a result which falls into both categories. We developed a numerical *method* for computing the evolution of entanglement-related quantities within the generalized hydrodynamics description of an inhomogeneous quench (see Chapter 4). In developing this method, we *generalized* the existing flea gas picture of hydrodynamics [113] from the Lieb–Liniger to the XXZ model, and joined the flea gas together with the quasiparticle picture of entanglement evolution. Our method is versatile in the sense that it should work with different integrable models, different partitions and entanglement measures. Specifically, it can compute the evolution of mutual information, for which no analytical result is available in the inhomogeneous setting. While we have presented robust numerical evidence for our method, it remains to be proven analytically in the XXZ model.

Acknowledgments

First, I would like to thank my supervisor, Prof. Pasquale Calabrese for his academic guidance. I am grateful to him for his many insightful ideas and for his useful advice, both essential for carrying out the research presented in this Thesis. My main collaborators during my Ph.D. training were Vincenzo Alba, Bruno Bertini and Lorenzo Piroli. I thank them for the pleasure of working together, and for the many things I learned through our collaboration. I also thank Xi-Wen Guan, Márton Kormos, Jacopo De Nardis, Balázs Pozsgay and Gábor Takács for discussions that made a difference in my research.

I thank Anna, Dávid, Ipé, Lajos and Tibor for their beautiful friendship. There are many others whom I should thank here; their number is too great to list them all. I am grateful to my Parents and my sister Wanda for their unwavering support.

Bibliography

[1] J. Eisert, M. Friesdorf, and C. Gogolin, Nat. Phys. **11**, 124–130 (2015).

[2] C. Gogolin and J. Eisert, Rep. Prog. Phys. **79**, 056001 (2016).

[3] L. D'Alessio, Y. Kafri, A. Polkovnikov, and M. Rigol, Advances in Physics **65**, 239–362 (2016).

[4] I. Bloch, J. Dalibard, and W. Zwerger, Rev. Mod. Phys. **80**, 885–964 (2008).

[5] M. A. Cazalilla, R. Citro, T. Giamarchi, E. Orignac, and M. Rigol, Rev. Mod. Phys. **83**, 1405–1466 (2011).

[6] X.-W. Guan, M. T. Batchelor, and C. Lee, Rev. Mod. Phys. **85**, 1633–1691 (2013).

[7] A. Polkovnikov, K. Sengupta, A. Silva, and M. Vengalattore, Rev. Mod. Phys. **83**, 863–883 (2011).

[8] T. Kinoshita, T. Wenger, and D. S. Weiss, Nature **440**, 900–903 (2006).

[9] E. H. Lieb and W. Liniger, Phys. Rev. **130**, 1605–1616 (1963).

[10] P. Calabrese, F. H. L. Essler, and G. Mussardo, eds., *Journal of Statistical Mechanics: Theory and Experiment* (2016): *Quantum Integrability in Out of Equilibrium Systems*.

[11] G. Delfino, J. Phys. A: Math. Theor. **47**, 402001 (2014).

[12] V. P. Yurov and A. B. Zamolodchikov, I. J. Mod. Phys. A **05**, 3221–3245 (1990).

[13] A. J. A. James, R. M. Konik, P. Lecheminant, N. J. Robinson, and A. M. Tsvelik, Rep. Prog. Phys. **81**, 046002 (2018).

[14] J. M. Deutsch, Phys. Rev. A **43**, 2046–2049 (1991).

[15] M. Srednicki, Phys. Rev. E **50**, 888–901 (1994).

[16] M. Rigol, V. Dunjko, and M. Olshanii, Nature **452**, 854–858 (2008).

[17] M. Rigol, Phys. Rev. Lett. **103**, 100403 (2009).

[18] M. Rigol and M. Srednicki, Phys. Rev. Lett. **108**, 110601 (2012).

[19] P. Reimann, New J. Phys. **17**, 055025 (2015).

[20] J. M. Deutsch, Rep. Prog. Phys. **81**, 082001 (2018).

[21] M. Takahashi, *Thermodynamics of One-Dimensional Solvable Models* (Cambridge University Press, 1999).

[22] V. E. Korepin, N. M. Bogoliubov, and A. G. Izergin, *Quantum inverse scattering method and correlation functions* (Cambridge University Press, 1993).

[23] F. H. L. Essler, H. Frahm, F. Göhmann, A. Klümper, and V. E. Korepin, *The One-Dimensional Hubbard Model* (Cambridge University Press, 2010).

[24] H. Bethe, Z. Phys. **71**, 205–226 (1931).

[25] R. Orbach, Phys. Rev. **112**, 309–316 (1958).

[26] M. Gaudin, Phys. Rev. Lett. **26**, 1301–1304 (1971).

[27] C. N. Yang and C. P. Yang, J. of Mat. Phys. **10**, 1115–1122 (1969).

[28] E. Ilievski, M. Medenjak, and T. Prosen, Phys. Rev. Lett. **115**, 120601 (2015).

[29] E. Ilievski, M. Medenjak, T. Prosen, and L. Zadnik, J. Stat. Mech.: Theor. Exp. **2016**, 064008 (2016).

[30] L. Bonnes, F. H. L. Essler, and A. M. Läuchli, Phys. Rev. Lett. **113**, 187203 (2014).

[31] B. Bertini, M. Collura, J. De Nardis, and M. Fagotti, Phys. Rev. Lett. **117**, 207201 (2016).

[32] O. A. Castro-Alvaredo, B. Doyon, and T. Yoshimura, Phys. Rev. X **6**, 041065 (2016).

[33] J.-S. Caux and F. H. L. Essler, Phys. Rev. Lett. **110**, 257203 (2013).

[34] M. A. Cazalilla, Phys. Rev. Lett. **97**, 156403 (2006).

[35] D. Rossini, A. Silva, G. Mussardo, and G. E. Santoro, Phys. Rev. Lett. **102**, 127204 (2009).

[36] P. Calabrese, F. H. L. Essler, and M. Fagotti, J. Stat. Mech.: Theor. Exp. **2012**, P07022 (2012).

[37] M. A. Cazalilla, A. Iucci, and M.-C. Chung, Phys. Rev. E **85**, 011133 (2012).

[38] M. Fagotti and F. H. L. Essler, Phys. Rev. B **87**, 245107 (2013).

[39] M. Collura, S. Sotiriadis, and P. Calabrese, Phys. Rev. Lett. **110**, 245301 (2013).

[40] M. Fagotti, J. Stat. Mech.: Theor. Exp. **2014**, P03016 (2014).

[41] M. Kormos, M. Collura, and P. Calabrese, Phys. Rev. A **89**, 013609 (2014).

[42] S. Sotiriadis and P. Calabrese, J. Stat. Mech.: Theor. Exp. **2014**, P07024 (2014).

[43] J.-S. Caux and R. M. Konik, Phys. Rev. Lett. **109**, 175301 (2012).

[44] M. Kormos, A. Shashi, Y.-Z. Chou, J.-S. Caux, and A. Imambekov, Phys. Rev. B **88**, 205131 (2013).

[45] J. De Nardis, B. Wouters, M. Brockmann, and J.-S. Caux, Phys. Rev. A **89**, 033601 (2014).

[46] M. Collura, M. Kormos, and P. Calabrese, Phys. Rev. A **97**, 033609 (2018).

[47] G. Goldstein and N. Andrei, Phys. Rev. B **92**, 155103 (2015).

[48] F. H. L. Essler and M. Fagotti, J. Stat. Mech.: Theor. Exp. **2016**, 064002 (2016).

[49] R. Vasseur and J. E. Moore, J. Stat. Mech.: Theor. Exp. **2016**, 064010 (2016).

[50] M. A. Cazalilla and M.-C. Chung, J. Stat. Mech.: Theor. Exp. **2016**, 064004 (2016).

[51] L. Vidmar and M. Rigol, J. Stat. Mech.: Theor. Exp. **2016**, 064007 (2016).

[52] B. Pozsgay, J. Stat. Mech.: Theor. Exp. **2013**, P07003 (2013).

[53] M. Fagotti, M. Collura, F. H. L. Essler, and P. Calabrese, Phys. Rev. B **89**, 125101 (2014).

[54] M. Fagotti and F. H. L. Essler, J. Stat. Mech.: Theor. Exp. **2013**, P07012 (2013).

[55] B. Wouters, J. De Nardis, M. Brockmann, D. Fioretto, M. Rigol, and J.-S. Caux, Phys. Rev. Lett. **113**, 117202 (2014).

[56] M. Brockmann, B. Wouters, D. Fioretto, J. D. Nardis, R. Vlijm, and J.-S. Caux, J. Stat. Mech.: Theor. Exp. **2014**, P12009 (2014).

[57] B. Pozsgay, M. Mestyán, M. A. Werner, M. Kormos, G. Zaránd, and G. Takács, Phys. Rev. Lett. **113**, 117203 (2014).

[58] M. Mestyán, B. Pozsgay, G. Takács, and M. A. Werner, J. Stat. Mech.: Theor. Exp. **2015**, P04001 (2015).

[59] B. Pozsgay, J. Stat. Mech.: Theor. Exp. **2014**, P09026 (2014).

[60] E. Ilievski, J. De Nardis, B. Wouters, J.-S. Caux, F. H. L. Essler, and T. Prosen, Phys. Rev. Lett. **115**, 157201 (2015).

[61] E. A. Yuzbashyan, Ann. Phys. **367**, 288–296 (2016).

[62] L. Piroli, E. Vernier, and P. Calabrese, Phys. Rev. B **94**, 054313 (2016).

[63] L. Piroli, E. Vernier, P. Calabrese, and M. Rigol, Phys. Rev. B **95**, 054308 (2017).

[64] B. Pozsgay, E. Vernier, and M. A. Werner, J. Stat. Mech.: Theor. Exp. **2017**, 093103 (2017).

[65] E. Ilievski and E. Quinn, arXiv e-prints, arXiv:1904.11975, arXiv:1904.11975 (2019).

[66] A. D. Luca and G. Mussardo, J. Stat. Mech.: Theor. Exp. **2016**, 064011 (2016).

[67] D. Fioretto and G. Mussardo, New J. Phys. **12**, 055015 (2010).

[68] G. Mussardo, Phys. Rev. Lett. **111**, 100401 (2013).

[69] S. Sotiriadis, G. Takacs, and G. Mussardo, Phys. Lett. B **734**, 52–57 (2014).

[70] J.-S. Caux and F. H. L. Essler, Phys. Rev. Lett. **110**, 257203 (2013).

[71] F. H. L. Essler, G. Mussardo, and M. Panfil, J. Stat. Mech.: Theor. Exp. **2017**, 013103 (2017).

[72] E. Vernier and A. C. Cubero, J. Stat. Mech.: Theor. Exp. **2017**, 023101 (2017).

[73] G. Goldstein and N. Andrei, Phys. Rev. A **90**, 043625 (2014).

[74] M. Mestyán and B. Pozsgay, J. Stat. Mech.: Theor. Exp. **2014**, P09020 (2014).

[75] B. Pozsgay, J. Phys. A: Math. Theor. **50**, 074006 (2017).

[76] N. Kitanine, J. M. Maillet, and V. Terras, Nucl. Phys. B **567**, 554–582 (2000).

[77] N. Kitanine, J. M. Maillet, N. A. Slavnov, and V. Terras, J. Stat. Mech.: Theor. Exp. **2005**, L09002 (2005).

[78] H. E. Boos, F. Göhmann, A. Klümper, and J. Suzuki, J. Stat. Mech.: Theor. Exp. **2006**, P04001 (2006).

[79] H. Boos, M. Jimbo, T. Miwa, F. Smirnov, and Y. Takeyama, Lett. Math. Phys. **75**, 201–208 (2006).

[80] J. Damerau, F. Göhmann, N. P. Hasenclever, and A. Klümper, J. Phys. A: Math. Theor. **40**, 4439–4453 (2007).

[81] H. Boos, M. Jimbo, T. Miwa, F. Smirnov, and Y. Takeyama, Comm. Math. Phys. **272**, 263–281 (2007).

[82] M. Jimbo, T. Miwa, and F. Smirnov, J. Phys. A: Math. Theor. **42**, 304018 (2009).

[83] H. Boos and F. Göhmann, J. Phys. A: Math. Theor. **42**, 315001 (2009).

[84] C. Trippe, F. Göhmann, and A. Klümper, Eur. Phys. J. B **73**, 253–264 (2010).

[85] E. Ilievski, E. Quinn, J. D. Nardis, and M. Brockmann, J. Stat. Mech.: Theor. Exp. **2016**, 063101 (2016).

[86] J.-S. Caux, J. Stat. Mech.: Theor. Exp. **2016**, 064006 (2016).

[87] A. De Luca, G. Martelloni, and J. Viti, Phys. Rev. A **91**, 021603 (2015).

[88] M. Mestyán, B. Bertini, L. Piroli, and P. Calabrese, J. Stat. Mech.: Theor. Exp. **2017**, 083103 (2017).

[89] R. Modak, L. Piroli, and P. Calabrese, arXiv:1906.09238 (2019).

[90] L. Piroli, P. Calabrese, and F. H. Essler, Phys. Rev. Lett. **116**, 070408 (2016).

[91] L. Bucciantini, J. Stat. Phys. **164**, 621–644 (2016).

[92] J. C. Zill, T. M. Wright, K. V. Kheruntsyan, T. Gasenzer, and M. J. Davis, Phys. Rev. A **91**, 023611 (2015).

[93] L. Piroli, B. Pozsgay, and E. Vernier, Nucl. Phys. B **925**, 362–402 (2017).

[94] K. K. Kozlowski and B. Pozsgay, J. Stat. Mech.: Theor. Exp. **2012**, P05021 (2012).

[95] M. Brockmann, J. D. Nardis, B. Wouters, and J.-S. Caux, J. Phys. A: Math. Theor. **47**, 145003 (2014).

[96] V. B. Bulchandani, R. Vasseur, C. Karrasch, and J. E. Moore, Phys. Rev. B **97**, 045407 (2018).

[97] V. B. Bulchandani, R. Vasseur, C. Karrasch, and J. E. Moore, Phys. Rev. Lett. **119**, 220604 (2017).

[98] E. Ilievski and J. De Nardis, Phys. Rev. Lett. **119**, 020602 (2017).

[99] E. Ilievski and J. De Nardis, Phys. Rev. B **96**, 081118 (2017).

[100] B. Doyon, SciPost Phys. **5**, 054 (2018).

[101] B. Doyon and H. Spohn, SciPost Phys. **3**, 039 (2017).

[102] J.-S. Caux, B. Doyon, J. Dubail, R. Konik, and T. Yoshimura, SciPost Phys. **6**, 070 (2019).

[103] B. Doyon, H. Spohn, and T. Yoshimura, Nucl. Phys. B **926**, 570–583 (2018).

[104] B. Doyon, T. Yoshimura, and T. Yoshimura, SciPost Phys. **2**, 014 (2017).

[105] B. Doyon, J. Dubail, R. Konik, and T. Yoshimura, Phys. Rev. Lett. **119**, 195301 (2017).

[106] L. Piroli, J. De Nardis, M. Collura, B. Bertini, and M. Fagotti, Phys. Rev. B **96**, 115124 (2017).

[107] B. Bertini and L. Piroli, arXiv:1711.00519 (2017).

[108] B. Bertini, L. Piroli, and P. Calabrese, Phys. Rev. Lett. **120**, 176801 (2018).

[109] M. Mestyán, B. Bertini, L. Piroli, and P. Calabrese, Phys. Rev. B **99**, 014305 (2019).

[110] B. Bertini, L. Piroli, and M. Kormos, Phys. Rev. B **100**, 035108 (2019).

[111] A. Bastianello, B. Doyon, G. Watts, and T. Yoshimura, SciPost Phys. **4**, 045 (2018).

[112] B. Doyon and H. Spohn, J. Stat. Mech.: Theory and Experiment **2017**, 073210 (2017).

[113] B. Doyon, T. Yoshimura, and J.-S. Caux, Phys. Rev. Lett. **120**, 045301 (2018).

[114] B. Doyon, J. Math. Phys.
60, 073302 (2019).

[115] V. B. Bulchandani, J Phys. A: Math. Theor. **50**, 435203 (2017).

[116] V. B. Bulchandani, X. Cao, and J. E. Moore, J. Phys. A: Math. Theor. **52**, 33LT01 (2019).

[117] X. Cao, V. B. Bulchandani, and H. Spohn, arXiv:1905.04548 (2019).

[118] M. Schemmer, I. Bouchoule, B. Doyon, and J. Dubail, Phys. Rev. Lett. **122**, 090601 (2019).

[119] J. De Nardis, D. Bernard, and B. Doyon, Phys. Rev. Lett. **121**, 160603 (2018).

[120] J. De Nardis, D. Bernard, and B. Doyon, SciPost Phys. **6**, 049 (2019).

[121] S. Gopalakrishnan, D. A. Huse, V. Khemani, and R. Vasseur, Phys. Rev. B **98**, 220303 (2018).

[122] E. Ilievski, J. De Nardis, M. Medenjak, and T. Prosen, Phys. Rev. Lett. **121**, 230602 (2018).

[123] S. Gopalakrishnan and R. Vasseur, Phys. Rev. Lett. **122**, 127202 (2019).

[124] O. Gamayun, Y. Miao, and E. Ilievski, Phys. Rev. B **99**, 140301 (2019).

[125] M. Medenjak, C. Karrasch, and T. Prosen, Phys. Rev. Lett. **119**, 080602 (2017).

[126] S. Gopalakrishnan, R. Vasseur, and B. Ware, Proceedings of the National Academy of Sciences **116**, 16250–16255 (2019).

[127] M. Ljubotina, Z. Marko, and T. Prosen, J. Phy. A: Math. Theor. **50**, 475002 (2017).

[128] M. Ljubotina, M. Znidaric, and T. Prosen, Nat. Comm. **8**, 16117 (2017).

[129] K. Klobas, M. Medenjak, and T. Prosen, J. Stat. Mech.: Theor. Exp. **2018**, 123202 (2018).

[130] M. Ljubotina, M. Znidaric, and T. Prosen, Phys. Rev. Lett. **122**, 210602 (2019).

[131] V. B. Bulchandani, C. Karrasch, and J. E. Moore, (2019).

[132] V. B. Bulchandani and C. Karrasch, Phys. Rev. B **99**, 121410 (2019).

[133] D.-L. Vu and T. Yoshimura, SciPost Phys. **6**, 23 (2019).

[134] M. Borsi, B. Pozsgay, and L. Pristyák, arXiv:1908.07320 (2019).

[135] V. Alba and P. Calabrese, Phys. Rev. B **96**, 115421 (2017).

[136] V. Alba and P. Calabrese, J. Stat. Mech.: Theor. Exp. **2017**, 113105 (2017).

[137] M. Mestyán, V. Alba, and P. Calabrese, J. Stat. Mech.: Theor. Exp. **2018**, 083104 (2018).

[138] M. Brockmann, B. Wouters, D. Fioretto, J. D. Nardis, R. Vlijm, and J.-S. Caux, J. Stat. Mech.: Theor. Exp. **2014**, P12009 (2014).

[139] B. Pozsgay, J. Stat. Mech.: Theor. Exp. **2018**, 053103 (2018).

[140] V. Alba, Phys. Rev. B **99**, 045150 (2019).

[141] V. Alba and P. Calabrese, Proceedings of the National Academy of Sciences **114**, 7947–7951 (2017).

[142] V. Alba and P. Calabrese, SciPost Phys. **4**, 17 (2018).

[143] R. Islam, R. Ma, P. M. Preiss, M. Eric Tai, A. Lukin, M. Rispoli, and M. Greiner, Nature **528**, 77–83 (2015).

[144] A. J. Daley, H. Pichler, J. Schachenmayer, and P. Zoller, Phys. Rev. Lett. **109**, 020505 (2012).

[145] A. Elben, B. Vermersch, M. Dalmonte, J. I. Cirac, and P. Zoller, Phys. Rev. Lett. **120**, 050406 (2018).

[146] A. M. Kaufman, M. E. Tai, A. Lukin, M. Rispoli, R. Schittko, P. M. Preiss, and M. Greiner, Science **353**, 794–800 (2016).

[147] C. K. Lai, J. Math. Phys. **15**, 1675–1676 (1974).

[148] B. Sutherland, Phys. Rev. B **12**, 3795–3805 (1975).

[149] P. P. Kulish and N. Y. Reshetikhin, Sov. Phys. JETP **53**.

[150] L. A. Takhtajan, Phys. Lett. A **87**, 479–482 (1982).

[151] H. M. Babujian, Phys. Lett. A **90**, 479–482 (1982).

[152] P. P. Kulish, N. Y. Reshetikhin, and E. K. Sklyanin, Letters in Mathematical Physics **5**, 393–403 (1981).

[153] H. Johannesson, Phys. Lett. A **116**, 133–138 (1986).

[154] H. Johannesson, Nucl. Phys. B **270**, 235–272 (1986).

[155] A. B. Zamolodchikov and A. B. Zamolodchikov, Ann. Phys. **120**, 253–291 (1979).

[156] N. Andrei, K. Furuya, and J. H. Lowenstein, Reviews of Modern Physics **55**, 331–402 (1983).

[157] Y.-J. Jee, K.-J.-B. Lee, and P. Schlottmann, Phys. Rev. B **39**, 2815–2818 (1989).

[158] L. Mezincescu, R. I. Nepomechie, P. K. Townsend, and A. M. Tsvelik, Nucl. Phys. B **406**, 681–707 (1993).

[159] A. Doikou and R. I. Nepomechie, Nucl. Phys. B **521**, 547–572 (1998).

[160] M. de Leeuw, C. Kristjansen, and S. Mori, Phys. Lett. B **763**, 197–202 (2016).

[161] S. R. White and A. E. Feiguin, Phys. Rev. Lett. **93**, 076401 (2004).

[162] A. J. Daley, C. Kollath, U. Schollw ock, and G. Vidal, J. Stat. Mech.: Theor. Exp. **2004**, P04005 (2004).

[163] U. Schollw ock, Reviews of Modern Physics **77**, 259–315 (2005).

[164] M. de Leeuw, C. Kristjansen, and K. Zarembo, J. High. Energy Phys. **2015**, 98 (2015).

[165] I. Buhl-Mortensen, M. de Leeuw, C. Kristjansen, and K. Zarembo, J. High. Energy Phys. **2016** (2015).

[166] O Foda and K Zarembo, J. Stat. Mech.: Theor. Exp. **2016** (2015).

[167] L. Piroli, P. Calabrese, and F. Essler, SciPost Phys. **1**, 001 (2016).

[168] L. Amico, R. Fazio, A. Osterloh, and V. Vedral, Reviews of Modern Physics **80**, 517–576 (2008).

[169] J. Eisert, M. Cramer, and M. B. Plenio, Reviews of Modern Physics **82**, 277–306 (2010).

[170] P. Calabrese, J. Cardy, and B. Doyon, J. Phys. A: Math. Theor. **42**, 500301 (2009).

[171] N. Laflorencie, Phys. Rep. **646**, 1–59 (2016).

[172] P. Calabrese and J. Cardy, J. Stat. Mech.: Theor. Exp. **2005**, P04010 (2005).

[173] P. Calabrese and J. Cardy, Phys. Rev. Lett. **96**, 136801 (2006).

[174] P. Calabrese and J. Cardy, J. Stat. Mech.: Theor. Exp. **2007**, P06008–P06008 (2007).

[175] M. G. Nezhadhaghighi and M. A. Rajabpour, Phys. Rev. B **90**, 205438 (2014).

[176] M. Fagotti and P. Calabrese, Phys. Rev. A **78**, 010306 (2008).

[177] A. Coser, E. Tonni, and P. Calabrese, J. Stat. Mech.: Theor. Exp. **2014**, P12017 (2014).

[178] V. Eisler and I. Peschel, Annalen der Physik **17**, 410–423 (2008).

[179] J. S. Cotler, M. P. Hertzberg, M. Mezei, and M. T. Mueller, J. High. Energy Phys. **2016**, 166 (2016).

[180] G. D. Chiara, S. Montangero, P. Calabrese, and R. Fazio, J. Stat. Mech.: Theor. Exp. **2006**, P03001–P03001 (2006).

[181] A. M. L auchli and C. Kollath, J. Stat. Mech.: Theor. Exp. **2008**, P05018 (2008).

[182] H. Kim and D. A. Huse, Phys. Rev. Lett. **111**, 127205 (2013).

[183] M. Collura, P. Calabrese, and F. H. L. Essler, Phys. Rev. B **92**, 125131 (2015).

[184] A. Nahum, J. Ruhman, S. Vijay, and J. Haah, Phys. Rev. X **7**, 031016 (2017).

[185] P. Calabrese and J. Cardy, J. Stat. Mech.: Theor. Exp. **2007**, P10004–P10004 (2007).

[186] V. Eisler and I. Peschel, J. Stat. Mech.: Theor. Exp. **2007**, P06005–P06005 (2007).

[187] J.-M. Stéphan and J. Dubail, J. Stat. Mech.: Theor. Exp. **2011**, P08019 (2011).

[188] B. Bertini, Phys. Rev. B **95**, 075153 (2017).

[189] J. Dubail, J.-M. Stéphan, J. Viti, and P. Calabrese, SciPost Phys. **2**, 002 (2017).

[190] B. Bertini and M. Fagotti, Phys. Rev. Lett. **117**, 130402 (2016).

[191] L. F. Santos, A. Polkovnikov, and M. Rigol, Phys. Rev. Lett. **107**, 040601 (2011).

[192] V. Gurarie, J. Stat. Mech.: Theor. Exp. **2013**, P02014 (2013).

[193] M. Collura, M. Kormos, and P. Calabrese, J. Stat. Mech.: Theor. Exp. **2014**, P01009 (2014).

[194] L. Bucciantini, M. Kormos, and P. Calabrese, J. Phys. A: Math. Theor. **47**, 175002 (2014).

[195] D. A. Roberts and D. Stanford, Phys. Rev. Lett. **115**, 131603 (2015).

[196] S. H. Shenker and D. Stanford, J. High. Energy Phys. **2014**, 67 (2014).

[197] C. T. Asplund, A. Bernamonti, F. Galli, and T. Hartman, J. High. Energy Phys. **2015**, 110 (2015).

[198] S. Leichenauer and M. Moosa, Phys. Rev. D **92**, 126004 (2015).

[199] K. K. Kozlowski and B. Pozsgay, J. Stat. Mech.: Theor. Exp. **2012**, P05021 (2012).

[200] B. Pozsgay, J. Stat. Mech.: Theor. Exp. **2014**, P06011 (2014).

[201] M. Kormos, Y.-Z. Chou, and A. Imambekov, Phys. Rev. Lett. **107**, 230405 (2011).

[202] B. Pozsgay, J. Stat. Mech.: Theor. Exp. **2011**, P11017 (2011).

[203] B. Bertini, L. Piroli, and P. Calabrese, J. Stat. Mech.: Theor. Exp. **2016**, 063102 (2016).

[204] S. Negro and F. Smirnov, Nucl. Phys. B **875**, 166–185 (2013).

[205] L. D. Faddeev, arXiv:hep-th/9605187 (1996).

[206] V. Alba, Phys. Rev. B **97**, 245135 (2018).

[207] B. Bertini, M. Fagotti, L. Piroli, and P. Calabrese, J. Phys. A: Math. Theor. **51**, 39LT01 (2018).

[208] V. Alba, B. Bertini, and M. Fagotti, SciPost Phys. **7**, 005 (2019).

[209] M. Mestyán and V. Alba, arXiv:1905.03206 (2019).

[210] C. Boldrighini, R L. Dobrushin, and Y. M. Sukhov, J. Stat. Phys. **31**, 577–616 (1983).

[211] W. Krauth, *Statistical mechanics: algorithms and computation* (Cambridge University Press, 2006).

[212] M. Fagotti, Phys. Rev. B **96**, 220302 (2017).

[213] V. Alba and P. Calabrese, arXiv:1903.09176 (2019).

[214] V. Alba, J. Dubail, and M. Medenjak, Phys. Rev. Lett. **122**, 250603 (2019).

[215] M. Gaudin, Phys. Lett. A **24**, 55 –56 (1967).

[216] C. N. Yang, Phys. Rev. Lett. **19**, 1312–1315 (1967).

[217] J. B. McGuire, J. Mat. Phys. **6**, 432–439 (1965).

[218] M. Flicker and E. H. Lieb, Phys. Rev. **161**, 179–188 (1967).

[219] M. Takahashi, Prog. Theor. Phys. **46**, 1388–1406 (1971).

[220] J. Y. Lee, X. W. Guan, K. Sakai, and M. T. Batchelor, Phys. Rev. B **85**, 085414 (2012).

[221] M. Takahashi, Prog. Theor. Phys. **50**, 1519–1536 (1973).

[222] D. Bernard and B. Doyon, J. Phys. A: Math. Theor. **45**, 362001 (2012).

[223] D. Bernard and B. Doyon, J. Stat. Mech.: Theor. Exp. **2016**, 064005 (2016).

[224] A. Imambekov and L. I. Glazman, Science **323**, 228–231 (2009).

[225] L. Piroli, E. Vernier, P. Calabrese, and B. Pozsgay, J. Stat. Mech.: Theor. Exp. **2019**, 063103 (2019).

[226] L. Piroli, E. Vernier, P. Calabrese, and B. Pozsgay, J. Stat. Mech.: Theor. Exp. **2019**, 063104 (2019).